

CAT. 15 CODE-1

XEROX

OTS PRICE

6.60 ph.

May 1, 1964

**Copyright © 1964  
Jet Propulsion Laboratory  
California Institute of Technology**

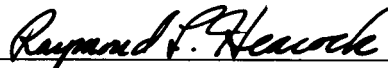
**Prepared Under Contract No. NAS 7-100  
National Aeronautics & Space Administration**

*Technical Report No. 32-492*

*An Instrument for the Measurement of  
Interplanetary Solar Plasma*

*Conrad Josias*

*James Lawrence, Jr.*



---

Raymond Heacock, Chief  
Space Instruments Development Section

JET PROPULSION LABORATORY  
CALIFORNIA INSTITUTE OF TECHNOLOGY  
PASADENA, CALIFORNIA

May 1, 1964

## CONTENTS

<b>I. Introduction</b>	1
<b>II. Functional Description</b>	3
A. The Basic System	3
B. <i>Ranger 1, 2</i> Plasma Instruments	3
1. Deflection Voltage System	3
2. Electrometer	5
C. <i>Mariner 2</i> Plasma Instrument	6
<b>III. The Electrometer System</b>	10
A. The Logarithmic Compressor	10
1. Unipolar Circuit	10
2. Bipolar Circuit	11
3. Dynamic Equivalent Circuit	13
B. The Electrometer Amplifier	13
1. Detailed Description	14
2. Design Choices	15
3. Gain	15
4. Offset Stability	25
C. Feedback Stability	26
1. Open-Loop Frequency Response	26
2. Closed-Loop Performance	31
D. Dynamic Reed Capacitor Development	33
<b>IV. The Deflection Voltage System</b>	37
A. Electrostatic Deflection Plates	37
B. Digital Programmer	38
C. High-Voltage Sweep Amplifier	40
<b>V. The <i>Mariner 2</i> Flight Instrument</b>	51
A. Preflight Calibrations	51
B. Flight Performance	55
1. General Flight Data	55
2. Instrument Performance	55
3. Scientific Results	57
<b>Nomenclature</b>	59
<b>References</b>	61



## TABLES

1. Measurement cycle for <i>Ranger</i> solar plasma instruments . . . . .	5
2. Particle energies corresponding to voltage across <i>Ranger</i> deflection plates . . . . .	5
3. Solar plasma particle energies corresponding to <i>Mariner 2</i> deflection plate voltages . . . . .	7
4. Performance of filament current regulator . . . . .	11
5. Nominal time constants and corner frequencies . . . . .	29
6. Component values . . . . .	31
7. Dominant time constants and corner frequencies for nominal closed-loop response . . . . .	32
8. Output voltage vs. temperature for <i>Ranger</i> sweep system . . . . .	50
9. Preflight electrometer performance . . . . .	52
10. Final preflight electrometer calibrations . . . . .	53
11. Preflight deflection voltage calibration . . . . .	54
12. Spacecraft events affecting cruise science . . . . .	56
13. Electrometer calibration history . . . . .	56
14. Manually collated plasma data beginning Sept. 24, 1962 (Day 267), 23:55 GMT . . . . .	58

## FIGURES

1. Block diagram of basic solar plasma instrumentation . . . . .	3
2. <i>Ranger 1, 2</i> spacecraft . . . . .	4
3. Block diagram of the <i>Ranger</i> solar plasma instrument . . . . .	5
4. 180-deg solar plasma analyzer used on the <i>Ranger</i> . . . . .	6
5. Dual electrometer compartment . . . . .	6
6. Calculated <i>Mariner 2</i> solar plasma experiment response as functions of particle energy and incident angle . . . . .	7
7. <i>Mariner 2</i> spacecraft . . . . .	8
8. <i>Mariner 2</i> solar plasma instrument . . . . .	9

## FIGURES (Cont'd)

9. Thermionic diode and associated characteristic . . . . .	10
10. Filament current regulator . . . . .	11
11. Bipolar logarithmic current-to-voltage compressor . . . . .	12
12. Bipolar logarithmic characteristics . . . . .	12
13. Bipolar logarithmic electrometer . . . . .	12
14. Dynamic equivalent circuit of a logarithmic diode . . . . .	13
15. <i>Mariner 2</i> electrometer block diagram . . . . .	14
16. <i>Mariner 2</i> electrometer schematic diagram . . . . .	17
17. Simplified diagram of carrier section . . . . .	19
18. Reduction of modulator—preamplifier cascade to Thevenin equivalent circuit . . . . .	19
19. Plot of preamplifier gain vs. frequency . . . . .	19
20. Triplet amplifier . . . . .	20
21. Carrier amplifier performance curves . . . . .	20
22. Demodulator and associated waveforms . . . . .	21
23. DC filter amplifier . . . . .	24
24. Static transfer characteristic of carrier section . . . . .	25
25. Equivalent circuits for determining loop transmission . . . . .	26
26. Asymptotic loop transmission responses without secondary feedback . . . . .	29
27. Asymptotic loop transmission responses with secondary feedback . . . . .	29
28. Test setup for loop transmission measurements . . . . .	30
29. Gain and phase curves with secondary feedback in ( $I_{bias} = 10^{-6}$ amp) . . . . .	30
30. Gain and phase curves with secondary feedback in ( $I_{bias} = 10^{-9}$ amp) . . . . .	30
31. Gain and phase curves with secondary feedback in ( $I_{bias} = 10^{-10}$ amp) . . . . .	30
32. Gain and phase curves with secondary feedback out ( $I_{bias} = 10^{-11}$ amp) . . . . .	30
33. Gain and phase curves with secondary feedback out ( $I_{bias} = 10^{-12}$ amp) . . . . .	31
34. Gain and phase curves with secondary feedback out ( $I_{bias} = 10^{-13}$ amp) . . . . .	31
35. Closed-loop frequency response with secondary feedback . . . . .	32
36. Closed-loop frequency response without secondary feedback . . . . .	32

## FIGURES (Cont'd)

37. Closed-loop transient response . . . . .	33
38. Dynamic capacitor on mounting base . . . . .	34
39. Uncased dynamic capacitor . . . . .	34
40. Resonant characteristic of early prototype dynamic capacitor vs. temperature . . . . .	35
41. Dynamic capacitor assembly . . . . .	36
42. Ranger programmer block diagram . . . . .	39
43. Mariner 2 programmer schematic diagram . . . . .	41
44. Partial schematic diagram of programmer reference and sweep amplifier input . . . . .	43
45. Ranger high-voltage sweep amplifier block diagram . . . . .	44
46. Ranger sweep amplifier schematic diagram . . . . .	45
47. Mariner sweep amplifier schematic diagram . . . . .	46
48. Mariner sweep amplifier loop transmission response . . . . .	47
49. Main sweep amplifier equivalent circuit . . . . .	49
50. Thermal drift characteristics vs. reference base resistor for typical Mariner sweep amplifier . . . . .	50
51. Portion of secondary feedback connected ( $\beta_2$ ) vs. input current . . . . .	52
52. Vacuum—temperature electrometer calibrations, May 8, 1962 . . . . .	53
53. Electrometer transient response . . . . .	57

## ACKNOWLEDGMENTS

It is with great pleasure that we acknowledge H. R. Mertz and L. D. Bowman for their engineering role in the development of the *Mariner 2* plasma instrument. Their responsibilities included modifications to the *Ranger* design and the development of the *Mariner* flight instrument package. Their extended participation in this program, from the management of the hardware development to the prelaunch checkout activities, was one of the most important factors in the successful history of this instrument. We are also indebted to G. Fagg, R. Holman, H. Richeson, and T. J. Theis, project members whose skills and workmanship were testified to by the *Mariner 2* plasma instrument flight performance. It is also fitting that we acknowledge L. Brashear, R. Graham, and L. Simmons, whose contributions on the *Ranger* instrument paved the way for the more refined instrument used on the *Mariner*.

We wish to thank J. H. Marshall and J. R. Locke for their assistance in the preparation of evaluation and performance data on the *Mariner 2* electrometer. Valuable suggestions by R. Heacock and R. Heyser, perhaps remembered only vaguely by them as conversational ideas, were subsequently incorporated into the designs presented in this paper. We also note the efficient dynamic capacitor drive oscillator designed by D. W. Slaughter.

The dynamic capacitor was one of the most important elements in this instrumentation, and for its timely development we wish to express our sincere gratitude to the Applied Physics Corporation of Monrovia, California. We especially want to thank W. Williams of this company for his personal cooperation and diligence in delivering stable and reliable modulators to JPL.

### ACKNOWLEDGMENTS (Cont'd)

Much of the fine craftsmanship in the experimental fabrication and mechanical design preliminary to both *Ranger* and *Mariner* flight units was done by K. La Bau. The deflection plates for the flight instruments and the vacuum chambers for ground testing were provided by G. Hotz, R. Hahn, and P. Schaper. The first of the four flight units was built at JPL and the remaining three were assembled with excellent workmanship at Dynamics Instrumentation Company of Monterey Park, California.

Finally, we would like to express our appreciation to Dr. D. H. Le Croisette and Mrs. M. F. Buehler for their editorial assistance with this Report.

20603

## ABSTRACT

A

An important scientific result of the interplanetary flight of the *Mariner 2* spacecraft to the planet Venus was the collection of extensive detailed data indicating the presence of a constantly flowing "solar wind." This Report describes the *Mariner 2* solar plasma instrument and its predecessor, which flew on *Rangers 1* and *2*. Special emphasis is given to the discussion of a wide-range electrometer system stabilized by a dynamic capacitor.

The instrument described here measures charged-particle energy spectra with a sensor consisting of a pair of concentric curved electrostatic deflection plates terminated by an isolated Faraday collector cup. The collection rate of charged particles is measured with an electrometer whose wide dynamic current range is provided by a logarithmic compressor composed of one or two subminiature thermionic diodes operated in the retarded field region. The electrostatic field is controlled by a programmed high-voltage sweep amplifier that provides the deflection plates with voltages of equal magnitude but opposite polarity.

The Report includes a history of preflight testing and calibration of the *Mariner 2* flight instrument, in addition to some details of its flight performance.

AUTHOR

## I. INTRODUCTION

The Venus-bound spacecraft, *Mariner 2*, which was successfully launched on August 27, 1962, carried a group of instruments to perform interplanetary scientific measurements. One of these instruments was a solar plasma analyzer, a device capable of analyzing the energy spectrum of the positive-ion component of a suspected solar wind. The usefulness of such solar plasma measurements was to be notably complemented by concurrent magnetic field measurements performed by another instrument, a magnetometer.

This launching began an operational flight of 129 days, during which data from several instruments including the plasma spectrometer were continuously monitored and evaluated for scientific disclosures and instrument performance. This Report describes the *Mariner 2* plasma instrument with respect to its design and flight performance and also discusses aspects of its predecessor flown on *Rangers 1* and *2*.

The study of fields and particles has occupied an important place in the scientific program of recent years

for unmanned lunar and planetary exploration of space. Of particular interest in this area is the low-energy solar corpuscular radiation sometimes called solar plasma or the solar wind (Ref. 1, 2). The determination of the flux of these particles as a function of (1) their energy and direction of travel, (2) the magnetic field that accompanies them, and (3) time is an essential step in the understanding of the physics of the solar corona, the modulation of cosmic rays, the distortion of the terrestrial and lunar magnetic fields, and many solar-terrestrial phenomena such as magnetic storms, auroras, and time variation in the contents and extent of the Van Allen belts. Various theories of the solar corona have predicted the direction of travel of the interplanetary plasma to be isotropic (Ref. 3), radially away from the Sun (Ref. 4, 5), or perpendicular to the ecliptic along a field line of a solar magnetic dipole (Ref. 6). The solar plasma was predicted to contain electrons, protons, and some heavier positive ions which have velocities near 300 km/sec. The energy of most of the electrons in the plasma streams would then be a few electron volts, with positive ion energies in the kilovolt range.

Measurement of this radiation by conventional methods is made somewhat difficult by the fact that the

energies of these particles may be so low as to preclude penetration of even the thinnest of the thin-walled counters. For this reason, the detector system about which the instrumentation in this report is designed was chosen to provide an unobstructed collection path for those charged particles of interest. This detector is the curved-plate electrostatic analyzer. The formulation of experiments to be conducted with these plasma analyzers and the design of the electrostatic deflection plates have been the responsibilities of M. M. Neugebauer and C. W. Snyder of the Jet Propulsion Laboratory (JPL).

The principal goals of these solar plasma experiments, in summary, were to perform interplanetary measurements to determine the extent of, and the variations in, the solar corona. A correlated engineering requirement was the development of an electronic system providing, within the minimal weight and power allocations customary in these applications, stable and reliable performance over periods of time required to traverse planetary distances. An additional goal was to provide instrumentation capable of being used in various low-current applications.

## II. FUNCTIONAL DESCRIPTION

### A. The Basic System

The basic electrostatic system is illustrated in Fig. 1. Charged particles entering the instrument are deflected by an electric field approximately transverse to the particle velocity. Those particles with a particular charge sign and within a certain range of energy per unit charge and a certain range of angle of incidence are deflected through the curved tunnel onto the charge collector. Particles that enter the instrument with the wrong charge sign, energy per unit charge, or angle of incidence strike the analyzer walls and are not collected. The energy distributions of both positively and negatively charged particles entering the device can be determined by varying the sign and magnitude of the deflection voltage. The charge collection rate is measured at each energy level by a wide-range electrometer.

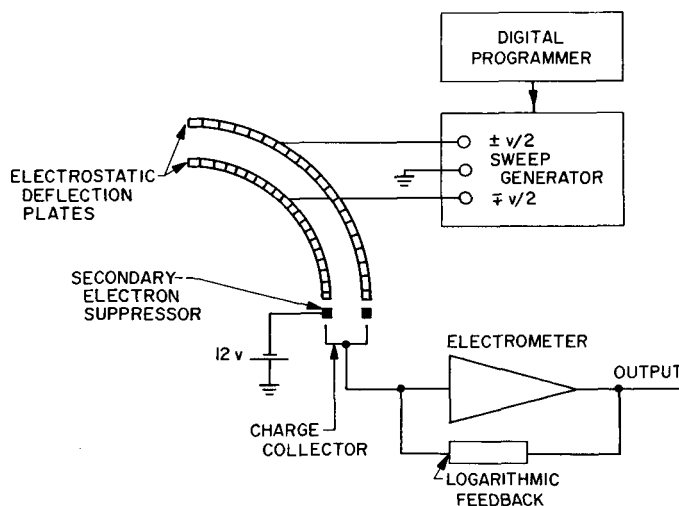


Fig. 1. Block diagram of basic solar plasma instrumentation

### B. Ranger 1, 2 Plasma Instruments

The primary mission of the first two *Ranger* spacecraft was to test the performance of those functions and parts of the spacecraft necessary for carrying out subsequent lunar and planetary missions using essentially the same spacecraft design. The secondary mission was the further determination of the nature of the particles and fields in interplanetary space. The plasma instruments, like most of the other *Ranger 1, 2* instruments, were directed toward the study of certain solar-terrestrial relationships, such as the correlation between geomagnetic storms and the solar wind.

One of the most important considerations in the *Ranger*-type spacecraft (the *Mariner* configuration is similar), is that the vehicle is attitude-stabilized in such a manner that the axis of symmetry (and thus the sensitive surface of the solar panels) points toward the Sun, and the plane that contains this axis and the high-gain antenna also contains the Earth (Fig. 2).

Six plasma detectors, each with an acceptance angle of approximately 15 deg, were situated on the spacecraft so as to point in six orthogonal directions: toward and away from the Sun, approximately forward and backward in the ecliptic, and approximately north and south of the ecliptic. The analyzers were assembled in pairs, and as seen in Fig. 2, the pair of analyzers pointing toward and away from the Sun was located on a boom intended to place the analyzers beyond the plasma sheath of the vehicle itself. The determination of the direction of particle travel was expected to make it possible to choose among the principal theoretical models for the interplanetary plasma.

The basic *Ranger* assembly is outlined in the block diagram of Fig. 3. The electrostatic drive for the deflection plates is supplied by a programmable high-voltage sweep amplifier. By having the ability to change the polarity of the deflection plate voltages, this amplifier enables the deflection system to focus either electrons or positive ions onto the collector. The sweep program was selected to provide discrimination at four electron energy levels between and including 13.7 and 110 ev. Similarly, eight positive-ion energy levels between 13.7 and 5,490 ev were to be monitored.

#### 1. Deflection Voltage System

The high-voltage amplifier is programmed by a  $4 \times 13$  diode matrix which consecutively gates a reference voltage to one of the 12 input resistors of the amplifier. The matrix is driven by a four-stage binary counter which accepts one pulse per 9 sec from the spacecraft Data Automation System (DAS). A reset pulse from the DAS every 120 sec recycles the counter for another measurement sequence. The measurement cycle is shown in Table 1.

The voltage drive for both pairs of deflection plates consists of an operational amplifier having wide dynamic range, augmented by two subsidiary amplifiers for generation of stable low-voltage steps. This system



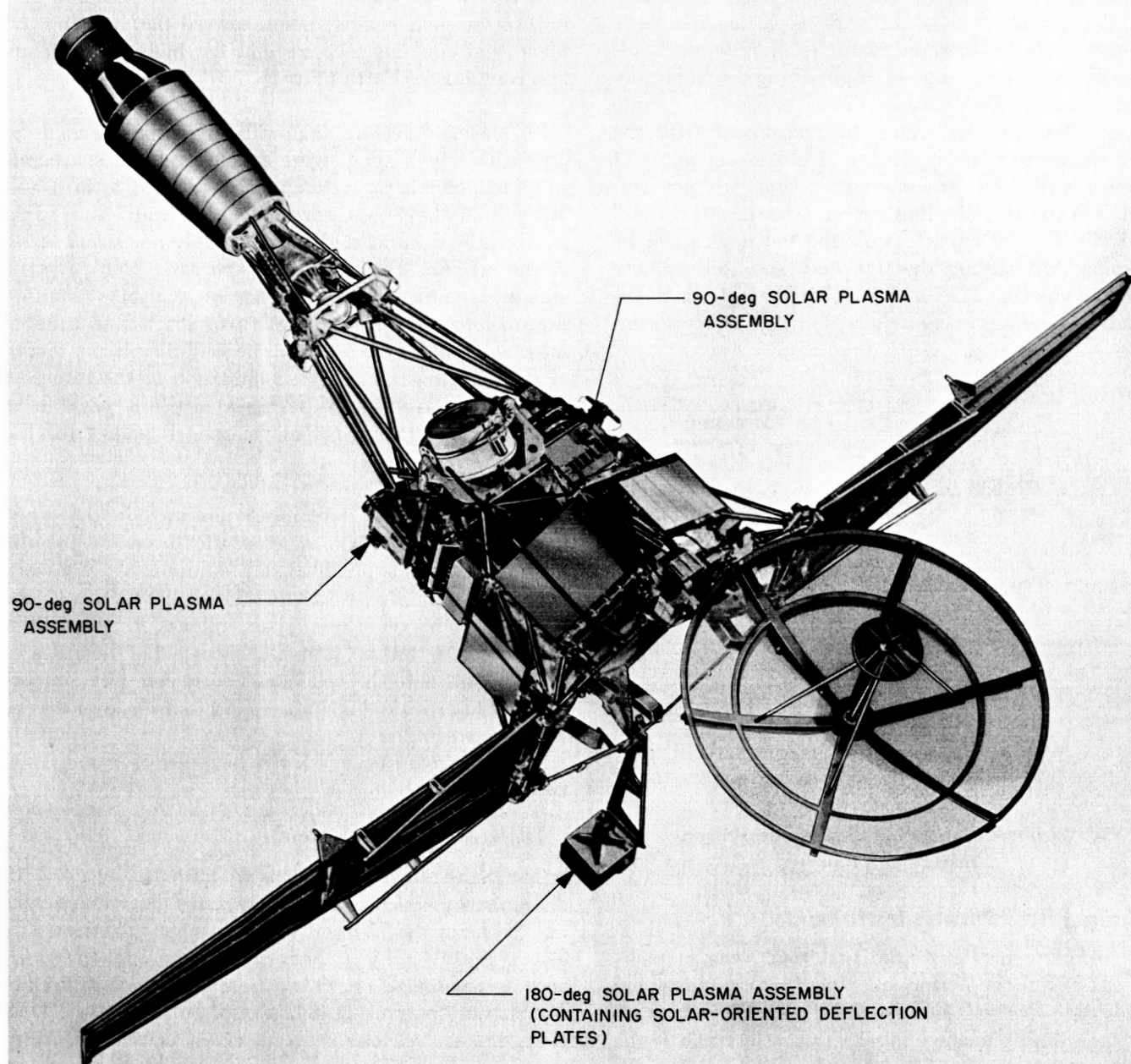


**Fig. 2. Ranger 1, 2 spacecraft**

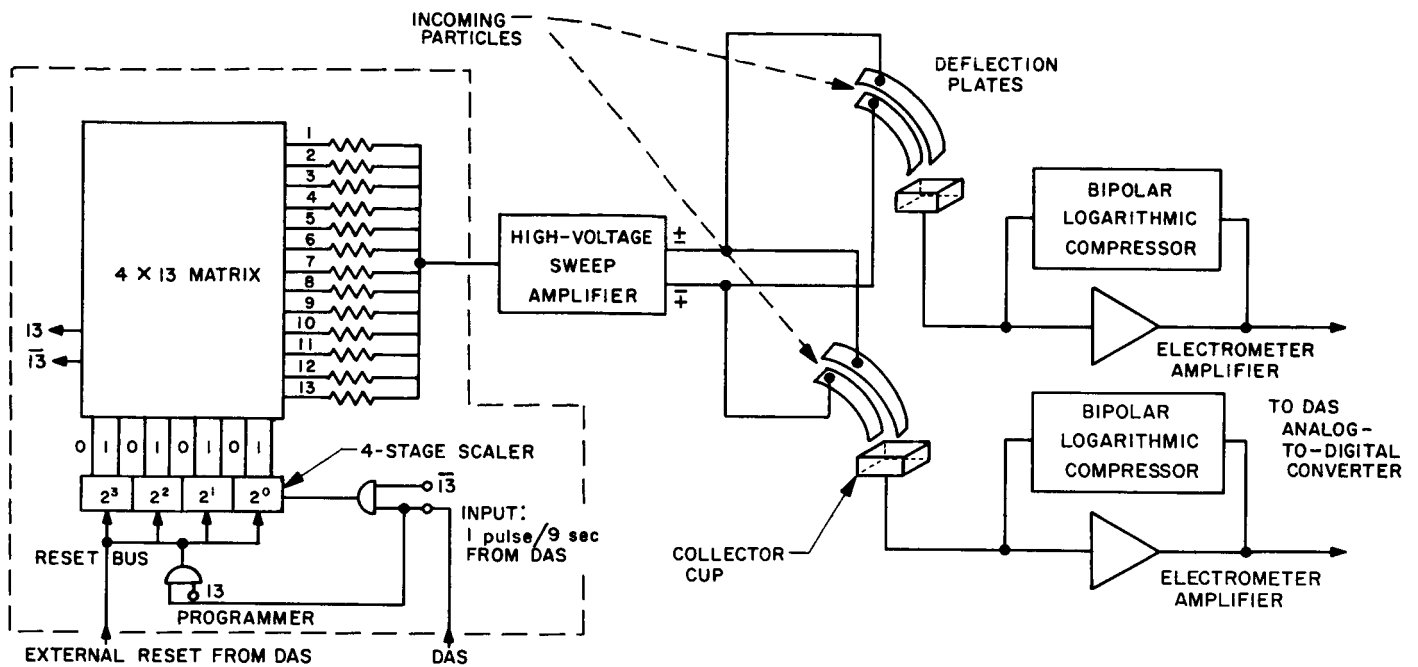


Fig. 3. Block diagram of the *Ranger* solar plasma instrument

delivers programmed voltages of +100 to -1,000 v dc and -100 to +1,000 v dc to the inner and outer plates, respectively. The differential voltages across the deflec-

tion plates and the corresponding energy levels are shown in Table 2.

Table 1. Measurement cycle for *Ranger* solar plasma instruments

Interval	Time, sec	Operation
1	0 to 9	Deflection voltages are set at step 1.
1	8 to 8.5	Outputs of all six electrometers are simultaneously converted to 8-bit digital form and stored by the DAS.
2	9 to 18	Deflection voltages are set at step 2, and data from interval 1 are commutated to the communications system at a standard telemetry transmission rate.
3 ↓ 12	10 consecutive 9-sec intervals	Measurement procedures are the same as in the first interval. In each interval, data of the previous interval are telemetered.
13	108 to 120	Deflection voltages are set at the step 1 level, but the electrometers are not sampled in this period.

Table 2. Particle energies corresponding to voltage across *Ranger* deflection plates

Step number	Deflection plate voltage (outer minus inner), v	Particle energy, ev
1	-40	110 <sup>a</sup>
2	-20	54.9 <sup>a</sup>
3	-10	27.4 <sup>a</sup>
4	-5	13.7 <sup>a</sup>
5	5	13.7 <sup>b</sup>
6	10	27.4 <sup>b</sup>
7	20	54.9 <sup>b</sup>
8	65	178 <sup>b</sup>
9	151	414 <sup>b</sup>
10	365	1,000 <sup>b</sup>
11	840	2,300 <sup>b</sup>
12	2,000	5,490 <sup>b</sup>

<sup>a</sup>Electron.  
<sup>b</sup>Positive ion.

## 2. Electrometer

The current-measuring part of the instrument consists of a dual logarithmic current-to-voltage transducer and

a dynamic capacitor-modulated carrier-type dc amplifier. The logarithmic device produces compression of both electron and positive-ion currents between  $10^{-13}$  and  $10^{-6}$  amp; for the deflection plate geometry being used, these currents correspond to particle fluxes ranging between  $8.6 \times 10^4$  and  $8.6 \times 10^{11} \text{ cm}^{-2} \text{ sec}^{-1}$  for each energy interval. The compressed analog output is converted to 8-bit digital form for transmission accuracy.

The twin-analyzer assemblies were produced in two forms. The two assemblies mounted on the superstructure above the main, hexagonally shaped body of the spacecraft (Fig. 2) each contained deflection systems whose apertures were 90 deg apart. The combined effect of having these two similarly constructed units on diagonal corners of the spacecraft was to produce four unobstructed analyzing views orthogonal to the axis of symmetry. The third assembly (illustrated in Fig. 4), which was extended from the vehicle at the end of a boom, contained apertures 180 deg apart for looking toward and away from the Sun. A compartment containing two electrometers, which is partially obscured in Fig. 4, is shown in Fig. 5.

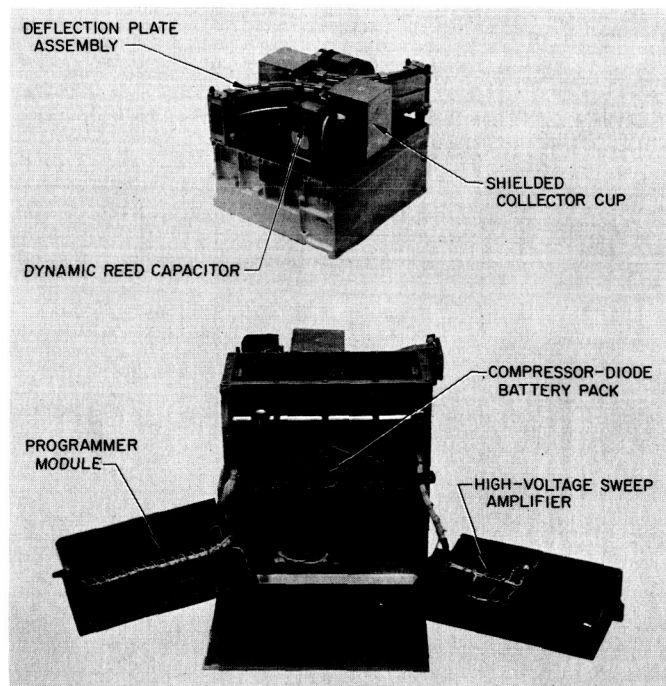


Fig. 4. 180-deg solar plasma analyzer used on the *Ranger*

*Rangers 1* and *2* were to be placed in "parking" or satellite orbits by *Atlas-Agena B* launch vehicles. At the end of the parking orbits, the spacecraft were to be ac-

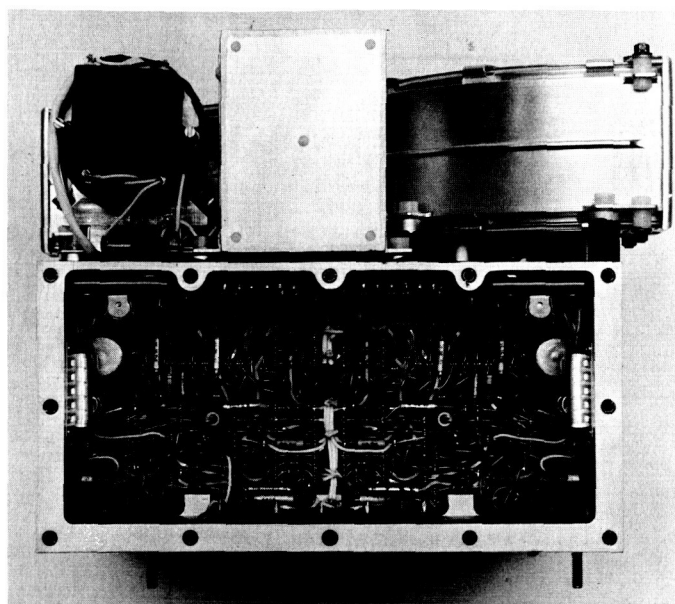


Fig. 5. Dual electrometer compartment

celerated from orbital velocity to nearly escape velocity in a direction away from the Moon (Ref. 7). *Ranger 1* was launched at 6:04 a.m. Eastern Daylight Time on August 23, 1961. The velocity increment needed to accelerate the spacecraft into a highly eccentric orbit from the parking phase did not occur, and as a result, *Ranger 1* was placed in a low Earth orbit (Ref. 8). The solar plasma experiment produced data of little scientific or engineering value, owing to orientation problems and ionospheric interactions.

### C. Mariner 2 Plasma Instrument

During the time when *Ranger 2* was being prepared for launch at the Atlantic Missile Range (AMR), a new passenger opportunity for a plasma instrument was presented. Work was proceeding at this time on the assembly of an 1,100-lb spacecraft called *Mariner* that was to be launched toward Venus in the following year by the *Atlas-Centaur* vehicle. However, after one of the two years allotted between spacecraft inception and launch had elapsed, it was established that *Centaur* would not be available for the planetary launch opportunity. A new *Mariner* spacecraft was being formulated, based upon an abbreviated schedule and the lesser weight-lifting capability of the *Atlas-Agena*. The new spacecraft was patterned after the *Ranger* system in terms of communication, guidance, control, and structure; however, the weight allocations for the components on the new spacecraft were more restrictive than those for the original *Mariner*. Scientific hardware, for example, was limited to 44 lb.

Based upon allocations of 5 pounds and 1 watt, one of the most important questions asked at this time was, "How comprehensive an experiment can be performed with one analyzer where six were required for the *Ranger 1* and 2 experiment?" Important observations made in March 1961 on *Explorer X* (Ref. 9, 10) suggested a radial flow of plasma from the Sun. With this valuable information, a single solar-oriented analyzer was proposed for *Mariner*. Subsequent approval required that the instrument be delivered within three months. The accelerated delivery requirement was considered realistic primarily because the *Mariner* package was patterned closely after the *Ranger* instrument.

The *Mariner* instrument did, however, provide a valuable opportunity for improving and updating the existing design. The electrostatic deflection plates, for instance, were extended from a 90-deg sector curve to a 120-deg curve. The ground rails separating the high-voltage plates were mechanically improved, and the collector-to-shield design was altered, thereby reducing collector-to-ground capacitance by 60%. The programming section of the instrument remained virtually unaltered, and deflection voltages were now supplied exclusively by the main high-voltage *Ranger* sweep amplifier. The new instrument was limited to positive-ion measurements of such energy levels as to make it possible to discard both positive and negative subsidiary amplifiers.

The sweep program is shown in Table 3 and the theoretical energy resolution and directionality are shown in Fig. 6, where the fraction of a beam of singly charged particles with energy  $E$ , incident at various angles on an analyzer, that reaches the collector cup is plotted vs.  $E/E_c$ . The energy  $E_c$  is that required for a trajectory with a constant radius of curvature for normally incident, singly charged particles. The value of  $E_c$  for the spacing and the 120-deg circular-sector geometry of the *Mariner* plates is four times the deflection voltage (Ref. 11, 12).

The electrometer made compressed measurements of only positive-ion current, thereby dispensing with a vacuum tube and its battery-operated filament-current supply. Other modifications of the electrometer circuit were as follows:

1. Nonlinear secondary feedback was introduced, resulting in improved low-current transient response.
2. A  $10^{-10}$  amp in-flight calibration was added.
3. A discriminator circuit was added to prevent amplifier saturation due to negative background current.

**Table 3. Solar plasma particle energies corresponding to *Mariner 2* deflection plate voltages**

Programmer step level	Voltage (nominal) across deflection plates, v	Energy $E_c$ of particles reaching cup, ev
1	60	240
2	90	360
3	132	528
4	196	784
5	290	1,160
6	425	1,700
7	630	2,520
8	950	3,800
9	1,400	5,600
10	2,100	8,400
11	-1.4	— <sup>a</sup>
12	-1.4	— <sup>b</sup>

<sup>a</sup>Low-energy and background measurement.

<sup>b</sup>Electrometer calibration.

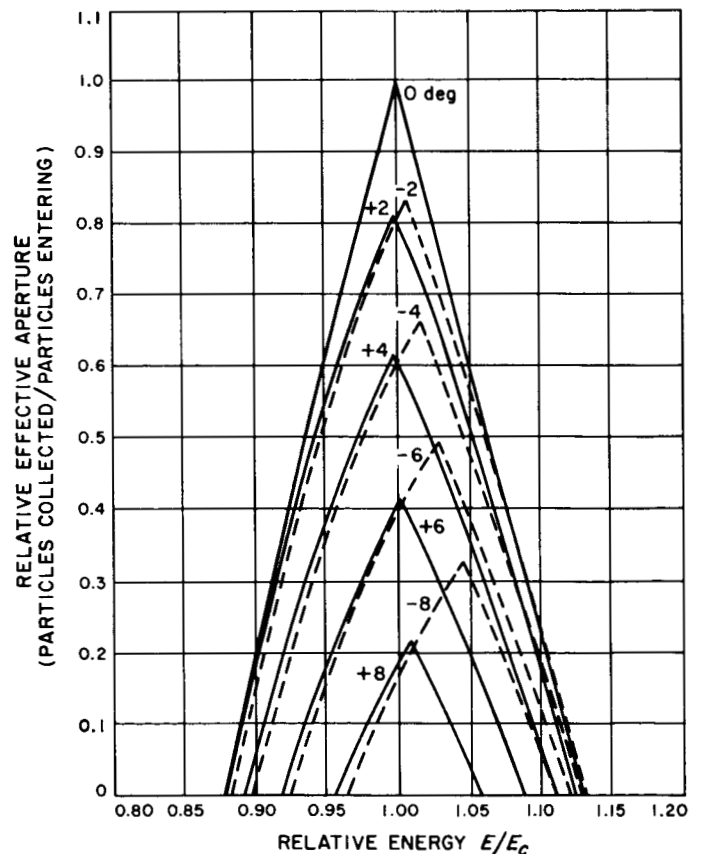


**Fig. 6. Calculated *Mariner 2* solar plasma experiment response as functions of particle energy and incident angle**



4. An improved dynamic-capacitor modulator was used.
5. Modulator excitation was now supplied by a self-resonant electro-acoustical oscillator.

The *Mariner* version of the plasma instrument is shown in Fig. 7 on board the *Mariner 2* spacecraft. It is shown once again in a somewhat less obscured view in Fig. 8.

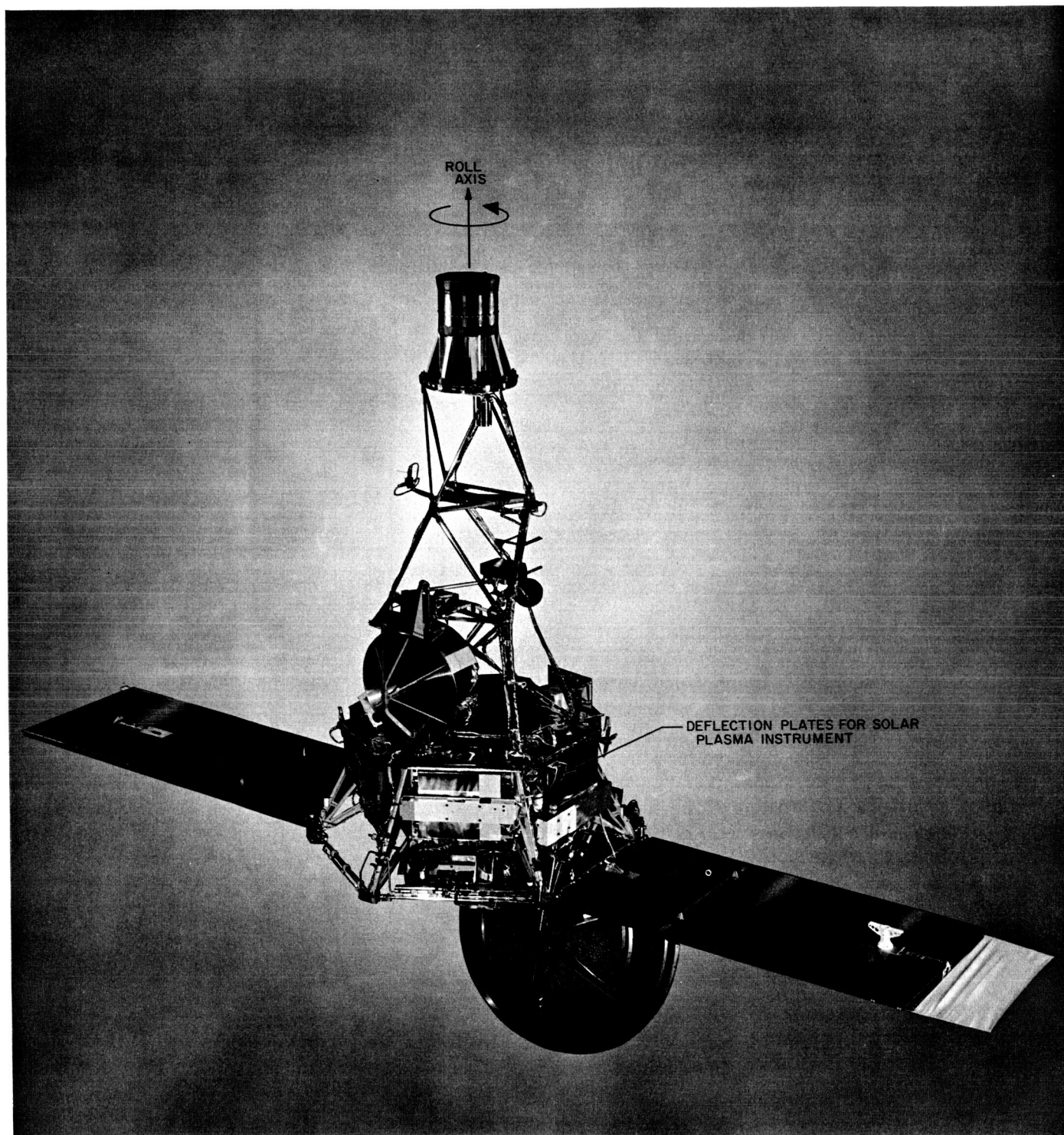
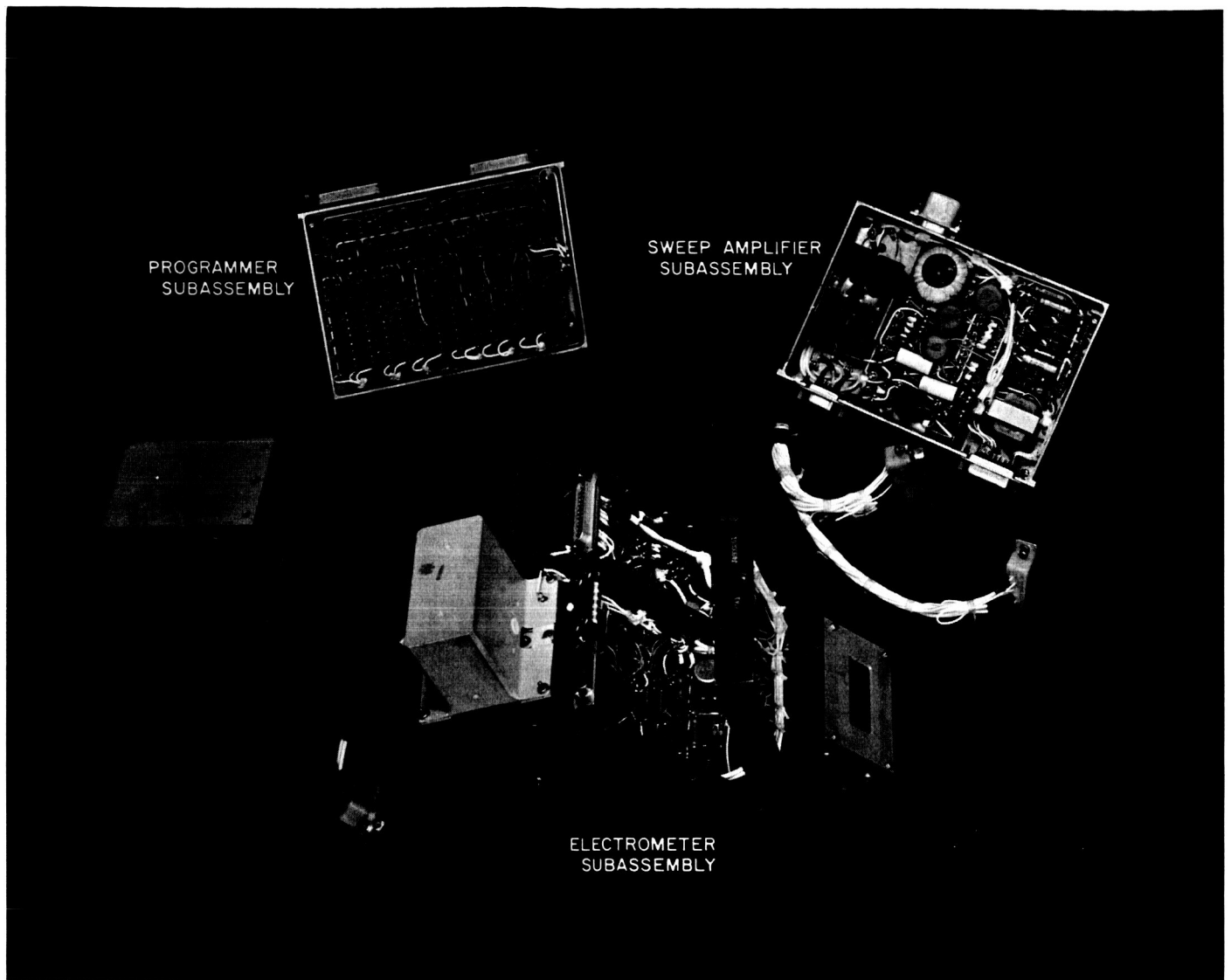


Fig. 7. *Mariner 2* spacecraft



**Fig. 8. Mariner 2 solar plasma instrument**

### III. THE ELECTROMETER SYSTEM

The basic form chosen for the electrometer system is the conventional operational amplifier configuration. The usual high-gain inverting amplifier is present but with certain external differences. The feedback element, usually a single resistor, in this case contains a more complex nonlinear circuit. The input resistor of the operational amplifier and its associated voltage source are replaced, in this application, by a current source of virtually infinite impedance. This amplifier configuration is popular in electrometer measurements because the small input (or summing-point) potential and small variations thereof minimize effects of input leakage resistance. Similarly, effects of input-to-ground capacitance upon the speed of response are also minimized.

The carrier-amplifier approach was pursued because input-modulating comparators of the dynamic capacitor variety offered such attractive prospects as high resistance, stability, and long life expectancy. Furthermore, if the modulator parameters were properly chosen, the need for a vacuum-tube input to the carrier amplifier would be eliminated. In addition, if the modulator frequency were made sufficiently high, the electrometer speed of response would not be severely limited by amplifier bandwidth, which would also be commensurately higher.

The choice of a nonlinear thermionic device for the principal feedback element was influenced by such considerations as dynamic range, simplicity, and familiarity. The dynamic current range requested by the experimenters was 7 decades—between  $10^{-13}$  and  $10^{-6}$  amp. The dynamic voltage range of the amplifier was forecast to be about 3 decades, limited at the high end by power supply voltage and at the low end by amplifier stability and the accuracy of analog-to-digital conversion. The more complex, though nonetheless appealing, technique of automatic switching of feedback resistors could not be used in view of project exigencies.

The stability of the static characteristic of the amplifier-compressor system was then realized to be primarily a function of the stability of the feedback tube. Regardless of this masking effect, the development of the capacitive modulator-stabilized amplifier was considered thoroughly worthwhile. The availability of a reliable modulator-amplifier combination would fulfill that perennial requirement for a system capable of providing low-threshold, fast, accurate, and long-lived measurements.

#### A. The Logarithmic Compressor

One of the simplest and most usable of nonlinear vacuum-tube devices is the logarithmic diode. This section of the Report describes two innovations to standard applications of logarithmic diodes as follows:

1. Emission stabilization by use of a low-voltage filament-current regulator.
2. Connection of two diodes and a battery, or its equivalent, in such a manner as to produce two distinguishable logarithmic calibration segments, i.e., one segment each for positive- and negative-polarity currents.

##### 1. Unipolar Circuit

One of the simplest and most usable of nonlinear vacuum-tube devices is the logarithmic diode. If the voltage  $V_p$  on the diode shown in Fig. 9 were set at zero by shorting the plate to the ground-referenced side of the filamentary cathode, a current  $I_0$  would flow. This initial-velocity electron current decreases upon the application of a negative plate voltage. For this reason the second-quadrant portion of the characteristic shown in Fig. 9 is sometimes called the retarding field region. A number of subminiature electrometer tubes were inspected in this region, many of which displayed almost flawless exponential characteristics of the form  $I_p = I_0 e^{aV_p}$  below  $I_0$ . Many of the  $I_0$ 's were in the range of  $10^{-5}$  to  $10^{-6}$  amp. The CK5886 subminiature pentode, a veritable work-horse of electrometer applications, was chosen, and both screen and control grids were tied to the plate

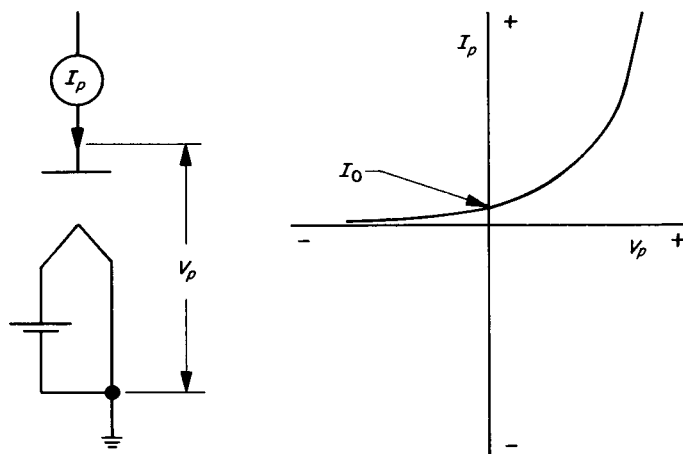


Fig. 9. Thermionic diode and associated characteristic

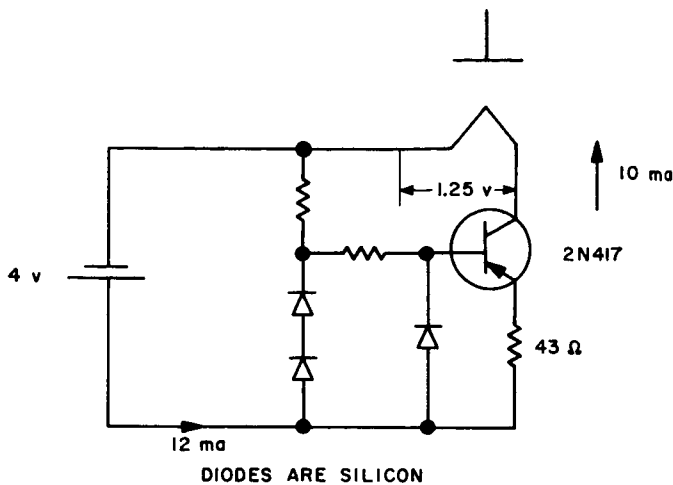


Fig. 10. Filament current regulator

to produce a diode connection. Extensive tube evaluations conducted under varying temperatures soon confirmed the desirability of having filament emission controlled with a constant-current regulator. This circuit, as shown in Fig. 10, affords low-voltage current regulation usually not available with series voltage-dropping resistors. An important feature of the regulator is that the emitter diode voltage of the germanium transistor is small enough compared with the drop across the adjacent silicon diode to permit inclusion of an important degeneration resistor in the transistor circuit. Probably more important still is the temperature tracking of the emitter diode and silicon diode voltages. The circuit has a current regulation of approximately 2% over a  $-10$  to  $+75^{\circ}\text{C}$  temperature range. Its regulation is such that current variations are 8% of input voltage variations at the nominal 4 v. Regulator performance is shown in Table 4.

During preliminary tube evaluation it was observed that drifts in plate voltage under conditions of constant plate current, but varying filament current, were often as much as three times smaller when measured with respect to the negative side of the filament than when measured with respect to the positive side. This effect, though not fully understood, is the principal reason for referencing the nonstandard negative side of the filament. Connecting the same vacuum tube in its triode configuration makes it far less sensitive to cathode temperature changes (Ref. 13). The triode, however, is sensitive to plate voltage variations. The sensitivity of plate current to plate voltage variations for a CK5889 may be shown to be approximately 0.1 decade/1% change in  $V_p$  when

$$I_{in} = 10^{-10} \text{ amp}$$

Table 4. Performance of filament current regulator

Battery voltage, v	$I_f$ , ma		
	At $+25^{\circ}\text{C}$	At $-10^{\circ}\text{C}$	At $+75^{\circ}\text{C}$
4.0	10.15	10.10	10.30
3.5	10.07	10.03	10.10
3.0	9.95	9.87	10.00
2.5	9.70	9.69	9.80
2.0	9.60	9.47	9.65

and

$$V_p = 5.2 \text{ v.}$$

Although the comparison is not exact, a similar tube, the CK5886 connected as a diode, produces the following filament-induced variation: 0.05 decade/1% change in  $I_f$  when

$$I_{in} = 10^{-8} \text{ amp}$$

and

$$I_f = 10 \text{ ma.}$$

The diode connection was selected because of its 2-terminal character and its consequent amenability to being used in the feedback leg of a fast operational amplifier. The filament current regulator, in addition, reduced variations in the static characteristics of the CK5886 tube to an acceptably low level.

## 2. Bipolar Circuit

If it is desirable to measure currents of both polarities over similarly wide ranges, the notion of using two logarithmic diodes in opposing directions becomes very appealing. Consider what happens when two diodes are connected back-to-back, i.e., plate 1 to filament 2; plate 2 to filament 1. To satisfy the loop voltage equation, both plate voltages should be equal and of opposite polarity ( $V_{p1} = -V_{p2}$ ). In the case of tubes having identical characteristics, the plate voltages become zero. For closely matched tubes, the circulating current will therefore be close to  $I_0$ , a value large enough to mask the effects of smaller external input currents. When it becomes necessary to reduce the circulating current, a biasing arrangement such as that shown in Fig. 11 may be used. The dc voltage  $V_B$  may then be made large enough to reduce the circulating current  $i_c$  to a value equal to or less than the threshold input current. The resultant characteris-



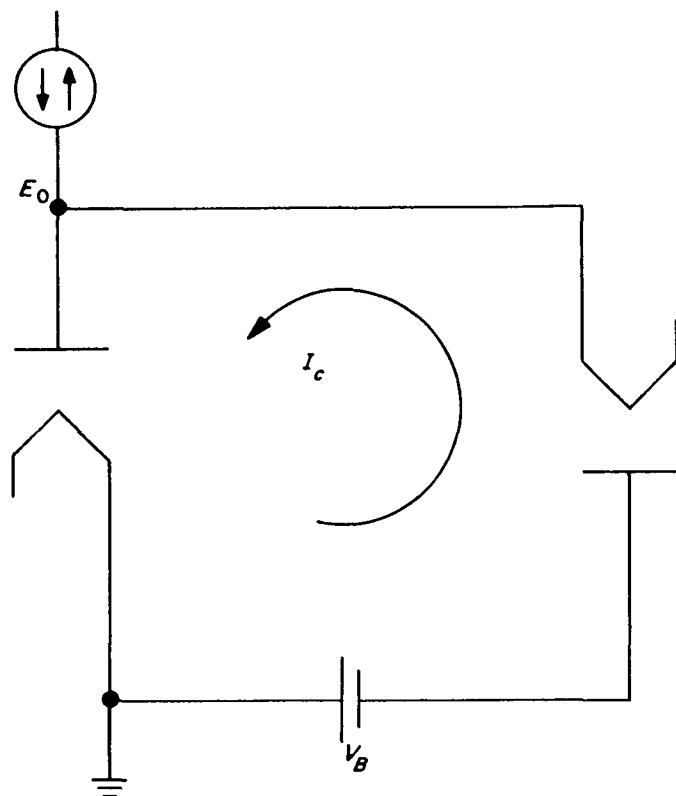


Fig. 11. Bipolar logarithmic current-to-voltage compressor

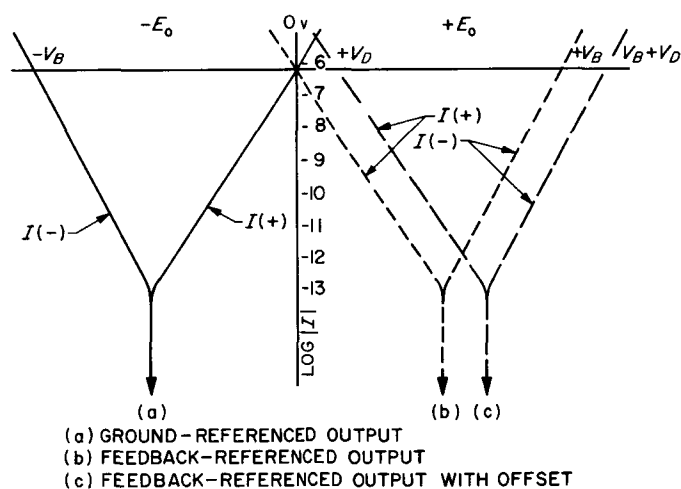


Fig. 12. Bipolar logarithmic characteristics

tic, as shown in Fig. 12a, would be produced with  $V_B = 3.75$  where both tubes have representative semilog slopes of 250 mv per current decade and  $I_0$ 's of  $10^{-6}$  amp.

To adapt this circuit to the form used on the *Ranger*, the circuit of Fig. 11 was transposed so that the input

node was connected to the summing point of the inverting dc electrometer amplifier, and the formerly grounded connection was connected to the amplifier output. An ideal amplifier having zero drift, infinitesimal error potential, and zero input leakage, among other qualities, would force the input current through the feedback circuit and as a consequence produce an output characteristic (Fig. 12b) that was a mirror image of the original (Fig. 12a). To remain safely within the sampling range of the analog-to-digital converter that followed the amplifier, a small translational offset  $V_D$  was inserted. The electrometer system with the feedback arrangement as used on the *Ranger* is shown in Fig. 13 and the corresponding translated curves are shown in Fig. 12c.

The filament supply was the most formidable problem connected with the logarithmic electron-current measurement. Although identical regulators were used, the transformer-rectifier supply used on the filament near the amplifier output could not be used for the filament at the input. For reasons of dc and ac isolation, a conventional insulated mercury-cell battery pack was used for the input filament of each of the two adjacent electrometers that appeared in each assembly. Each battery pack, capable of delivering two separate 50-mw loads for about 700 hr, weighed 3 lb. The penalties paid for the range and simplicity of this electron measurement

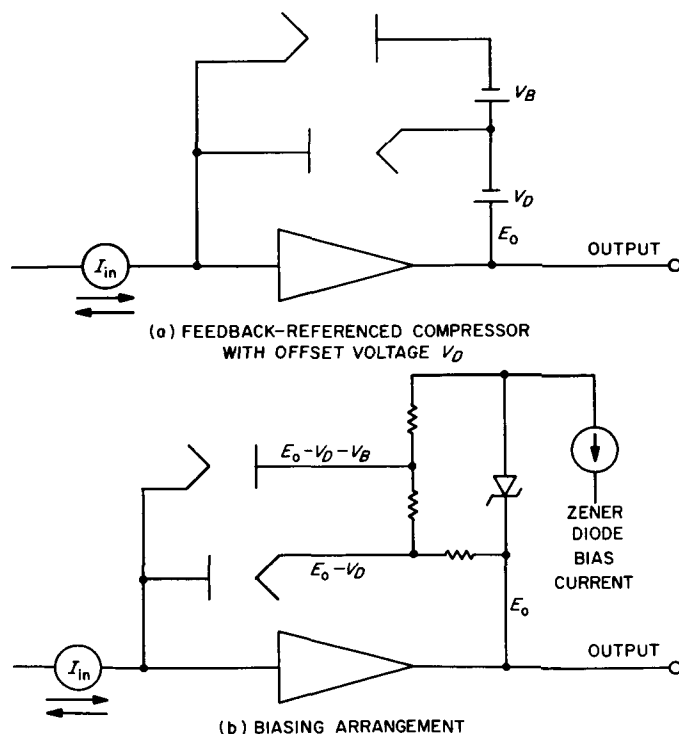


Fig. 13. Bipolar logarithmic electrometer

were in the weight of the battery pack and in the reduced prelaunch operational replacement flexibility.

### 3. Dynamic Equivalent Circuit

An important exercise for circuit applications is the exposition of an equivalent network representing an accurate dynamic model of the logarithmic diode. This network enters into calculations for electrometer speed of response and into the formulation of feedback polynomials used in the determination of closed-loop stability.

A good approximation to the characteristic produced by the diode used in the logarithmic compressor is (Ref. 14)

$$I_p = I e^{(q/KT)(V_p + E_c)} \quad (1)$$

where

$I_p$  = plate current

$I$  = total emission current

$V_p$  = plate-to-filament voltage

$E_c$  = contact potential

$q$  = electron charge

$K$  = Boltzmann constant.

Both  $E_c$  and  $I$  may be omitted by reintroducing  $I_0$  as the plate current at zero plate voltage (since the relation does hold for this tube):

$$I_p = I_0 e^{(qV_p/KT)} \quad (2)$$

or

$$V_p = \frac{KT}{q} \ln \frac{I_p}{I_0}. \quad (3)$$

The resistance of the diode may be written

$$r_D = \frac{dV_p}{dI_p} = \frac{KT}{qI_p}. \quad (4a)$$

The slope of the semilog characteristic may be written

$$M = \frac{q}{KT} = \frac{\ln(I_p/I_0)}{V_p} = \frac{\ln(I_{p_1}/I_{p_2})}{V_{p_1} - V_{p_2}}.$$

Most of the 5886 diodes operating at filament currents of 10 ma displayed characteristics having about 230 mv per current decade. Applying this information, accordingly, to the last equation,

$$M = \frac{\ln 10}{0.230} = 10.$$

Using this approximation, the resistance may be written

$$r_D = \frac{1}{10 I_p}. \quad (4b)$$

This expression is valid so long as the input current is static or varies slowly. If input current fluctuates rapidly, the equivalent instantaneous plate current will be different owing to interelectrode capacitance effects as suggested in Fig. 14. Lower-case terms are used here to denote transient or dynamic values of current, in which case  $i_p$  and  $i_{in}$  are not necessarily equal on an instantaneous basis and may conceivably be of opposite polarity.

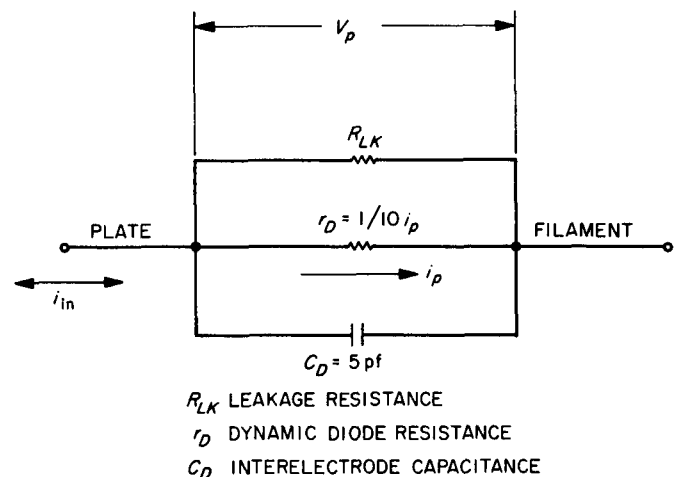


Fig. 14. Dynamic equivalent circuit of a logarithmic diode

Effects of expected extremes in ambient or mounting temperature (273 to 343°K) are attenuated to a good degree by a comparatively stable and high filament temperature (1260°K as calculated from the expression  $T = q/KM$ ).

### B. The Electrometer Amplifier

Since the instrument that was flown on *Mariner 2* was a refined version of the *Ranger* instrument, the

discussion in this Section will bear mainly on the electrometer amplifier used in the *Mariner 2* solar plasma instrument (see Fig. 15).

### 1. Detailed Description

If the main feedback loop is inspected in a counter-clockwise direction starting at the input, the first element of interest is the dynamic capacitor assembly. This modulator was developed for JPL through a series of contracts with the Applied Physics Corporation of Monrovia, California. The device is mechanically resonant near 2,400 cps ( $Q_m \cong 200$ ) and is driven at this resonance by a tuned Class C amplifier (Ref. 15). The capacitor-drive oscillator loop is completed with a lead titanate vibration transducer, which is affixed to the vibrating reed element. Following the modulator are a one-stage low-noise ac preamplifier and a 3-stage ac postamplifier. The carrier signal is then half-wave demodulated with a transistor switch. Direct-coupled amplification and filtering are performed by a 4-stage Miller-type filter amplifier. The

loop is then closed with a single logarithmic diode and its associated 10-ma current regulator. An offset voltage used in the flight instrument is not shown in the block diagram of Fig. 15.

Since the dynamic resistance of the feedback element may vary as many orders of magnitude as may the measurable input current, it was decided to augment the main loop with a secondary loop for purposes of nonlinear damping. The notion of an efficient single linear network correction for fast, stable operation in this system over a 7-decade current range still remains a pleasant fantasy.

A comparator that is referenced at a pre-saturation voltage has been provided to preclude saturation of the amplifier, an event that could occur in the presence of small negative background currents. When this reference level has been exceeded, an input current source, which doubles as a calibration current, is activated, thereby bringing the electrometer to a midrange voltage.

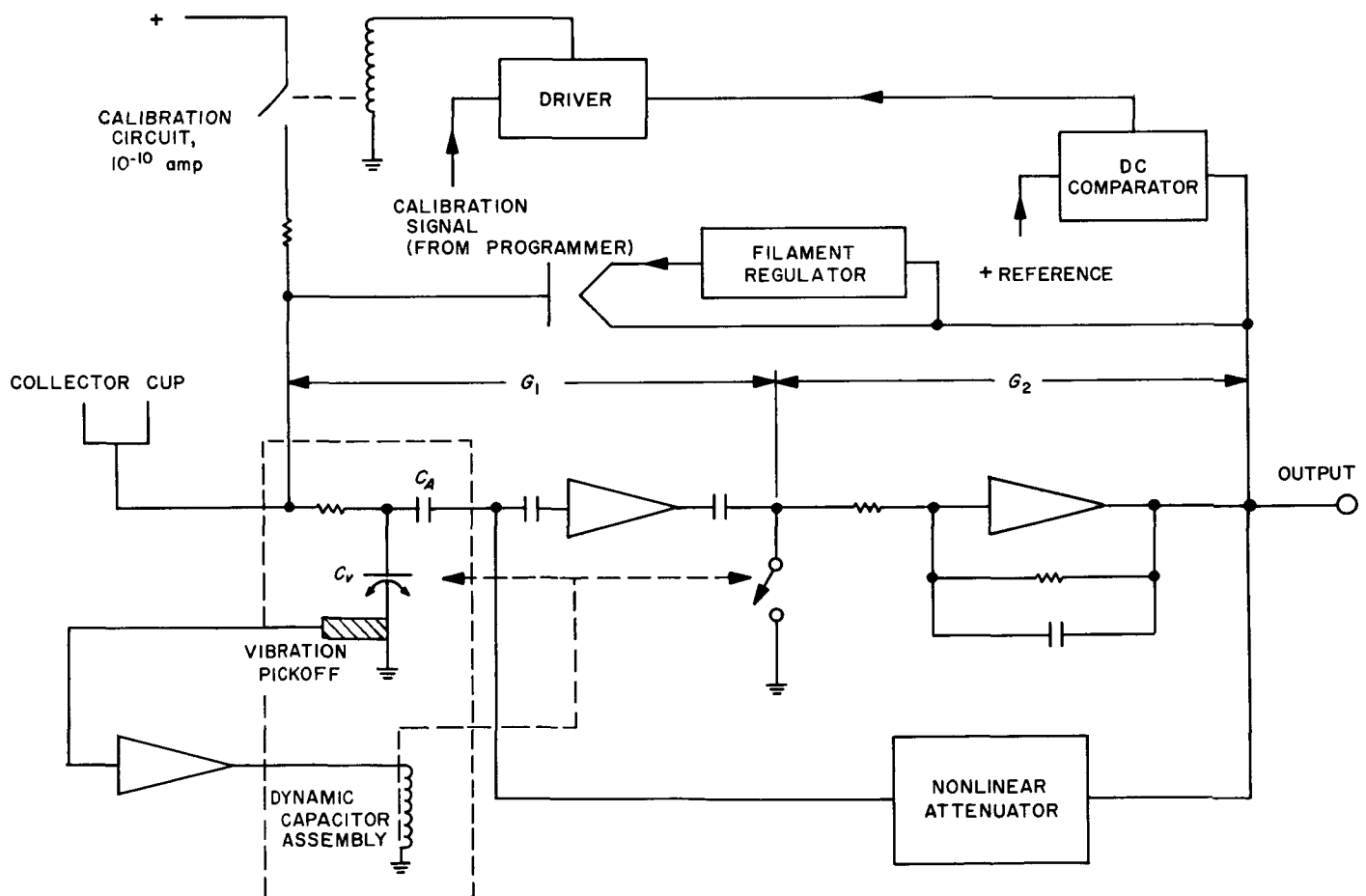


Fig. 15. *Mariner 2* electrometer block diagram

## 2. Design Choices

A figure of 1,000 was selected as the requirement for dc gain between the input and the output. If one neglects the effects of leakage current and resistance, the figure of 1,000 becomes the dc feedback factor. This standard of amplifier tightness limits dynamic deviations to 0.1% of the output as obtained with infinite gain.

The portion of this over-all gain incorporated into the carrier section was determined principally by considerations of noise and dc stability. The gain had to be made large enough to adequately minimize the effects of drifts in the demodulator baseline and the dc amplifier as seen at the electrometer input, but not so large as to permit input noise to drive the output stage of the ac amplifier into nonlinear operation. A representative gain of 35 for  $G_1$  (see Fig. 15) reduced drifts from the dc section to the order of 1 mv as observed at the electrometer input. Noise at the output of the ac amplifier was about 100 mv rms within a linear dynamic capability of +2.5 and -6 v.

Since the transformer-rectifier power supply for the instrument was driven by a 50-v, 2,400-cps, square-wave source, it was certain that at least small amounts of 2,400-cps energy would be present in the carrier amplifier. The *Ranger* modulator was driven at the spacecraft power frequency, also 2,400 cps, and the ac amplifier, which was designed accordingly, was retained for the *Mariner* electrometer. The self-resonant dynamic capacitors used for *Mariner* were, therefore, ordered with mechanical resonances sufficiently displaced from 2,400 cps as to minimize internal beat-frequency signals.

The ac preamplifier presented one of the most likely areas for innovation. The question was whether the parameters of the customary vacuum-tube preamplifier could be replaced by those of a transistor. The number of stages needed for the carrier section turned out to be about the same both for a high-input impedance bootstrapped amplifier and for conventional low-input impedance common-emitter amplifiers. The low-impedance connection, as embodied in the circuit of Q1 in Fig. 16, was finally used. This circuit, as one might suspect, predated the commercial availability of field-effect transistors. The current gain of the carrier amplifier was significantly increased by a current step-up transformer ( $n = 14:1$ ) interposed between the preamplifier and the dynamic capacitor. The primary impedance, which was  $n^2$  times the amplifier input impedance, was still relatively small compared with the capacitive source reactance of the dynamic capacitor. A phase-stable current gain of

14 could, therefore, be expected without increasing the noise component at the output of the carrier amplifier. Several germanium and silicon transistors were inspected in unloaded models of the preamplifier. The 2,400-cps gains of this highly degenerative circuit were experimentally confirmed to be equal, and then the output noise content was inspected. The germanium 2N417 was selected for the application because of its superior noise performance as observed through this empirical procedure. The chief safeguard against high-temperature saturation of the transistor caused by collector leakage is the diode CR2, whose  $I_{co}$  characteristic is matched to that of the transistor to at least 70°C. The preamplifier bias configuration presented an optimum thermal stability ( $S_{I_c} = 1$ ) along with reduced gain to  $1/f$  noise.

All amplifier elements within the main loop contained some local feedback. The oscillator that drove the dynamic capacitor, in fact, had a temperature-sensitive amplitude variation designed to maintain a more constant modulation conversion efficiency than would ordinarily be obtained with a constant drive voltage.

## 3. Gain

*a. Carrier Amplifier.* The first element entering into the gain equation for the carrier section is the dynamic capacitance ( $C_v$  in Fig. 17). Briefly reviewing the theory of operation of this modulator (Ref. 16), consider the elements  $V_{in}$ , R2, and the dynamic capacitor as shown in Fig. 18a, with the output of  $C_v$  open-circuited in this example. Treating the capacitor as a parallel-plate device, its value may be written

$$C_v = \frac{\epsilon_0 A}{d} \quad (5)$$

where

$A$  = area

$d$  = separation between plates

$\epsilon_0$  = dielectric constant of free space.

If one of the plates is sinusoidally driven at a frequency  $f$  such that its separation from the other plate is

$$d = d_0 [1 + (\Delta d/d_0) \sin \omega t], \quad (6)$$

the varying capacitance may then be expressed

$$C_v = \frac{\epsilon_0 A}{d_0 [1 + (\Delta d/d_0) \sin \omega t]} = \frac{C_0}{[1 + (\Delta d/d_0) \sin \omega t]} \quad (7)$$

where  $C_0$  is the rest capacitance. In the general case where

$$R_2 C_0 \gg 1/\omega$$

a constant charge

$$Q_0 = V_{in} C_0 \quad (8)$$

is built up across the capacitor,  $C_v$ . The combined average, plus modulation voltage produced, is given by

$$\begin{aligned} V &= \frac{Q_0}{C_v} = \frac{V_{in} C_0 [1 + (\Delta d/d_0) \sin \omega t]}{C_v} \\ &= V_{in} [1 + (\Delta d/d_0) \sin \omega t] . \end{aligned} \quad (9)$$

The conversion efficiency  $\eta_c$  is the figure of merit describing the efficiency of dc-to-ac conversion and is defined as follows:

$$\eta_c = \frac{V_{rms \text{ (open circuit)}}}{V_{in \text{ (dc)}}} = \frac{\Delta d}{d_0} \frac{\sqrt{2}}{2} . \quad (10)$$

Representative parameters and component values for the *Mariner 2*-type modulators are as follows:

$$C_0 = 50 \text{ pf}$$

$$C_A = 70 \text{ pf}$$

$$\eta_c = 10\%$$

and

$$f_0 = 2,350 \text{ cps}$$

where  $C_A$  is a high-quality vacuum dielectric capacitor built into the modulator assembly, and  $f_0$  is the mechanical resonant frequency at which the reed is driven.

An ac approximation to the dynamic capacitor circuit, shown in Fig. 18b, replaces the dc source  $V_{in}$  with the ac generator  $\eta_c V_{in}$ , and replaces the nonlinear  $C_v$  with a source capacitance  $C_0$ . The feedback resistor  $R_{12}$  provides degeneration in the preamplifier and at the same time presents a suitably small termination to the transformer secondary. The nominal impedances of the transformer are 200 K and 1 K for the primary and secondary, respectively. The secondary impedance as shown by the Miller equivalent in Fig. 18b and c is indeed about 1 K. Under actual conditions when the preamplifier is loaded

by the "Triplet" ac amplifier, the impedance may rise from 1 K to about 2.5 K with a small amount of reactive detuning present. Neglecting the effect of  $R_2$ , the open-circuit preamplifier output voltage  $E_{1(oc)}$  may now be calculated from the circuit of Fig. 18c. In this circuit, the source impedance in ohms is given by

$$X_g = X_0 + X_A + X_2 = 2.64 \times 10^6$$

where

$$X_0 = 1.36 \times 10^6$$

$$X_A = 0.97 \times 10^6$$

$$X_2 = 0.31 \times 10^6 \quad (C_2 = 220 \text{ pf})$$

and the primary input impedance is given by

$$R_p \cong 0.2 \times 10^6 .$$

The primary current,  $i_1$ , is given approximately by

$$i_1 = \frac{\eta_c V_{in}}{-j X_g} .$$

Therefore

$$v_s = \frac{i_1 n R_{12}}{(1 - A_1)} = \frac{\eta_c V_{in}}{-j X_g} \frac{n R_{12}}{1 - A_1}$$

and

$$E_{1(oc)} = \frac{\eta_c V_{in} n R_{12}}{-j X_g} \frac{A_1}{1 - A_1} . \quad (11)$$

According to the equation

$$\left| \frac{E_{1(oc)}}{\eta_c V_{in}} \right| \cong \frac{n R_{12}}{X_g}$$

the gain at 2,350 cps is calculated to be 0.25. In a test performed on the circuit of Fig. 18, the dynamic capacitor assembly was replaced by a 27-pf series capacitor, and a generator simulating the signal  $\eta_c V_{in}$  was connected to the input. The gain of this circuit vs. the frequency is shown in Fig. 19. The output impedance of the preamplifier was measured to be 5 K at 2,350 cps.

The triplet amplifier is a 3-stage, direct-coupled, feedback-biased cascade. At the carrier frequency, a substantial portion of the feedback used to bias the

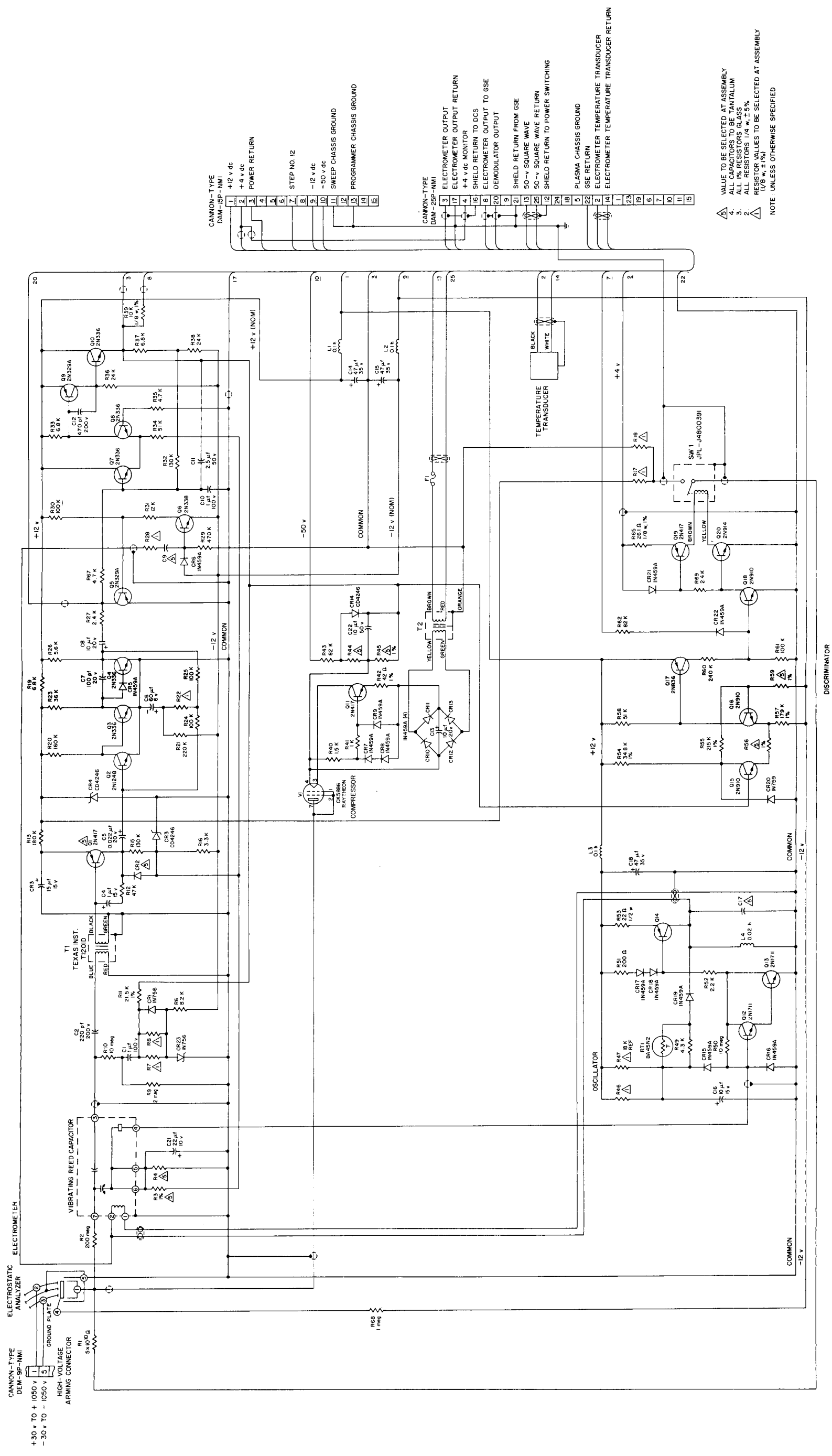


Fig. 16. Mariner 2 electrometer schematic diagram

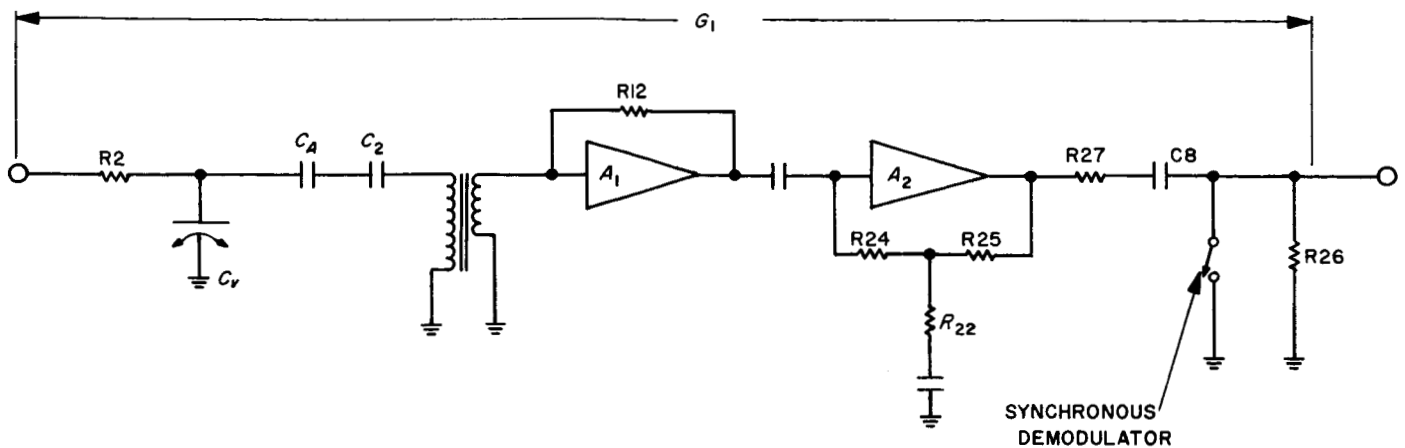


Fig. 17. Simplified diagram of carrier section

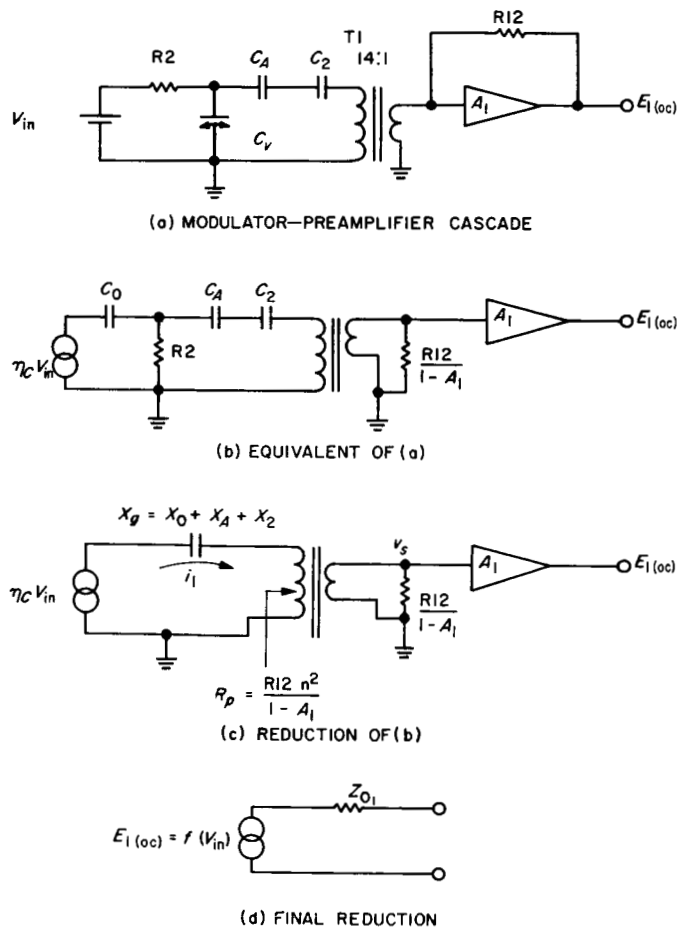


Fig. 18. Reduction of modulator-preamplifier cascade to Thevenin equivalent circuit

amplifier at dc is disconnected by the shunt capacitor C6. The resultant circuit is shown in Fig. 20, together with its equivalent driving source.

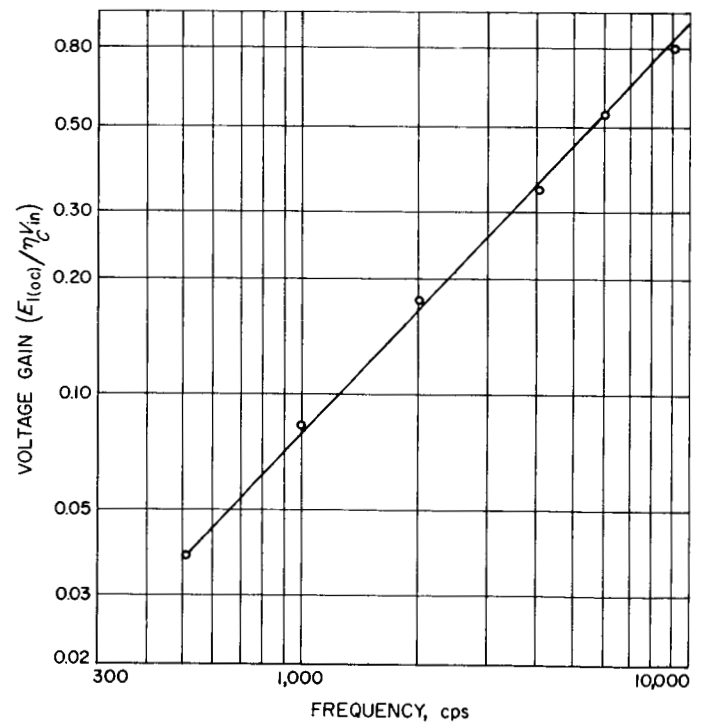


Fig. 19. Plot of preamplifier gain vs. frequency

The gain of an operational amplifier may be expressed in the following general form:

$$K = K_i \left( \frac{A\beta}{1 - A\beta} \right) \quad (12)$$

where

$\beta$  = portion of output returned to summing point

$A\beta$  = feedback factor

$-K_i$  = closed-loop gain with infinite feedback factor.

In the circuit of Fig. 20a

$$K_i = \frac{R_{24} R_{25} + R_{24} R_{22} + R_{25} R_{22}}{Z_{o1} R_{22}}. \quad (13)$$

Using circuit values of

$$R_{24} = R_{25} = 10^5 \Omega$$

$$R_{22} = 220 \Omega$$

$$Z_{o1} = 5 \times 10^3 \text{ at } 2,350 \text{ cps}$$

$$A_2 = -25 \times 10^3$$

and

$$Z_{in} = 15 \times 10^3 \Omega$$

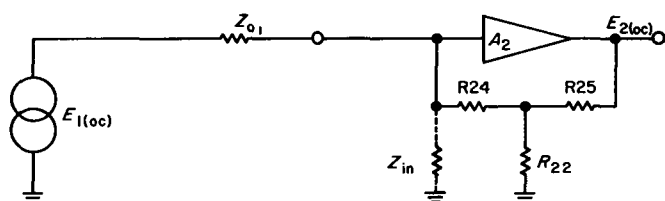
(both  $Z_{o1}$  and  $Z_{in}$  are considered resistive), one obtains

$$K_i = 9.1 \times 10^3$$

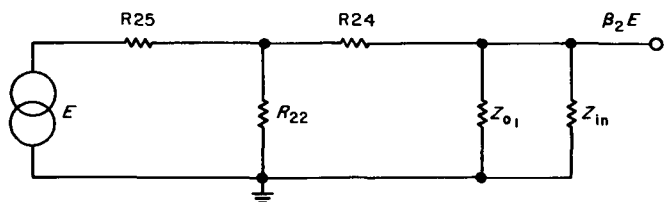
$$\beta_2 = 8.25 \times 10^{-5}$$

and

$$A_2 \beta_2 = -2.06.$$



(a) MIDBAND EQUIVALENT CIRCUIT



(b)  $\beta$  NETWORK FOR LOOP TRANSMISSION EQUATION

Fig. 20. Triplet amplifier

If  $A_2 \beta_2$  contained no phase shift, the triplet gain, as determined from Eq. (12), would be  $6.14 \times 10^3$ . Comparisons of measured and calculated values for carrier gains at 2,350 cps are shown in the following table.

Element	Calculated gain	Measured gain
Preamplifier	0.25	0.20
Triplet amplifier	$6.14 \times 10^3$	$5.2 \times 10^3$
Cascade	1,540	910

Response of the entire cascade with respect to frequency is shown in Fig. 21. The low-frequency slope of 12 db/octave is composed of two equal contributions: one 6-db/octave rate from the capacitive source reactance to the transformer and another similar effect from

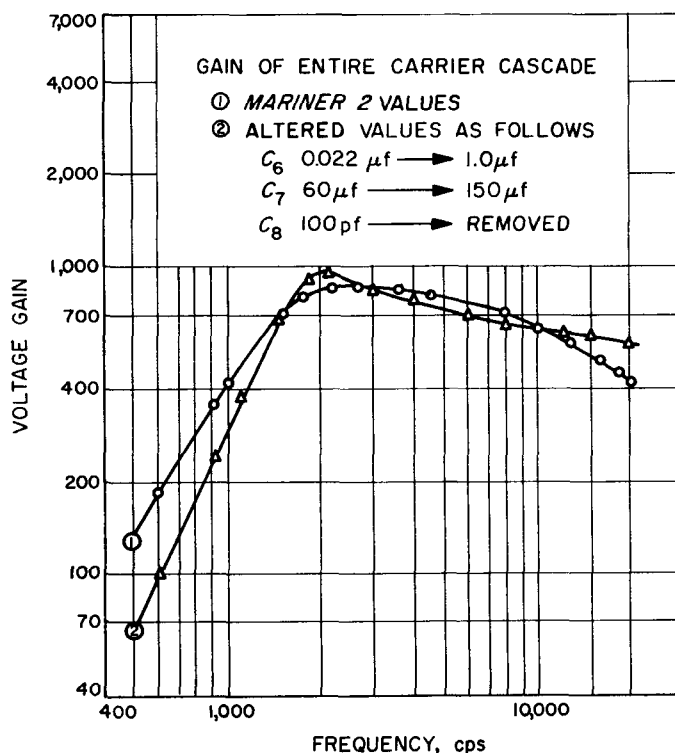


Fig. 21. Carrier amplifier performance curves

the network coupling the preamplifier and the triplet. If the preamplifier output impedance  $Z_{o1}$  were constant, one might expect a characteristic that would still be rising 6 db/octave at the carrier frequency. This impedance, because it is affected by the preamplifier source impedance, is actually rising with frequency at 2,350 cps and is the principal cause of flattening as seen in Fig. 21.



**b. Demodulator.** The ac signal from the carrier amplifier is reconverted to dc by means of synchronous detection. The signal  $E_{in}$  in the equivalent circuit of Fig. 22 represents the open-circuit output voltage of the triplet amplifier. The series element  $R_1$  is a composite of R27 (see Fig. 16) and the output resistance of the triplet amplifier. The synchronous switching in this example is performed by the transistor Q5 while R67, the input resistor to the dc filter amplifier, is closely approximated in the equivalent circuit by the ground-connected R2. The physical series resistor that is part of  $R_1$  must be made large enough to limit the maximum chopped currents in the shunt switch ( $i_a$  in Fig. 22c) and prevent the triplet amplifier from cutting off on its positive swing. On the other hand, this resistor must not be made so large as to seriously attenuate the signal to the dc amplifier. Interposition of a voltage step-up transformer between the triplet and the demodulator would have the effect of multiplying the component of  $R_1$  due to triplet output resistance by the square of the turns ratio. To preserve high detection efficiencies it then becomes necessary to

elevate the impedance levels in the amplifier following the demodulator.

Maximum detection efficiency is produced at drive-to-signal phasings of 0 and 180 deg. At intermediate phasings, efficiencies are described by the cosine of the drive-signal phase angle. Two important aspects of demodulator performance that will be discussed here are the efficiency and the low-pass frequency response of the idealized capacitor-coupled demodulator as characterized by the circuit of Fig. 22a. In both cases a 180-deg chopping duration, phased for maximum efficiency, will be assumed.

The output developed across the synchronous switch is made up of two components, signal and pedestal, both of which are attenuated by the factor  $R_2/(R_1 + R_2)$ . The pedestal is attributable to a dc voltage retained by the coupling capacitor as though it were the output filter of a rectifier system.

To determine the value of the output pedestal and finally of the aggregate output, it is first necessary to determine the steady-state voltage developed across the capacitor. The voltage across the capacitor,  $v_c$ , at the end of one cycle of signal demodulation may be written

$$v_c = v_{c_1} + \frac{1}{C} \int_0^{\frac{\pi}{\omega}} i_a dt + \frac{1}{C} \int_{\frac{\pi}{\omega}}^{2\pi/\omega} i_b dt \quad (14)$$

where

$v_{c_1}$  = capacitor voltage at start of cycle

$i_a$  = capacitor current during switch closure

$$= \frac{E_p \sin \omega t - v_{c_1}}{R_1}$$

$i_b$  = capacitor current during switch opening

$$= \frac{E_p \sin \omega t - v_{c_1}}{R_1 + R_2}$$

The assumption made in writing the current equations is that  $v_c$  does not significantly change its value during the cycle. If the system has reached equilibrium,  $v_c$  must

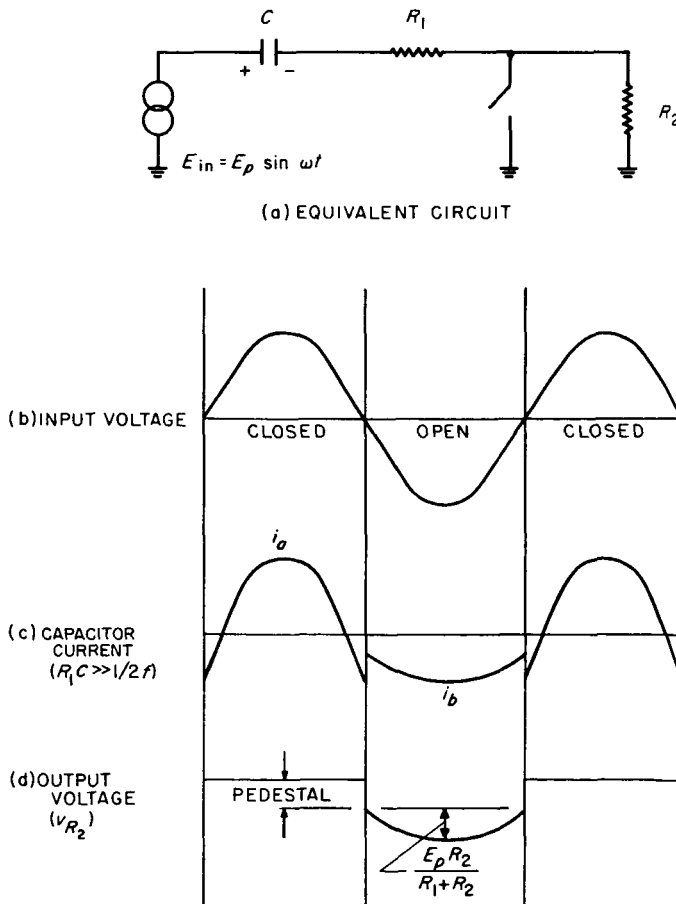


Fig. 22. Demodulator and associated waveforms

equal  $v_{c_1}$  at the end of the cycle, and Eq. (14) may be rewritten and

$$\Delta v_c = \int_0^{\frac{\pi}{\omega}} i_a dt + \int_{\frac{\pi}{\omega}}^{\frac{2\pi}{\omega}} i_b dt = 0. \quad (15)$$

Substituting  $i_a$  and  $i_b$  in Eq. (15) and integrating, the steady-state capacitor voltage  $v_{c_1}$  may be written

$$v_{c_1} = \frac{2E_p}{\pi} \left[ \frac{R_2}{2R_1 + R_2} \right]. \quad (16)$$

The average full-cycle output voltage may then be determined by adding the average half-cycle pedestal and signal voltages, dividing by 2, and multiplying by the resistive attenuation as follows:

$$\begin{aligned} v_{R_2} &= \frac{1}{2} \left( \frac{R_2}{R_1 + R_2} \right) \left[ \frac{2E_p}{\pi} \left( \frac{R_2}{2R_1 + R_2} \right) + \frac{2E_p}{\pi} \right] \\ &= \frac{2E_p}{\pi} \frac{R_2}{2R_1 + R_2}. \end{aligned} \quad (17)$$

Since input modulation efficiency was described as the ratio of rms voltage to dc input voltage (Eq. 10), it becomes convenient in completing the gain calculation for the carrier section to define the demodulation efficiency  $\eta_D$  in inverse terms, i.e.,

$$\begin{aligned} \eta_D &= \frac{v_{R_2}(\text{avg})}{E_{in}(\text{rms})} \\ &= \frac{2}{\pi} \sqrt{2} \frac{R_2}{(2R_1 + R_2)} \\ &= \frac{0.9 R_2}{2R_1 + R_2}. \end{aligned} \quad (18)$$

In the circuit of Fig. 16

$$\begin{aligned} R_2 &= R_{67} = 4.7 \text{ K} \\ R_1 &\cong R_{27} + \frac{R_{26}}{1 - A_2 \beta_2} \\ &= 2.4 \text{ K} + \frac{5.6 \text{ K}}{3.06} = 4.2 \text{ K} \end{aligned}$$

$$\eta_D = 32.4\%.$$

The dc voltage gain of the entire carrier section may then be written

$$G_1 = \eta_C G_{AC} \eta_D. \quad (19)$$

The laboratory model on which many of these tests were run, like the flight electrometers, had its carrier gain adjusted with  $R_{22}$  to a nominal value of 35. Using the measured value of  $G_{AC}$  (910) and the calculated value of  $\eta_D$  for the sake of illustration, the dynamic capacitor conversion efficiency producing the requisite gain of 35 is calculated to be 12%.

It is interesting to note that when a signal suddenly appears at the output of the triplet amplifier, only the signal component is transmitted at first. The pedestal component, however, builds up in accordance with the charging of the capacitor. The effect on the carrier envelope or on the average demodulated signal, in a low-pass sense, is that of a network producing a phase-lag doublet. This variation of  $\eta_D$  vs. frequency and the attendant low-pass phase shifts are discussed in the following paragraphs.

The general expression for incremental capacitor voltage in a system that has not reached equilibrium is given in Eq. (15), except that  $\Delta v_c$  is not zero. Substituting  $i_a$  and  $i_b$  in Eq. (15), the incremental buildup across the capacitor during one cycle may be written

$$\begin{aligned} \Delta v_c &= \frac{-v_{c_1} \pi}{\omega C} \left[ \frac{1}{R_1} + \frac{1}{R_1 + R_2} \right] \\ &\quad + \frac{2E_p}{\omega C} \left[ \frac{1}{R_1} - \frac{1}{R_1 + R_2} \right] \text{ volts/period} \end{aligned} \quad (20)$$

or

$$\begin{aligned} \frac{\Delta v_c}{\Delta t} &= \frac{-v_{c_1}}{2C} \left( \frac{2R_1 + R_2}{R_1(R_1 + R_2)} \right) \\ &\quad + \frac{E_p}{\pi C} \left[ \frac{R_2}{R_1(R_1 + R_2)} \right] \text{ volts/second.} \end{aligned} \quad (21)$$

If the time required for the capacitor voltage to build up is long compared with a carrier signal period, Eq. (21) may be written in the following differential form:

$$\frac{dv_c}{dt} = \frac{-v_c}{2CR_A} + \frac{E_p}{\pi CR_B} \quad (22)$$

where

$v_c$  = capacitor voltage at  $t$  sec after introduction of a sine wave signal having a peak voltage  $E_p$

$$R_A = \frac{R_1(R_1 + R_2)}{2R_1 + R_2}$$

$$R_B = \frac{R_1(R_1 + R_2)}{R_2}$$

Rewriting Eq. (22) in operational form,

$$pv_c(p) + \frac{1}{2R_A C} v_c(p) = \frac{E_p}{p \pi R_B C}$$

and

$$v_c(p) = \frac{E_p}{\pi R_B C} \frac{1}{p} \frac{1}{p + \frac{1}{2R_A C}} \quad (23)$$

where  $p$  = Laplace operator.

The average demodulated voltage may be similarly written in operational form (see Eq. 17) as follows:

$$v_{R_2}(p) = \frac{1}{2} \frac{R_2}{R_1 + R_2} \left( v_c(p) + \frac{2E_p}{p \pi} \right) \quad (24)$$

Combining Eq. (23) and (24), the demodulated output is reduced to the following form:

$$v_{R_2}(p) = \frac{E_p K}{\sqrt{2} p} \eta_D(p) \quad (25)$$

or

$$v_{R_2}(p) = \frac{E_{in(rms)}}{p} \left[ \eta_{D_0} \left( \frac{p \tau_1 + 1}{p \tau_2 + 1} \right) \right] \quad (26)$$

where

$\eta_{D_0}$  = dc or steady-state demodulation efficiency

$$\tau_1 = R_1 C$$

$$\tau_2 = 2R_A C = \frac{2C R_1(R_1 + R_2)}{2R_1 + R_2}$$

In the demodulation circuit of Fig. 16,

$$\tau_1 = 4.2 \times 10^3 \times 10^{-5}$$

$$= 4.2 \times 10^{-2} \text{ sec}$$

and

$$\tau_2 = 2 \times 10^{-5} \frac{4.2(8.9) \times 10^6}{13.1 \times 10^3}$$

$$= 5.7 \times 10^{-2} \text{ sec.}$$

The pole and zero corner frequencies are then, respectively,

$$f_2 = \frac{1}{2 \pi \tau_2} = 2.8 \text{ cps}$$

and

$$f_1 = \frac{1}{2 \pi \tau_1} = 3.8 \text{ cps.}$$

The maximum phase shift, as calculated at  $\sqrt{f_1 f_2} = 3.24$  cps, is 9 deg lagging. Maximum-efficiency detectors of this design (90%) will produce 1-octave pole-zero doublets with maximum associated phase lags of about 20 deg. As in other phase contributions, the modest amount presented by this demodulator need not present a problem unless, of course, it occurs unexpectedly at gain crossover, using up most of the margin.

**c. DC Amplifier.** The dc amplifier, which is the final element in the electrometer and comprises transistors Q7, Q8, Q9, and Q10, provides the following functions:

1. Supplementary gain for required loop tightness,
2. Suitably wide output dynamic range,
3. Demodulation ripple filtering, and
4. Low output impedance.

Consider the gain requirement. The dc gain between modulator and demodulator was designated to be 35. The section following the demodulator must also provide a dc gain of 35 if the arbitrary standard of tightness,

the zero-frequency feedback factor, is to be about 1,000. The filter capacitor, located across the amplifier in this design, must be chosen so as to satisfy a variety of conditions. It must reduce the ripple component at the output of the electrometer to within tolerable limits for external measuring equipment. This is most often a level low enough to preclude problems due to ripple feedback to the modulator. This capacitor should not, however, be made so large as to produce a serious voltage rate-limiting problem. Such a problem is often caused by a combination of (1) limited dynamic range in the carrier amplifier and (2) too large a filter capacitor. Since this capacitance is an important term in one of the corner frequencies for the low-pass loop transmission characteristic, it must also be scrutinized from the viewpoint of loop stability.

The filter-amplifier is depicted in a somewhat simplified form in Fig. 23a. The input  $E_D$  is the average demodulated signal developed across the shunt switch (Q5) when the switch is loaded by  $R_{67}$ . The resistive  $T$  feedback network performs, as its principal function, the zero-signal level adjustment of the output, which must

be above zero to accommodate the log diode characteristic. Two successive approximations to the circuit shown in Fig. 23a are shown in Fig. 23b and 23c. The nominal voltage gain of the filter-amplifier as calculated from the diagram in Fig. 23c may be written

$$K_2 = \frac{G_{2_0}}{1 + p \tau_3} \quad (27a)$$

where

$$G_{2_0} = \text{dc gain} = \frac{R_{32} \left( \frac{R_{38} + R_{37}}{R_{38}} \right) + R_{37}}{R_{67}}$$

and

$$\tau_3 = \left[ R_{32} \left( \frac{R_{38} + R_{37}}{R_{38}} \right) + R_{37} \right] C_{11} \quad (27b)$$

Characteristic feedback factors of 30 for this amplifier make the equivalent circuit and the resulting gain calculation accurate to within about 3%. Using values from Fig. 16,

$$G_{2_0} = 37.5$$

and

$$\tau_3 = 0.435 \text{ sec.}$$

The rate limit of the electrometer is the slope of the integrated output of the filter amplifier produced by the maximum signal available from the carrier amplifier. Maximum values for positive and negative demodulated voltages will be somewhat different because of asymmetrical current-handling capabilities in the output stage of the triplet amplifier on negative and positive swings. In the actual transfer characteristic as shown in Fig. 24, the maximum average positive demodulator voltage of 1.2 v establishes an amplifier charging rate limit of

$$\frac{dE_o}{dt} = \frac{E_D}{R_{67} C_{11}} = -100 \text{ v/sec.}$$

This permits the amplifier to negotiate a negative 5-v step in 50 msec if no other factors are involved.

In most applications, where the output of a sensitive device such as this electrometer must be protected against electrostatic coupling of external power and signal transients, it is imperative to furnish the amplifier with a suitably low output impedance. Over-all electrometer

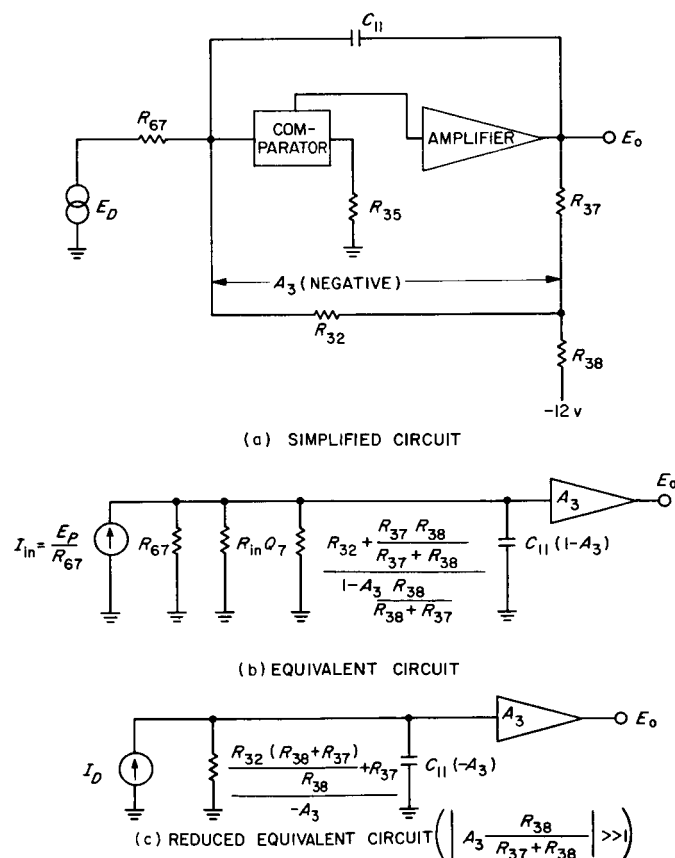


Fig. 23. DC filter amplifier

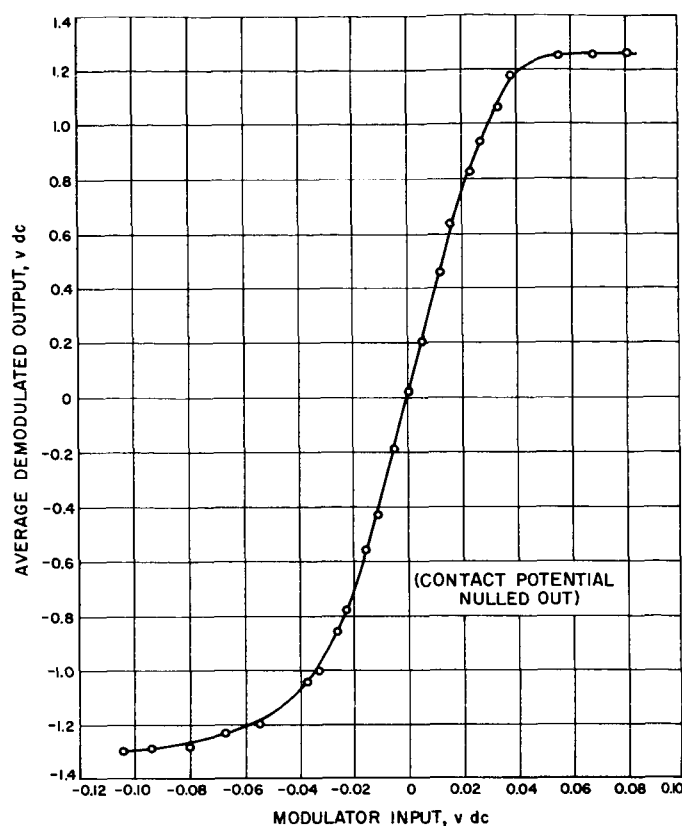


Fig. 24. Static transfer characteristic of carrier section

feedback does not necessarily ensure wide-band protection, because at low input-current levels the dynamic feedback resistance is high, and unity-gain crossover for the loop feedback factor occurs at low frequencies. The result is a total absence of impedance degeneration above a few cycles per second. For this reason, local feedback in the filter-amplifier is required to provide low-output impedance independent of the over-all loop. The emitter-follower, Q10, for instance, may have an output impedance of 300 ohms, further degenerated by the local feedback to about 10 ohms. The dc impedance of 10 ohms is further reduced at frequencies where  $C_{11}$  produces increased local feedback. The static output impedance, as previously suggested, is also enhanced by the dc feedback factor of the entire loop, which reduces the filter-amplifier impedance by 1,000 to a small fraction of an ohm.

#### 4. Offset Stability

There are three main contributions to drift at the electrometer input. These are

1. Variation in dynamic capacitor contact potential,

2. Variation in balance of the dc amplifier comparator, and
3. Variation of the demodulator offset.

Contact potential drift in the modulator appears directly at the electrometer input. Changes in modulator reference potentials are similarly reflected directly at the input. As a precaution against inverse-polarity leakage currents, the modulator is referenced so that a nominal negative potential appears at the summing point. Leakage produced by input resistance will therefore cause a small error current, of the same polarity as positive-ion input current, to flow in the feedback element.

The comparator stage of the dc filter-amplifier is a relatively coarse device. The drift in the differential stage composed of Q7 and Q8 is characteristically about  $-50$  mv between  $-20$  and  $+70^\circ\text{C}$ , yielding an average temperature coefficient of  $-0.6$  mv/ $^\circ\text{C}$ . If the gain of the carrier section between the modulator and demodulator were assumed constant at 35 over this temperature range, the drift at the summing point attributable to the dc amplifier instability would be 1.4 mv.

The demodulator transistor (Q5) is likewise coarse in performance. A 2N329A PNP alloy transistor is used in the normal configuration for its superior current gain, thereby forsaking the stability of the inverted connection. In an application such as this, one may consider the zero-signal closed-switch offset potential as the principal source of instability. This offset is expressed as follows (Ref. 17):

$$v_0 = \frac{KT}{q} \ln \frac{1}{\alpha_i} \quad (28)$$

where

$\alpha_i$  = inverse emitter-to-collector current gain

$v_0$  = collector-to-emitter voltage with zero collector current.

It is estimated that drifts in  $v_0$  attributable to temperature and  $\alpha$  changes will not exceed 10 mv. The full-cycle average drift, 5 mv, would correspondingly produce a 0.14-mv shift at the electrometer input. The combined demodulator-dc amplifier drift reflected to the electrometer input would therefore be small compared with the modulator contact potential drifts, which fall in the 5- to 10-mv range.

### C. Feedback Stability

This section will first describe theoretical considerations in the analysis of the electrometer as a feedback amplifier. The equations for loop transmission (feedback factor) will be presented under conditions of zero and fixed secondary damping feedback. A table of dominant time constants versus input current will illustrate the consequences of using a nonlinear or non-discrete primary feedback element. Both theoretical and measured curves of loop transmission are presented, after which closed-loop frequency and transient responses are shown.

#### 1. Open-Loop Frequency Response

The electrometer transfer characteristic may be written

$$E_o = I_{in} Z_f \left( \frac{A\beta}{1 - A\beta} \right) \quad (29)$$

where

$A$  = forward dc amplifier gain

$\beta$  = portion of output returned to summing point

$Z_f$  = feedback impedance.

The amplifier, as is implied in Eq. (29), is dependent upon the feedback factor  $A\beta$  for such important char-

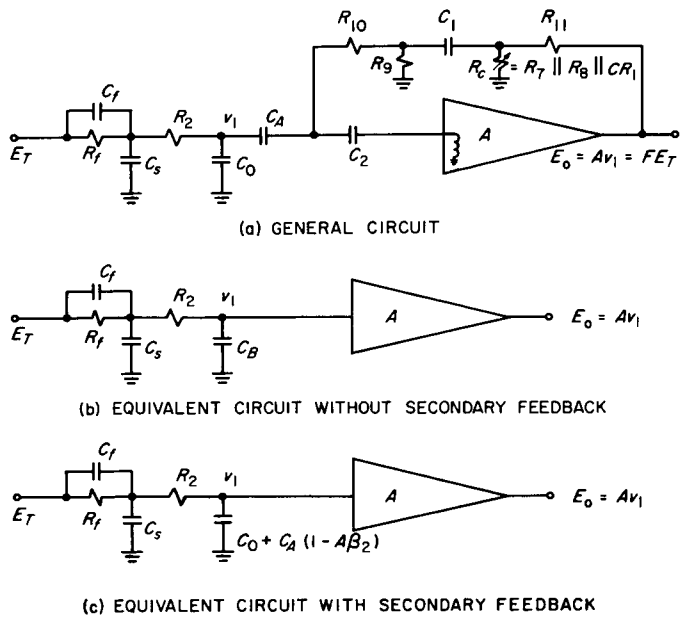


Fig. 25. Equivalent circuits for determining loop transmission

**a. Theoretical Considerations.** At low currents where secondary feedback is effectively disconnected, the loop transmission as determined from the circuit of Fig. 25 is given by

$$F = \frac{A(1 + p\tau_f)}{p^2(R_f R_2 C_s C_B + \tau_f C_B R_2) + p(R_f[C_B + C_s + C_f] + C_B R_2) + 1} \quad (30)$$

acteristics as static accuracy, speed of response, and loop stability. Trying to satisfy conditions for loop stability presents an unusual problem, in that  $R_f$ , one of the principal parameters in the calculation of  $A\beta$  (see Fig. 25a), varies in excess of 7 decades.

Since the feedback resistance varies as an inverse function of the feedback current, the secondary feedback, or damping, must also be nonlinear. No single condition of feedback will satisfy requirements for both loop stability and speed of response at all currents within the measurable range of the instrument. A nonlinear attenuator composed of R7, R8, R11, and zener diode CR1 provides a two-point compensation characterized by zero damping at low currents, fixed damping at high currents, and a transition corresponding to about one current decade. The use of  $C_A$  in the dual role of damping element and carrier-frequency coupling capacitor was suggested by an earlier commercial application (Ref. 18).

where

$$\tau_f = R_f C_f$$

$$C_B = C_0 + (C_A C_2)/(C_A + C_2)$$

$C_s$  = collector-to-shield capacitance.

The amplifier gain may be described principally by the filter-amplifier and demodulator time constants in such a manner that

$$A = \frac{A_0(1 + p\tau_2)}{(1 + p\tau_1)(1 + p\tau_3)} \quad (31)$$

where

$A_0$  = dc gain

$\tau_1$  = demodulator pole time constant (see Eq. 26)

$\tau_2$  = demodulator zero time constant (see Eq. 26)

$\tau_3$  = filter-amplifier time constant (see Eq. 27b).

The polynomial in the denominator of Eq. (30), when written in the form

$$ap^2 + bp + c$$

can be approximately factored into

$$c \left( \frac{a}{b} p + 1 \right) \left( \frac{b}{c} p + 1 \right)$$

when

$$\frac{4ac}{b^2} \ll 1.$$

Over the range of input currents where secondary feedback is disconnected, this condition is satisfied in the following form:

$$\frac{4R_2}{R_f} \left\{ \frac{C_B(C_s + C_f)}{[(C_B + C_s + C_f) + C_B(R_2/R_f)]^2} \right\} \ll 1.$$

The loop transmission  $F$  may therefore be written in the following factored form:

$$F = \frac{[A_0(1 + p\tau_2)(1 + p\tau_4)]}{[(1 + p\tau_1)(1 + p\tau_3)(1 + p\tau_5)(1 + p\tau_6)]} \quad (32)$$

where

$$\tau_4 = \tau_f = C_f R_f$$

$$\tau_5 = R_f(C_B + C_s + C_f) + C_B R_2$$

and

$$\tau_6 = \frac{R_2 C_B (C_s + C_f)}{(C_B + C_s + C_f) + C_B (R_2/R_f)}.$$

As feedback current is raised to the order of  $10^{-10}$  amp, upward migration of the corner frequency determined by  $\tau_5$  produces sufficient phase shift at gain crossover to result in oscillatory behavior. The addition of secondary feedback at lower current before this condition is reached produces a new set of dominant time constants.

Consider the effect of the limited amplifier bandwidth on the gain-sensitive capacitance in Fig. 25c. If the amplifier response is approximated exclusively by filter cutoff so that

$$A \cong \frac{A_0}{1 + p\tau_3}$$

the loop transmission is then given by

$$F = \frac{A_0(1 + p\tau_4)}{(1 + p\tau_3)(1 + p\tau'_5)(1 + p\tau'_6)} \quad (33)$$

The expressions for  $\tau'_5$  and  $\tau'_6$  are identical with the  $\tau_5$  and  $\tau_6$  terms of Eq. (32) except that  $C_B$  is replaced by the gain-sensitive capacitance

$$C_0 + C_A \left( 1 - \frac{A_0 \beta_2}{1 + p\tau_3} \right)$$

where

$$\beta_2 = \frac{R_c}{R_c + R_{11}}$$

and

$$R_9 \gg \frac{R_c R_{11}}{R_c + R_{11}}.$$

If  $C_1$  is assumed to be infinite and if the pole in the  $\beta_2$  network (produced by the lag network comprising  $R_{10}$ ,  $C_0$ ,  $C_A$ , and  $C_2$ ) is neglected ( $\tau = 3$  msec), the loop transmission (Eq. 33) may then be reduced to

$$F = \frac{A_0(1 + p\tau_4)}{(1 + p\tau'_6)(1 + p\tau_7)(1 + p\tau_8)} \quad (34)$$

where

$$\tau_7 = -\frac{\tau_3}{A_0 \beta_2} \left[ \left( \frac{C_0 + C_A}{C_A} \right) + \left( \frac{R_f}{R_f + R_2} \right) \left( \frac{C_s + C_f}{C_A} \right) \right] \quad (35)$$

$$\begin{aligned} \tau_8 &= \tau_3 - A_0 \beta_2 C_A (R_2 + R_f) \\ &\quad + (R_f + R_2)(C_0 + C_A) \\ &\quad + R_f(C_s + C_f) \\ &\cong \tau_3 - A_0 \beta_2 C_A (R_2 + R_f) \end{aligned} \quad (36)$$

and

$$\tau'_6 \cong \frac{R_2 R_f}{R_2 + R_f} (C_s + C_f). \quad (37)$$

The dominant pole in Eq. (34) is produced by  $\tau_8$ . The principal effect of the amplifier time constant,  $\tau_3$ , is to add directly to  $-A_0 \beta_2 C_A (R_2 + R_f)$ . Corner frequencies produced by  $\tau'_6$  and  $\tau_7$  occur sufficiently beyond gain crossover as to produce gain margins no less than 15 db over the range of currents for which this secondary feedback is effective.

A consequence of using ac coupling in the secondary feedback that was overlooked in the initial design is the peak that occurs in the loop transmission. While there was no harmful effect in this case, it is evident that this coupling time constant can provide large lagging phase shifts as illustrated in some of the gain and phase curves. Consider the effect of the ac coupling in the secondary loop as embodied in the dominant time constant of Eq. (34). The loop transmission may then be written

$$F \cong \frac{A_0}{1 + p \tau'_8} \quad (38)$$

where

$$\begin{aligned} \tau'_8 &= \tau_3 - A_0 \beta_2 C_A (R_2 + R_f) \frac{p \tau_9}{1 + p \tau_9} \\ &= \frac{\tau_3 + p \tau_8 \tau_9}{1 + p \tau_9} \end{aligned}$$

and

$$\tau_9 = C_1 R_9.$$

Substituting for  $\tau'_8$  in Eq. (38)

$$F = \frac{A_0 (1 + p \tau_9)}{1 + p (\tau_3 + \tau_9) + p^2 \tau_8 \tau_9}. \quad (39)$$

The location of the poles of Eq. (39) in the  $p$  plane are as follows:

$$p_1, p_2 = \frac{(\tau_3 + \tau_9)}{2 \tau_8 \tau_9} \left[ 1 \mp \left( 1 - \frac{4 \tau_8 \tau_9}{(\tau_3 + \tau_9)^2} \right)^{1/2} \right]. \quad (40)$$

For the condition where

$$\frac{4 \tau_8 \tau_9}{(\tau_3 + \tau_9)^2} \gg 1,$$

which is applicable in this case, Eq. (40) may be rewritten

$$p_1, p_2 \cong \frac{-(\tau_3 + \tau_9)}{2 \tau_8 \tau_9} \pm j \frac{1}{(\tau_8 \tau_9)^{1/2}}. \quad (41)$$

The frequency at which  $F$  (Eq. 39) peaks is now determined by the imaginary component of Eq. (41), i.e.,

$$f_{PK} = \frac{1}{2\pi (\tau_8 \tau_9)^{1/2}}.$$

For bias currents of  $10^{-10}$  and  $10^{-6}$  amp where  $\tau_9 = 2$  sec, the peaking frequencies are calculated to be 0.015 and 0.037 cps, respectively.

Table 5 presents a listing of all dominant time constants and their variation with bias current. The asymptotic loop responses resulting from the tabulated corner frequencies for the cases of secondary feedback out and in are shown in Fig. 26 and 27, respectively.

**b. Experimental Results.** To correlate actual performance with predicted behavior and to verify adequacy of phase margins, a set of tests was performed on a laboratory electrometer using the experimental arrangement of Fig. 28. The signal generator was placed in the feedback loop so that the feedback would still stabilize the dc operating point and that output levels would be determined by the equivalent series generator voltage, i.e.,

$$E_o = V_g \left( \frac{F}{1 - F} \right) \quad (42)$$

where

$$V_g = E_T - F E_T.$$

The open-loop amplitude and phase responses were obtained by taking oscilloscope pictures of the waveforms on both sides of the floating signal generator, which also supplied scope trigger pulses. The dc bias current in the tube was determined by resistors connected between a 1-v battery and the electrometer input. This resulted in a 10% reduction in  $A_0$  and in a small modification to the responses of  $F$  vs. the frequency that would have been obtained with perfect current sources. A 50-pf capacitor



Table 5. Nominal time constants and corner frequencies

## (a) Secondary feedback out

Bias current amp	Time constant, sec						Corner frequency, cps					
	$\tau_1$	$\tau_2$	$\tau_3$	$\tau_4$	$\tau_5$	$\tau_6$	$f_1$	$f_2$	$f_3$	$f_4$	$f_5$	$f_6$
$10^{-10}$	0.042	0.057	0.435	0.005	0.168	0.0072	3.8	2.8	0.37	32	0.95	22
$10^{-11}$	↓	↓	↓	0.05	1.59	↓	↓	↓	↓	3.2	0.1	↓
$10^{-12}$	↓	↓	↓	0.5	15.8	↓	↓	↓	↓	0.32	0.01	↓
$10^{-13}$	↓	↓	↓	5.0	158	↓	↓	↓	↓	0.032	0.001	↓

## (b) Secondary feedback in

Bias current amp	Time constant, sec					Corner frequency, cps				
	$\tau_4$	$\tau_6'$	$\tau_7$	$\tau_8$	$\tau_9$	$f_4$	$f_6'$	$f_7$	$f_8$	$f_9$
$10^{-6}$	$5 \times 10^{-7}$	$5.5 \times 10^{-6}$	$1.6 \times 10^{-3}$	9.5	2.0	$32 \times 10^4$	$2.9 \times 10^4$	100	$1.7 \times 10^{-2}$	0.0796
$10^{-9}$	$5 \times 10^{-4}$	$3.7 \times 10^{-3}$	$1.78 \times 10^{-3}$	14.1	↓	320	43	89	$1.1 \times 10^{-2}$	↓
$10^{-10}$	0.005	$9.2 \times 10^{-3}$	$2.04 \times 10^{-3}$	55	↓	32	16.3	78	$2.9 \times 10^{-3}$	↓
$10^{-11}$	0.05	$11 \times 10^{-3}$	$2.15 \times 10^{-3}$	455	↓	3.2	14.4	74	$3.5 \times 10^{-4}$	↓
$10^{-12}$	0.5	$11 \times 10^{-3}$	$2.15 \times 10^{-3}$	4,550	↓	0.32	14.4	74	$3.5 \times 10^{-5}$	↓

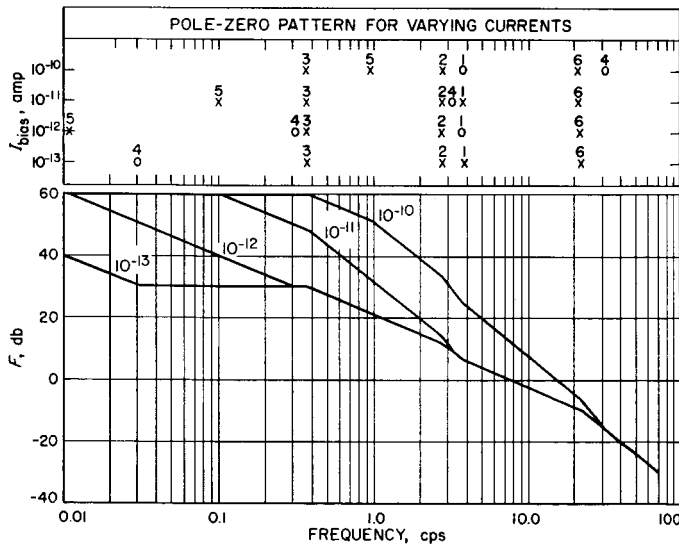


Fig. 26. Asymptotic loop transmission responses without secondary feedback

with a leakage resistance greater than  $10^{15}$  ohms simulated the capacitance between the collector and its electrostatic shield. An R-C filter at the scope input reduced the 60-cps signals generated in the loop by the large floating generator; as a result, measurements above 20 cps were somewhat unreliable. For bias currents greater than or equal to  $10^{-10}$  amp, the secondary feedback was re-

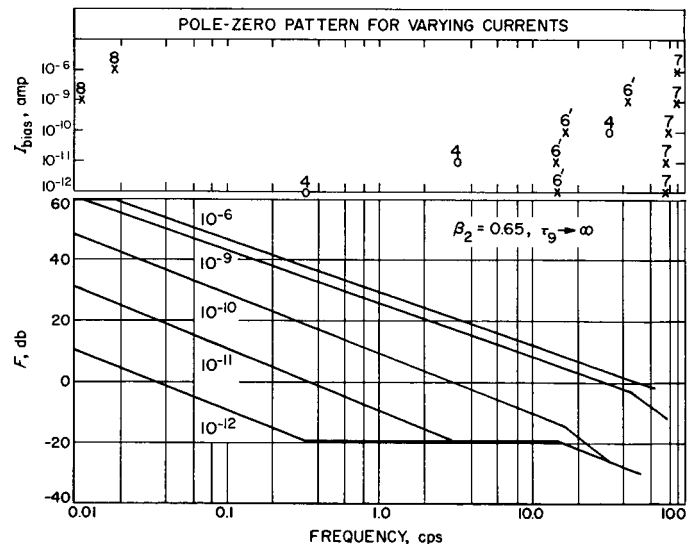
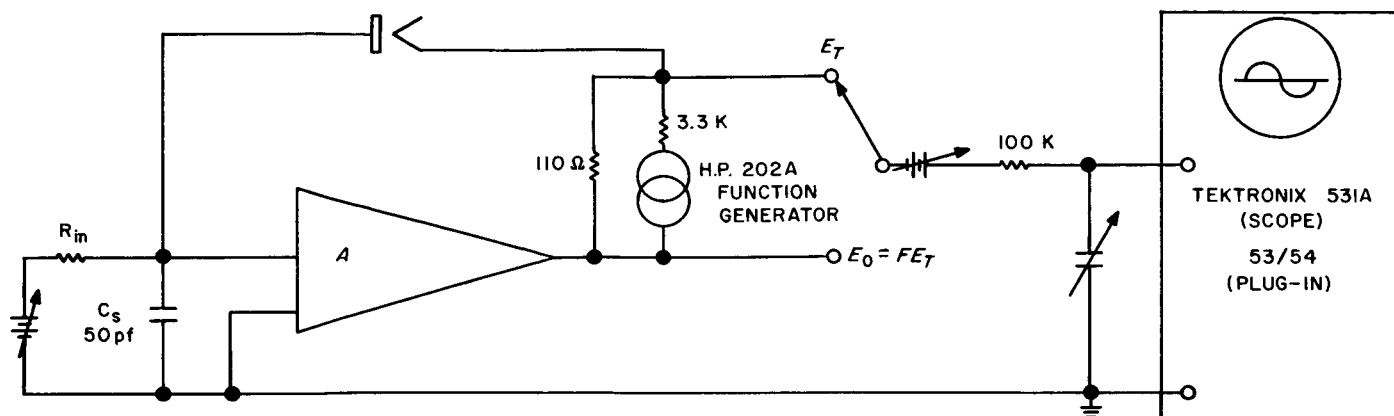


Fig. 27. Asymptotic loop transmission responses with secondary feedback

moved by disconnecting R10. Figures 29 to 34 show gain and phase shift of the amplifier measured at frequencies from 0.01 to 100 cps for bias currents between  $10^{-6}$  and  $10^{-13}$  amp.

The laboratory electrometer used for these tests contained several components whose values were different



**Fig. 28. Test setup for loop transmission measurements**

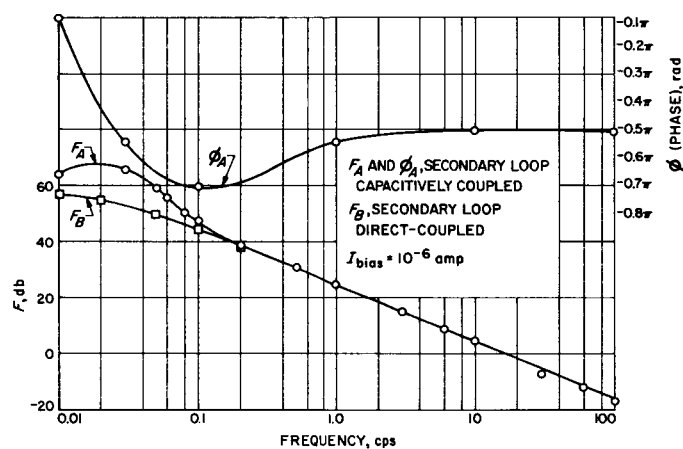


**Fig. 29. Gain and phase curves with secondary feedback in ( $I_{bias} = 10^{-6}$  amp)**

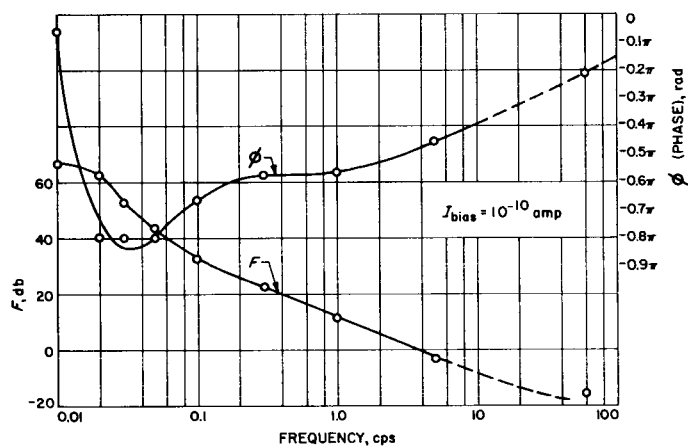


**Fig. 31. Gain and phase curves with secondary feedback in ( $I_{\text{bias}} = 10^{-10}$  amp)**

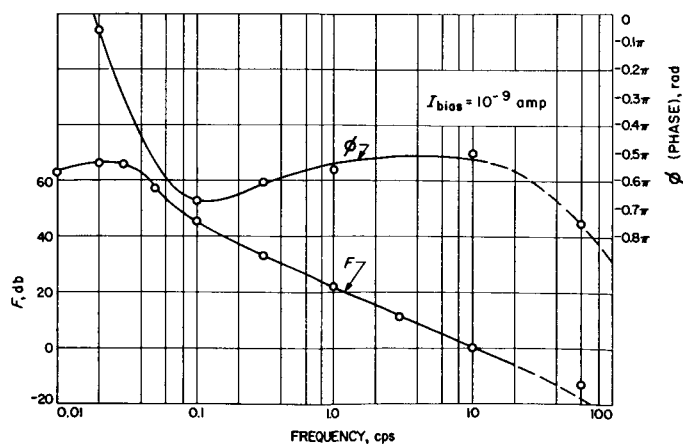


**Fig. 30. Gain and phase curves with secondary feedback in ( $I_{bias} = 10^{-9}$  amp)**

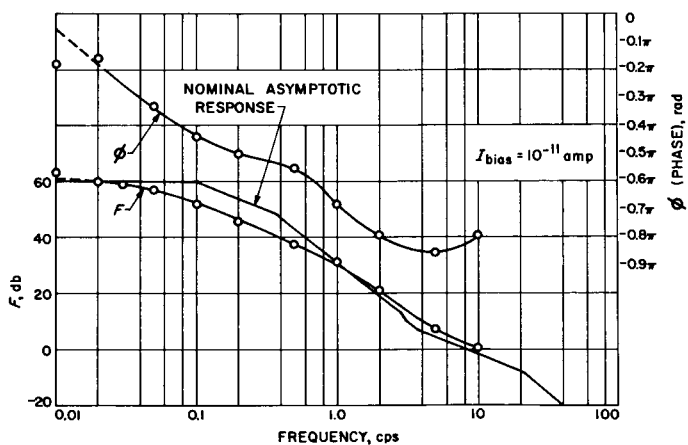


**Fig. 32. Gain and phase curves with secondary feedback out ( $I_{\text{bias}} = 10^{-11}$  amp)**

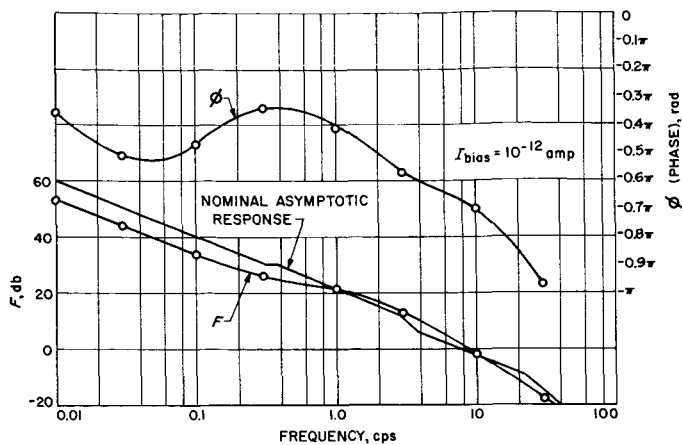


Fig. 33. Gain and phase curves with secondary feedback out ( $I_{\text{bias}} = 10^{-12}$  amp)

from the nominal flight-unit values or had changed since those components were installed. Since there was some variance between measured responses and nominal curves, comparison was then made between measured component values and values providing the best fit to the experimental curves (see Table 6).

Table 6. Component values

Component	Value		
	Nominal	Measured	Best fit
			<b>Assumed</b>
$C_0$ , pf	50	150	150
$C_2$ , pf	220	—	220
$C_1$ , $\mu$ f	1	—	1
$R_{32}$ , K	130	150	150
$R_{37}$ , K	6.8	9.1	9.1
$R_{38}$ , K	24	24	24
$R_{11}$ , K	21.5	21.5	21.5
$R_c$ , K	60 (max.)	60 (max.)	60 (max.)
$R_0$ , meg	2	2	2
$R_f$ , $\Omega$	$1/10 I_{\text{bias}}$	$\approx 1/10 I_{\text{bias}}$	$1/10 I_{\text{bias}}$
			<b>Calculated</b>
$C_s$ , pf	50	63	154
$C_A$ , pf	70	60	59
$C_{11}$ , $\mu$ f	2.5	0.96	0.93
$C_f$ , pf	5	5	5.3
$R_s$ , meg	200	160	208
$A_0$	-1000	—	-1000

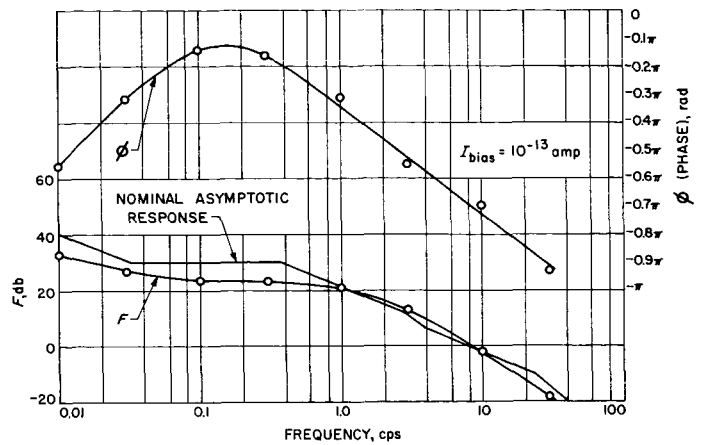


Fig. 34. Gain and phase curves with secondary feedback out ( $I_{\text{bias}} = 10^{-13}$  amp)

The best-fit component values agree reasonably well with the measured values except for  $C_s$ , where the dispersion is not fully understood at this time. Most notable departures from expected values were in the cases of the filter capacitor C11 and the dynamic capacitor rest capacitance,  $C_0$ . The filter capacitor, a bipolar tantalum unit, may have deteriorated with age. The dynamic capacitor, a non-flightworthy developmental model, had apparently acquired a reduced reed-to-anvil spacing.

Of the six bias conditions for which curves have been drawn, minimum margin occurs with a bias current of  $10^{-11}$  amp. (Fig. 32). In this curve, the rolloff rate at gain crossover (10 cps) is about 8 db/octave with a  $-144$ -deg phase shift, although the phase shift in this case does reach a pre-crossover maximum of  $-153$  deg at 6 cps. Deviations in the capacitances  $C_0$  and  $C_s$  reduced the corner frequency  $f_c$  from a nominal 22 cps to less than half its standard value. This placed  $f_c$  near gain crossover, thereby reducing margins in the laboratory instrument, though not to intolerably small levels. The flight instruments were generally adjusted for transition between secondary feedback states at about  $5 \times 10^{-12}$  amp.

## 2. Closed-Loop Performance

When the electrometer is driven by a current source, its transfer impedance may be expressed in the following modified form of Eq. (29):

$$Z_T = \frac{-E_o}{I_{in}} = Z_f \left[ \frac{1}{1 - (1/F)} \right]. \quad (43)$$

If the loop transmission characteristic is approximated at gain crossover ( $f_{gc}$ ) by a 6 db/octave rolloff rate, the transfer impedance is then given by

$$Z_T = \frac{R_f}{(1 + p\tau_4)(1 + p\tau_{gc})} \quad (44)$$

where

$$\tau_{gc} = \frac{1}{2\pi f_{gc}}$$

Table 7 lists the time constants of Eq. (44) and their associated frequencies as a function of bias current. The gain-crossover frequency with secondary feedback ( $f'_{gc}$ ) is also listed.

Families of closed-loop frequency responses are shown in Fig. 35 and 36 for secondary feedback in and out, respectively. Electrometer biasing was similar to that used in Fig. 32, and a signal current was inserted into the summing point by a function generator connected in series with a suitably large resistor. The only parameter significantly different from the ones used in the loop transmission tests was the modulator rest capacitance ( $C_0$ ), which was 59 pf for the dynamic capacitor used in this case.

Peaking that occurs at lower currents in Fig. 35 is directly attributable to phase shifts associated with peaks in loop transmission characteristics that are not sufficiently removed from gain crossover. The overshoots associated with transient response to these characteristics were not observed in flight instruments, since secondary feedback transition occurred at about  $5 \times 10^{-12}$  amp.

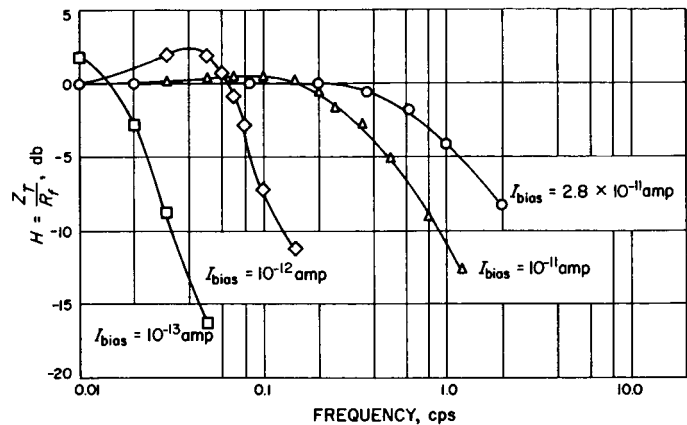


Fig. 35. Closed-loop frequency response with secondary feedback

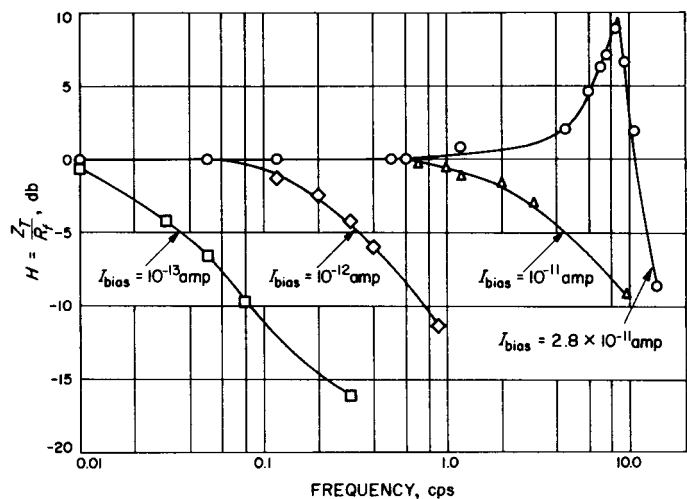


Fig. 36. Closed-loop frequency response without secondary feedback

Table 7. Dominant time constants and corner frequencies for nominal closed-loop response

Bias current amp	Time constant, sec			Corner frequency, cps		
	$\tau_4$	$\tau_{gc}$	$\tau'_{gc}$	$f_4$	$f_{gc}$	$f'_{gc}$
$10^{-6}$	$5 \times 10^{-7}$	— <sup>a</sup>	0.0094	$3.7 \times 10^5$	—	17
$10^{-9}$	$5 \times 10^{-4}$	— <sup>a</sup>	0.014	370	—	11
$10^{-10}$	0.005	— <sup>a</sup>	0.053	37	—	3.0
$10^{-11}$	0.05	0.018	0.45 <sup>b</sup>	3.7	9	0.35
$10^{-12}$	0.5	0.018	4.5 <sup>b</sup>	0.37	9	0.035
$10^{-13}$	5	0.018	45 <sup>b</sup>	0.037	9	0.0035

<sup>a</sup> Secondary feedback connected at these currents; for applicable time constant, see  $\tau'_{gc}$  column.

<sup>b</sup> Secondary feedback customarily disconnected at these currents; values listed denote theoretical values that would be obtained if secondary feedback were connected.

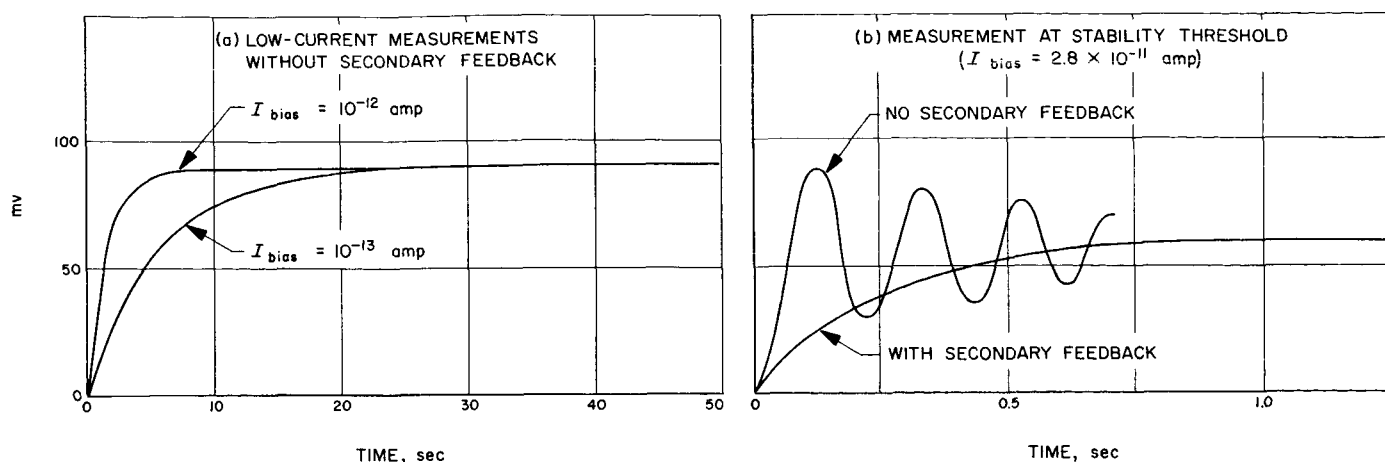


Fig. 37. Closed-loop transient response

The peaks are removable, however, by direct coupling of the secondary feedback. This is considered a generally advisable procedure for this configuration providing that capacitor  $C_A$  has a sufficiently large leakage resistance.

Closed-loop transient responses (Fig. 37) were recorded by changing the sine-wave signal used in the previous closed-loop tests to a square wave. Care was taken to keep the signal amplitude down to swings of not more than a quarter of a decade from quiescent levels, lest nonlinearities in the feedback tube mask the true small-signal performance.

Although this electrometer is fast enough for *Mariner 2* sampling rates (one sample per 17 sec), the interelectrode capacitance of the feedback element may make this system too sluggish for other applications requiring faster low-current response. Speed-of-response capabilities for this amplifier may be put in a better perspective, however, by inspecting its performance with a more universally used feedback component such as a carbon resistor. A current threshold of  $10^{-13}$  amp, for example, may be obtained with a feedback resistor of  $10^{11}$  ohms. If gain crossover for this new system were comparable to the values in Table 7 ( $\tau_{gc} = 0.018$  sec), the closed-loop speed of response would reflect the lower time constant of the new feedback element. Assuming a distributed capacitance of 0.5 pf across the resistor, the feedback time constant  $\tau_4$  becomes 0.05 sec. This value of  $\tau_4$ , indeed, becomes the  $e^{-1}$  response time for the electrometer, because  $\tau_{gc}$  is small enough to not affect the composite response. If the filter-induced rate limit for the electrometer described in this Report (100 v/sec) were applied to this hypothetical case, rate limiting would occur for input step currents above  $5 \times 10^{-11}$  amp. A maximum-range

signal of about 10 v ( $I_{in} = 10^{-12}$  amp) would therefore require about 100 msec to reach 90% of full amplitude.

For the case of a particular feedback resistor, electrometer transient responses to signal currents below rate-limit level may be considered uniformly linear. What makes quantitative comparison of the log diode system difficult is that dominant time constants for log feedback are based upon bias currents and not necessarily on absolute values of transient current. It is also very possible in actual spectrometer applications that the log diode system will come to rest somewhere between the lower end of the useful diode characteristic and the discriminator threshold. Tube capacitance must then be charged before the tube becomes conductive, whereas resistive feedback provides a constant conductance and a fixed starting point.

In applications requiring the speed of response and zero stability afforded by a feedback resistor, one may then tailor the loop transmission characteristic to the specific requirements of the resistor. The technique of secondary damping feedback described in this Report may then be applied, when needed, in a more efficient manner by the inclusion of a fixed damping factor ( $\beta_2$ ). In a similar fashion, commutated feedback resistors may also be efficiently used with synchronous switching of discrete optimized feedback networks.

#### D. Dynamic Reed Capacitor Development

Dynamic capacitors of the type used in the *Ranger* and *Mariner* solar plasma instruments (Fig. 38 and 39) originated over 15 years ago (Ref. 16), and have been employed in various commercial electrometers. Since the

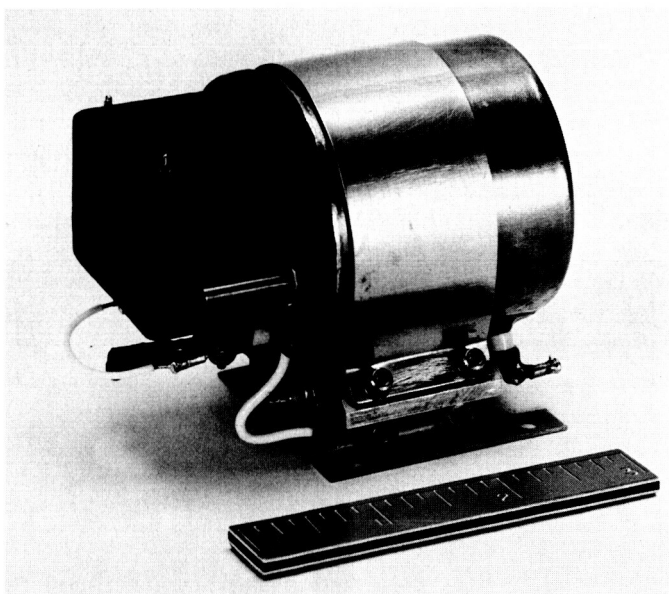


Fig. 38. Dynamic capacitor on mounting base

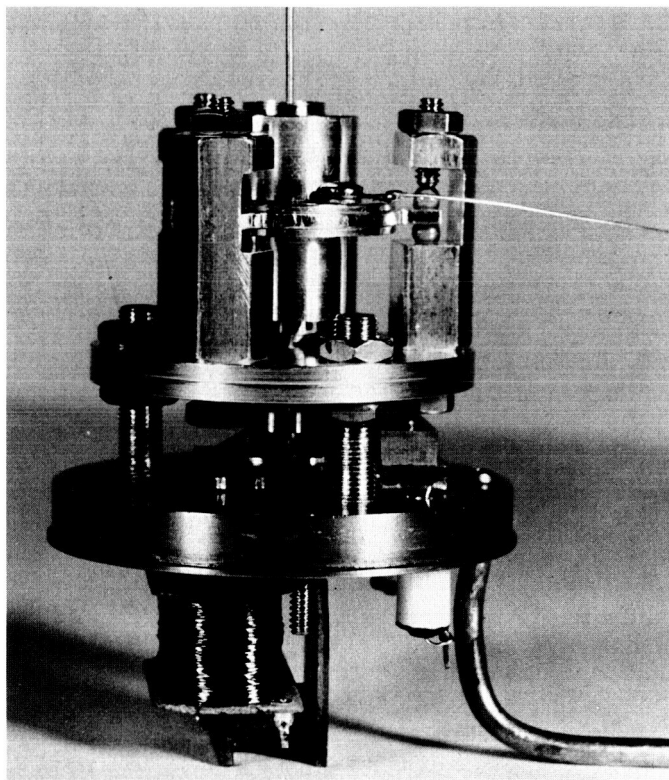


Fig. 39. Uncased dynamic capacitor

instrument demanded a lightweight, low-power device that could withstand the rigorous vibrational and thermal environment imposed by the spacecraft, a special design was required. In January 1960, a development contract

for the vibrating reed capacitor was let to the Applied Physics Corporation of Monrovia, California.

Evaluation of the first six prototypes and communication with Applied Physics resulted in the following target specifications:

1. Reed resonance at 25°C:  $2,395 \pm 5$  cps.
2. Resonant frequency shift between 0 and 70°C: 15 cps max.
3. Conversion efficiency at 2,400 cps and 25°C: 8 to 10%.
4. Resonant  $Q$ : 150 max.
5. Drive voltage at 2,400 cps: 6.8 v rms.
6. Drive coil power: 75 mw max.
7. Reed-to-anvil rest capacitance:  $C_0 = 70$  pf max.
8. Coupling capacitance:  $50 \pm 3$  pf.
9. Contact potential:  $0 \pm 50$  mv dc max.
10. Temperature coefficient of contact potential:  $70 \mu\text{V}/^\circ\text{C}$  max.
11. Weight: 0.6 lb max.
12. Unit evacuation pressure:  $< 10^{-5}$  Torr.
13. Input resistance:  $> 10^{14}$  ohms.

The choice of reed resonance at approximately 2,400 cps was based on (1) the ability to drive the reed directly from the 2,400-cps spacecraft supply and (2) the small size of the reed, which resulted in an over-all structure of minimum dimensions. The values of rest and coupling capacitance were influenced by such factors as conversion efficiency, loop transient response, and the source impedance presented to the subsequent transistor electronics.

The over-all structure of the reed capacitor suggested a cylindrical or can-type enclosure. The can was evacuated in order to obtain high compliance of the reed with a minimum expenditure of drive power for a given conversion efficiency. In addition, since anticipated uses of the converter would require extended periods of operation (one to two years) in the vacuum of space, and since gradual loss of an atmosphere of inert gas in a modulator would catastrophically alter the reed characteristics, the evacuated can appeared doubly attractive.

However, as development progressed, the effect of the evacuated can on the contact potential specification

became painfully obvious. Temperature cycling of the evacuated modulator caused outgassing of most of the materials inside the device and resulted in contamination of the reed and anvil, with an accompanying increase in contact potential and its thermal coefficient. This problem was ultimately solved by high-temperature vacuum annealing of most components internal to the can and by elimination of all internal organic materials and internal solder connections.

Early in the program, the need for a reed-tracking oscillator was considered; that is, a device that would sense the drift in reed resonant frequency due to age and temperature change and would synchronously drive the phase-sensitive demodulator in the electrometer amplifier. The behavior of the capacitor resonant characteristic vs. temperature for the early prototypes (Fig. 40) was monitored, and several units were installed in a breadboard electrometer. Loop-gain and phase-margin tests were performed vs. temperature in this test fixture, with both the reed and the demodulator driven from a fixed 2.4-kc signal (see the discussion on the demodulator). Analysis of these data indicated that the change in amplifier loop gain, owing to changes in demodulator efficiency (caused by phase shift between the reed output signal and the demodulator drive signal), would not seriously degrade the amplifier performance. Because of this fact and the limited period for development of the instrument, it was decided in September

1960 to drop the tracking oscillator approach and start production on units to be driven at 2.4 kc, a point slightly above the natural resonant frequency. By operating the reed in this manner with the specified  $Q$  and the allowable resonant frequency drift, it appeared that the amplifier loop-gain stability requirements would be reasonably easy to satisfy. Trouble developed shortly thereafter when attempts at simultaneous control of parameters such as resonant frequency, frequency drift, mechanical  $Q$ , and conversion efficiency led to a poor yield of production modulators. To meet the demands of the *Ranger 1* and 2 system schedules, it then became a necessary part of the reed acceptance procedure to run each modulator in an electrometer breadboard and select the optimum phase compensation network for the demodulator for that particular assembly. Since the production reed characteristics were not uniform, this optimum phase shift network had to be selected by examining the gain and carrier phase characteristics of the electrometer over the operating temperature range ( $-10$  to  $+80^{\circ}\text{C}$ ) and selecting a compromise value which would ensure electrometer stability at all temperatures.

This complicated evaluation procedure subsequently led to a new contract with the Applied Physics Corporation in April 1961, which resulted in a capacitor with a piezoelectric crystal mounted on the reed. Since the crystal, which was made of lead titanate, gave maximum output at reed resonance, it provided a stimulus signal for a regenerative coil drive system, which could also synchronously drive the demodulator. The frequency stability of mechanical resonance in this capacitor was also markedly improved by changing the reed material from stainless steel 303 to a constant-modulus alloy, Ni-SPAN-C. The mechanical assembly drawing (Fig. 41) illustrates the rugged construction of the unit, which passed vibrational tests far surpassing the actual launch vibration environment.

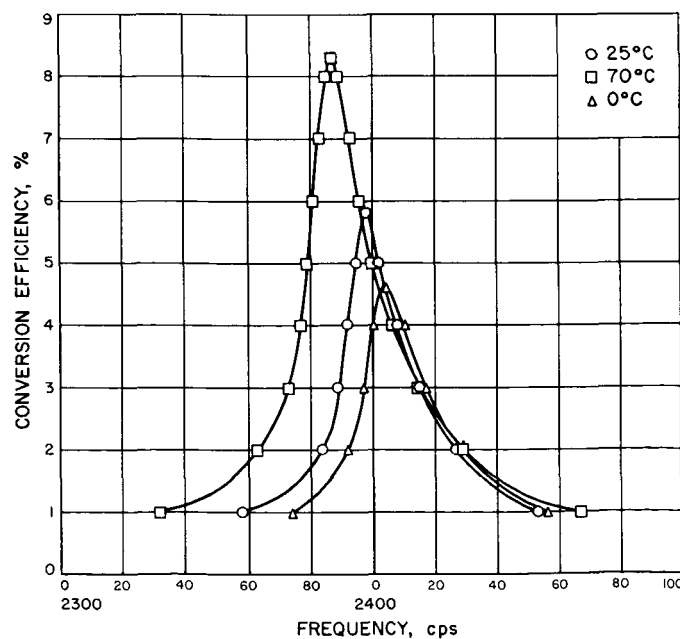


Fig. 40. Resonant characteristic of early prototype dynamic capacitor vs. temperature

The center post forms one element of the coupling capacitor with respect to the stator assembly and also acts as an input terminal to the stationary element of the variable capacitor, the anvil. The construction design ensures that both the variable and coupling capacitors are guarded, in order to provide capacitor stability and minimize leakage current paths. Although the center post was initially designed to house an input resistor that provided isolation of the source and input terminal capacitance from the reed-anvil capacitance, it was decided to accept a small decrease in open-circuit conversion efficiency (owing to additional shunt capacitance) and to place the

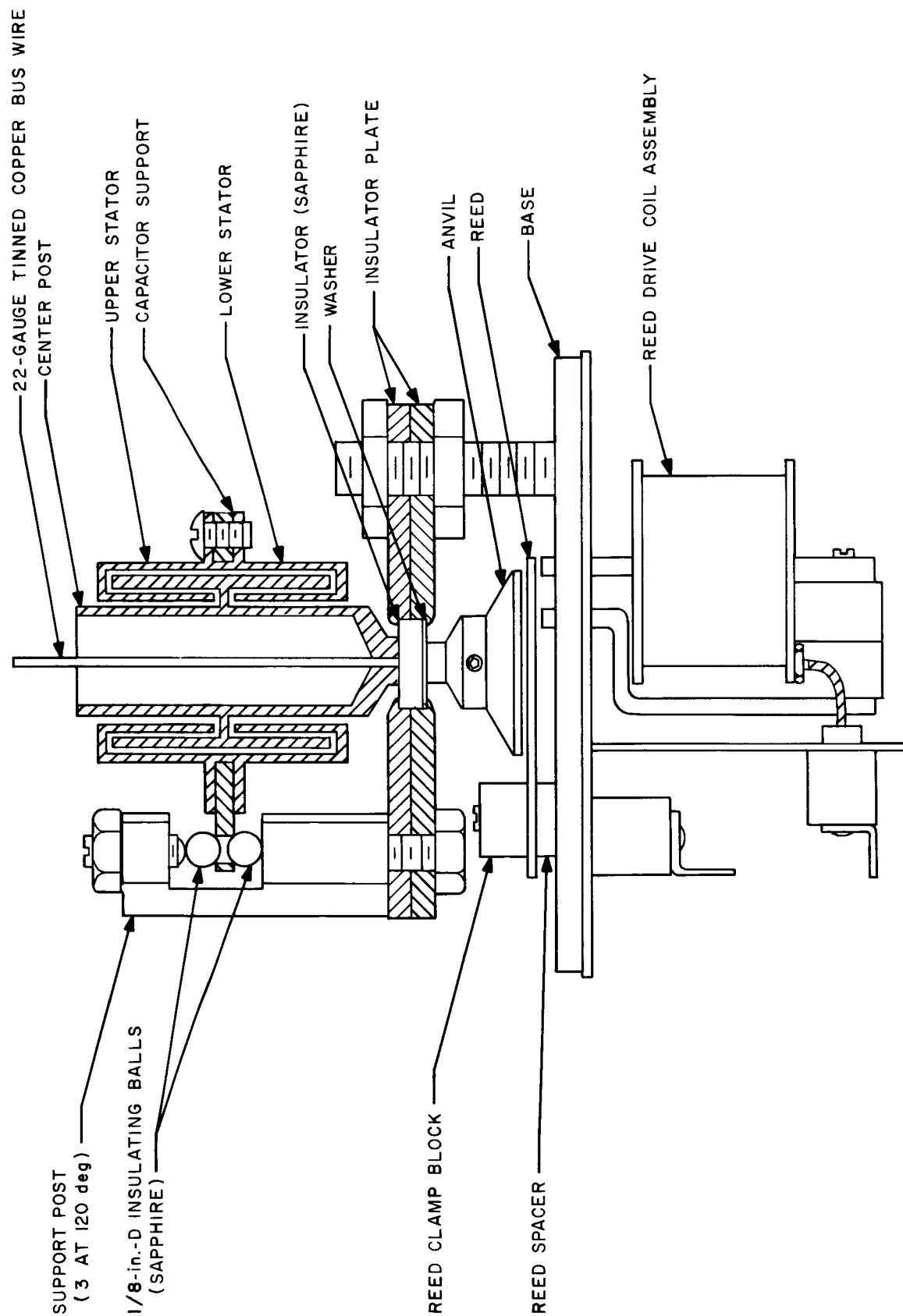


Fig. 41. Dynamic capacitor assembly



resistor outside the assembly in order to reduce possible sources of contamination. The *Mariner 2* unit (with an end shield to reduce the effects of magnetic fields from the reed assembly) was 3.25 in. long by 2.06 in. in diameter and weighed 0.6 lb.

Since the absolute value of the coupling capacitor is not critical in an electrometer of this type, an improved version of the unit was later developed which utilized

small-area, closely spaced, parallel plates for the coupling capacitor and afforded a 3/4-in. reduction in length and a resultant weight saving. A sapphire input terminal increased the input resistance to more than  $10^{16}$  ohms. The superior short time constant of strain currents exhibited by this material has made practicable the design of electrometers for long-term space use with a null stability of  $10^{-14}$  amp over the temperature range of  $-50$  to  $+90^{\circ}\text{C}$ .

#### IV. THE DEFLECTION VOLTAGE SYSTEM

The electrostatic deflection system for the *Ranger* and *Mariner* plasma instruments consisted of three elements: a digital programmer, a high-voltage sweep amplifier, and the electrostatic deflection plates. The programmer received timing pulses from the spacecraft DAS and supplied precise analog currents to the high-voltage sweep amplifier. The output voltage of the sweep amplifier was then impressed across the electrostatic deflection plates so that particles of a particular charge sign and energy proportional to that deflection voltage were focused through the deflection plate assembly onto the Faraday charge collection cup. Mechanization of the *Ranger* and *Mariner* deflection systems was practically identical except that the *Mariner* sweep amplifier was somewhat simpler since only positive ions were to be measured.

##### A. Electrostatic Deflection Plates

The *Ranger* and *Mariner* deflection plate systems (Fig. 4 and 8 respectively) were designed according to dimensions supplied by the JPL experimenters, M. M. Neugebauer and C. W. Snyder. Each unit consisted of a set of curved parallel plates separated by ground rails to control field fringing effects between the plates. A rectangular plate at ground potential was located at both the entrance and exit of the deflection plates for the same

reason. Inside the entrance to the Faraday cup, but shielded from the particle beam by the rectangular ground plane, was a suppressor electrode which prevented secondary emission of electrons from the Faraday cup due to collisions of incident particles. All metal parts were gold-plated magnesium with the exception of the entrance ground plane, which for reasons of spacecraft passive temperature control was made of polished aluminum.

The energy  $E_c$  required for a constant radius of curvature for normally incident particles was equal to 2.74 times the deflection voltage on *Ranger* and 4.0 times the deflection voltage on *Mariner*. Differential deflection voltage (outer to inner plate) vs. energy level is shown in Tables 2 and 3 for the *Ranger* and *Mariner* systems, respectively.

Evaluation of a prototype instrument in a particle accelerator revealed a troublesome phenomenon. Ultraviolet photons in the Lyman-Alpha region emitted by the particle source reflected down the bright gold walls of the deflection plates and then reflected off the charge collection cup. This indirectly illuminated the negatively biased suppressor electrode and caused a release of photoelectrons. The photoelectron current collected at the Faraday cup and measured by the electrometer was on the

order of  $10^{-10}$  amp or three orders of magnitude above the electrometer threshold.

The problem of darkening the gold-plated parts to reduce the reflected light was complicated by the fact that any material utilized had to be a good electrical conductor. Following a method described for increasing the efficiency of infrared detectors (Ref. 19), it was decided to coat the deflection plates and Faraday cup with gold-black. Gold was evaporated off a tungsten filament onto the gold-plated magnesium surfaces in a low-pressure atmosphere of hydrogen. The hydrogen decreased the mean free path and the temperature of the gold molecules emanating from the filament so that they accumulated on the surfaces of interest in a loose molecular structure. The resultant surface was extremely black to ultraviolet as well as visible wavelengths. Although the black surface could be easily rubbed off, evaluation over a temperature range of  $-50$  to  $+150^{\circ}\text{C}$  and exposure to a vibrational energy spectrum much greater than that anticipated on the spacecraft failed to indicate any changes in the surface absorptivity.

Subsequent evaluation of the gold-black system with an ultraviolet source whose estimated intensity was equal to three times that emitted by the Sun revealed that the resultant background current was on the order of  $10^{-14}$  amp (measured with a commercial electrometer) and well below the flight electrometer threshold. Gold-black was applied on later instruments using nitrogen in lieu of hydrogen, but in either case the process was an extremely laborious one, owing to the difficulty in obtaining a uniform, nonspecular coating over the large surface area. Platinum-black, which is a commercial plating process, was evaluated late in the *Mariner* program and proved to be as effective as the gold-black. The platinum-black method was dropped, however, owing to the limited development time, when it was discovered that there was a corrosive action between the platinum-black plating solution and the magnesium plates as a result of the porosity of the gold plate.

In a redesign of the deflection plates for the *Mariner* system, the sector angle of the deflection plates was increased from  $90$  to  $120$  deg to increase the number of reflections necessary for a beam of photons to reach the suppressor grid, and the resultant background electron current dropped to less than  $10^{-15}$  amp. Experience with the *Ranger* instrument at AMR, where the humidity was very high, dictated the use of insulators such as Teflon and Diall FS-4, a glass-filled diallyl phthalate, in lieu of materials such as nylon that were hygroscopic

and absorbed water in the humid environment, and thus drastically lowered important insulation resistances. Other engineering improvements in the *Ranger* design were the use of improved ground rails to reduce the number of critical high-voltage insulators, reduction of the over-all number of parts to simplify mechanical construction, and redesign of the collector cup, which reduced the number of insulator leakage paths and provided a substantial decrease (60%) in collector cup capacitance.

## B. Digital Programmer

The digital programmer receives a timing pulse from the DAS at fixed intervals, and at each interval gates a precise analog current into the high-voltage sweep amplifier to generate a discrete deflection voltage. At the end of every measurement interval, a reset pulse, which resets the binary counters to the zero state, is received from the DAS. This procedure insured synchronism of the measurement interval with the frame coding of the DAS data format and was used in lieu of an energy level identification signal which would have required more information bits.

The *Ranger* and *Mariner* programmers were essentially identical except for the number of energy levels and the data interval time. The *Ranger* system provided twelve discrete outputs and also a thirteenth step, which was identical with Step 1. This provision was to ensure that the entire system would stabilize before DAS readout if the electrometer input went from a large positive-ion current in Step 12 (2,000 v) to an electron current in Step 1 ( $-40$  v). The measurement sequence for the *Ranger* system is shown in Table 1. The *Mariner* sequence was similar except that the time interval was approximately 17 sec and there were 10 energy levels plus a reset and calibration interval (Table 3).

A block diagram of the *Ranger* programmer (Fig. 42) can be correlated with the *Mariner* programmer schematic (Fig. 43). Reset gate circuitry (transistors Q28 through Q30) was incorporated into one of the *Ranger* programmers to allow synchronization of all the sweep voltages in the absence of the DAS in a systems test operation. Transistors Q16 through Q23 formed a four-stage counter which was triggered by the DAS timing pulse through pulse amplifiers and shapers Q24 and Q25. The flip-flops used were flown on *Pioneer III* and *IV* (Ref. 20) and were used here because of the proven design reliability. The outputs of the counter were examined by a multiple AND gate diode matrix using the standard binary-to-decimal conversion technique. Transistor gates

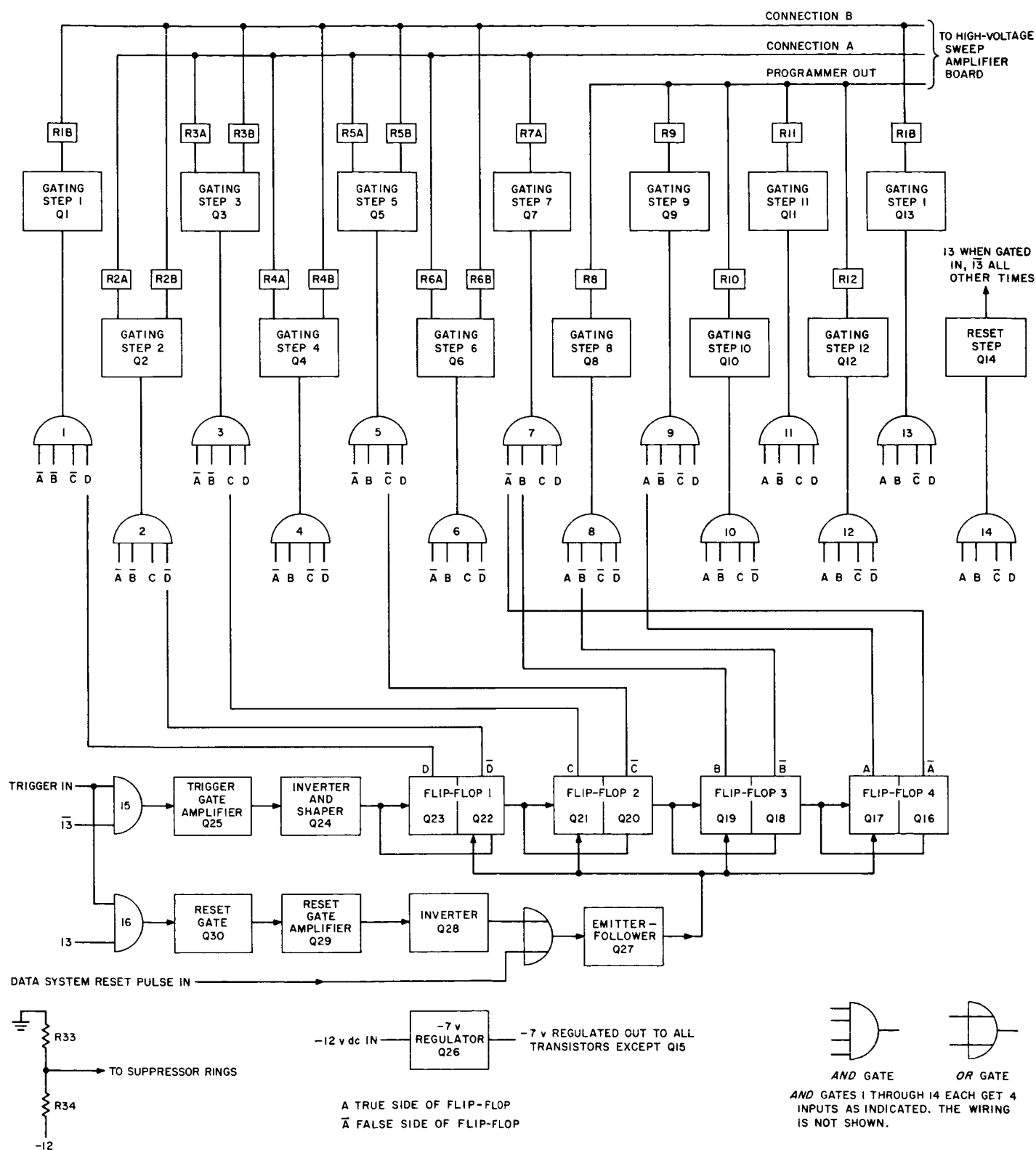


Fig. 42. Ranger programmer block diagram

Q1 through Q13 (Q1 through 10 on *Mariner 2*) switched a regulated reference voltage to resistive weighting networks to form the sweep amplifier analog input currents. On *Mariner*, no input voltage was gated to the sweep amplifier in Step 11 (Q11), as will be explained, and Step 12 (Q12) provided gating for the electrometer calibration reed-switch coil.

Since the programmer output circuitry is direct-coupled and since it was desired to keep the sweep analog input currents stable within a few percent over the specified operating temperature range ( $-20$  to  $+80^{\circ}\text{C}$ ), an effort was made to compensate for the temperature variations of diodes in the signal path. Figure 44 shows the compensation technique used to stabilize the sweep analog input currents. The compensated zener diode (CR110) is a selected precision reference with temperature coefficient of better than  $0.004\%/^{\circ}\text{C}$  at a bias current of slightly less than 1 ma. Diodes CR111 and CR112 buck out the offset and temperature variation of the base emitter diode of Q15 and the blocking diode (CR1) associated with the gate transistor (Q1). A resistive divider (R82, R88, and R85) is used to adjust the absolute value of the input voltage, and after a series of temperature runs, a silicon resistor (R88) is selected to compensate for the attenuation of the divider on the temperature coefficients of diodes CR111 and 112 and for the general temperature coefficient mismatch of all components involved. The diodes (CR2) connected from the gating transistor collector to ground clamp the cutoff voltage of the OFF gates, limiting the back voltage on the blocking diodes and thus minimizing the total leakage current errors from those gates that are off. Resistors  $R_a$ ,  $R_b$ , and  $R_c$  are designed for the proper transfer impedance for a particular sweep amplifier input current, and in addition are constrained so that the resistance seen by the individual blocking diodes is identical. As a result, the current through the individual blocking diodes is almost independent of signal current, the voltage rise across all diodes is the same and, therefore, the voltage appearing at the input resistor on any step will be approximately the same (about 7.0 v).

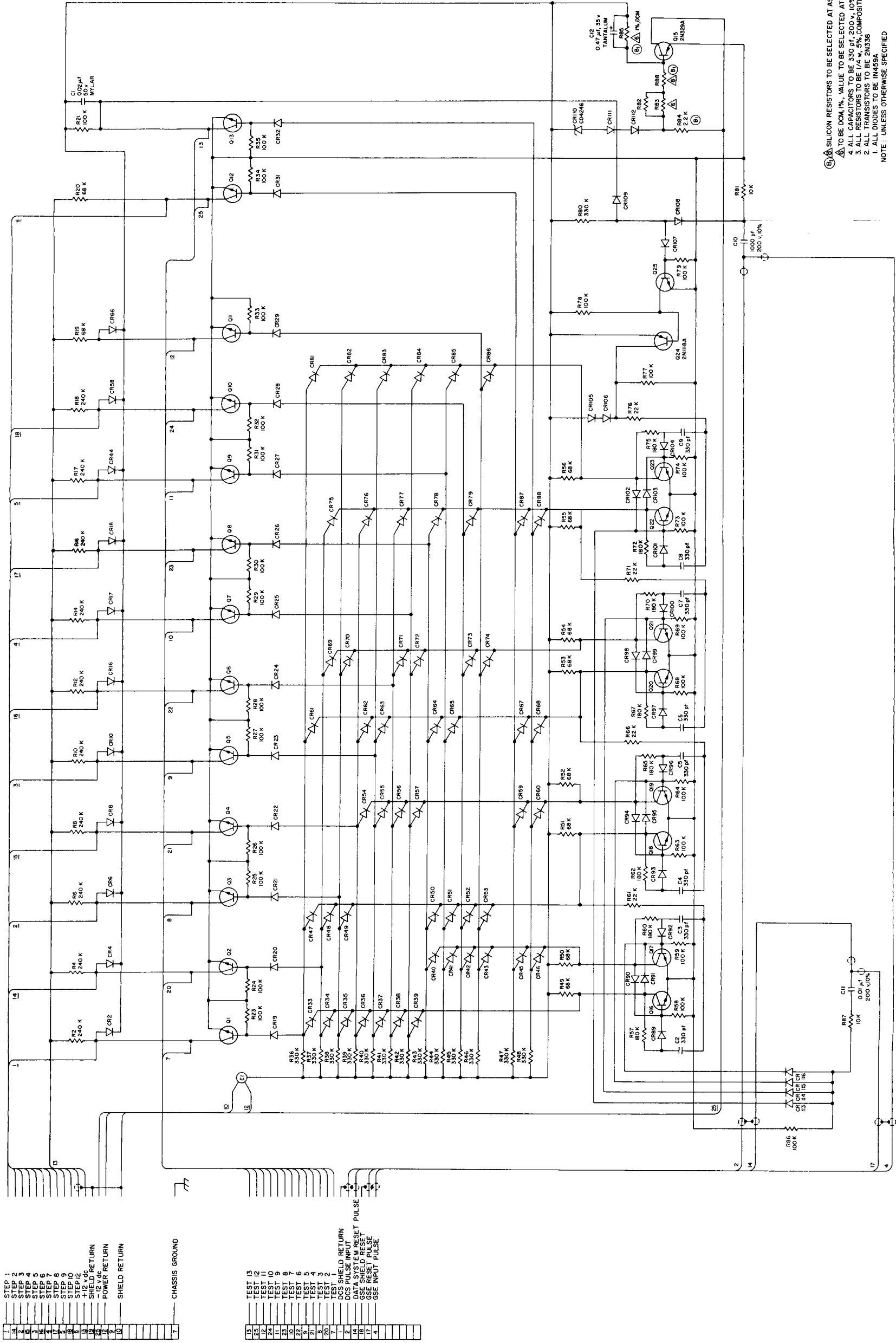
Another advantage of the resistive T networks is that although the transfer impedance varies greatly (almost two decades) through a cycle, the effective  $\beta$  network of the sweep amplifier feedback loop remains a constant, and consequently the loop gain ( $A\beta$ ) of the sweep amplifier remains constant. The following figures illustrate the change in voltage at the input of the resistor network on Step 1 at the initial setting and at temperature extremes on a typical flight programmer:

Temperature $^{\circ}\text{C}$	$E_{\text{Step 1}}, \text{v}$	$\Delta E_{25^{\circ}\text{C}}, \text{mv}$
+80	-6.965	+21
+25	-6.986	+19
-20	-6.967	

Since these deviations are only a  $-0.3\%$  and a  $-0.27\%$  change from the  $25^{\circ}\text{C}$  value, they are considered satisfactory, as the allowable deviation of any deflection voltage about the  $25^{\circ}$  value was  $\pm 5\%$ . In more recent programmer designs, use of a reference zener diode with a tightly controlled absolute value has eliminated the need for the resistive divider and the resultant thermal tracking problems.

### C. High-Voltage Sweep Amplifier

The high-voltage sweep amplifiers used on *Mariner* and *Ranger* were identical except that the *Ranger* system used two subsidiary amplifiers for stable generation of the low-voltage steps. (For comparison of ranges, see Tables 2 and 3.) Figure 45 illustrates the logic arrangement of the *Ranger* sweep system. The main sweep amplifier portion of the block diagram is identical for both systems. The large dynamic range required by the *Ranger* system ( $-20$  to  $+1,000$  v, one side to ground) suggested the use of a transformable ac system. In order to avoid the effects of various drifts arising in dc input stages and thus achieve reasonable thermal gain stability ( $<10\%$ ) in the low-voltage steps, a carrier-type operational amplifier was considered. Subsequent investigation of the carrier approach revealed that the most critical part of this design would be the chopper itself. Although much had been written about the static offset parameters of chopper transistors, very little was known or had been published about the mechanics of dynamic offset parameters such as switching spikes. In addition, thermal and long-term stability of leakage currents in the choppers then available was poor, owing to the lack of surface treatment found in present-day choppers. Although this design approach was recently achieved through the advances in (1) chopper transistor technology, (2) use of wide-band amplifiers with low hangover and blocking characteristics, and (3) duty-cycle action between modulator and demodulator to cancel the switching spikes, it was not a feasible approach at the time of the *Ranger* development. Instead, a direct-coupled operational amplifier, with a balanced differential output, was used for generation of voltage steps of  $+32$  to  $+1,000$  and  $-32$  to  $-1,000$  v, and a pair of three-stage, direct-coupled, feedback-biased operational amplifiers generated voltage



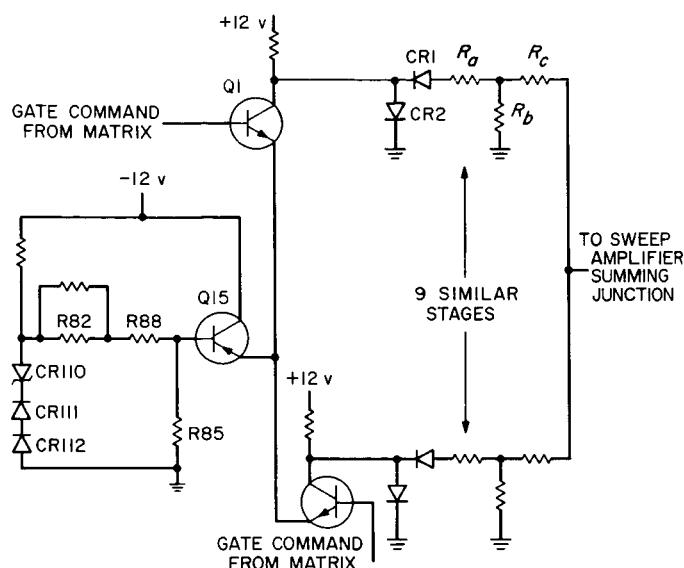


**Fig. 44. Partial schematic diagram of programmer reference and sweep amplifier input**

steps of  $-20$  to  $+10$  and  $+20$  to  $-10$  v (Fig. 46). A temperature-compensated diode isolation circuit was utilized so that the deflection plates were clamped to the subsidiary amplifiers for the low-voltage steps and to the main sweep amplifier for the high-voltage steps. Use of forward biased diodes (CR6 and CR7) in series with the outputs of the subsidiary amplifiers provided adequate temperature compensation for the voltage variation of the blocking diodes (CR7 and 8, CR12 and 16). During the subsidiary amplifier portion of the sweep cycle, the normally positive output of the main sweep amplifier was allowed to cut off, leaving the junction of R33 and R34 at approximately  $-30$  v, thus clamping the positive or outer deflection plate to the subsidiary amplifier. With the exception of the polarities involved, the inner deflection plate sweep circuit worked in a similar manner.

The main sweep amplifier used on *Ranger* and *Mariner* (Fig. 47) was a direct-coupled operational amplifier which relied on a balanced differential input stage for null stability. The input stage (Q1 and Q2) is followed by a stage of voltage gain (Q3) succeeded by two stages of power gain (Q4 and Q5) which drive a transistor-saturable-core oscillator. The oscillator drives a balanced voltage-doubler network (CR16, 17, 18, 19, and C4, C5 on the positive side) such that output voltages of equal magnitude and opposite polarity, which are proportional to the oscillator input drive voltage, are obtained. An opposite-polarity bucking voltage is placed in the charging paths of both sides of the balanced voltage in such a way that each single-ended output voltage of the sweep

amplifier is equal to the algebraic sum of the bucking voltage and the output voltage doubler. For a given deflection voltage, the closed-loop system then forces the static inverter output to a value equal to the given voltage plus the bucking voltage magnitude. This allows the saturable-core oscillator to operate with reasonable efficiency at the lower deflection voltages, increases the frequency of oscillation at the lower deflection voltages so that fairly small capacitors can be used for high-voltage ripple filtering, and conveniently allows the high-voltage amplifier to operate with a null output without danger that the loop will open because of static inverter cutoff.

The balanced, half-wave rectifier that was used for the offset voltage on *Ranger* had a 26-v rms, 2,400-cps, sinusoidal, spacecraft power supply. Some difficulty was experienced in designing an efficient voltage step-up transformer at this frequency because of the large excitation losses and the small secondary current demand. It was determined that *Mariner 2* would use a 100-v peak-to-peak, 2,400-cps, 5- $\mu$ s rise time, square-wave power supply in order to provide greater spacecraft conversion efficiency. To ease the complexity of the step-up transformer design problem, a balanced half-wave voltage doubler was adopted. On the *Mariner* system, the negative bucking voltage in the positive output side was generated by C2 and C6 and by CR46 and CR14.

Inspection of Fig. 47 reveals that the amplifier feedback loop is single-ended so that the system error signal is provided by the positive output side alone. This design approach assumes reasonable thermal tracking of both sides of the static-inverter voltage doubler and demands that the outputs of the bucking supply be of equal magnitude in order to obtain a symmetrical output of the over-all sweep amplifier. This is reasonable since the negative-output side is a mirror image of the positive output about the ground center line. During operation of the system in the space environment, all charged particles that enter the deflection system and are not focused onto the collection cup impinge on the deflection plates and form a current that must be absorbed by the power supply. An electron current that is absorbed on the positive plate and that is larger than the idling current through R49 minus the feedback current will develop a voltage across R49 sufficiently large to keep diode CR46 reverse-biased during its normal charging cycle. As the current increases, the bucking voltage across R49 increases. Since the negative bucking voltage is inside the amplifier feedback loop, the system would force the static inverter output upward to maintain the

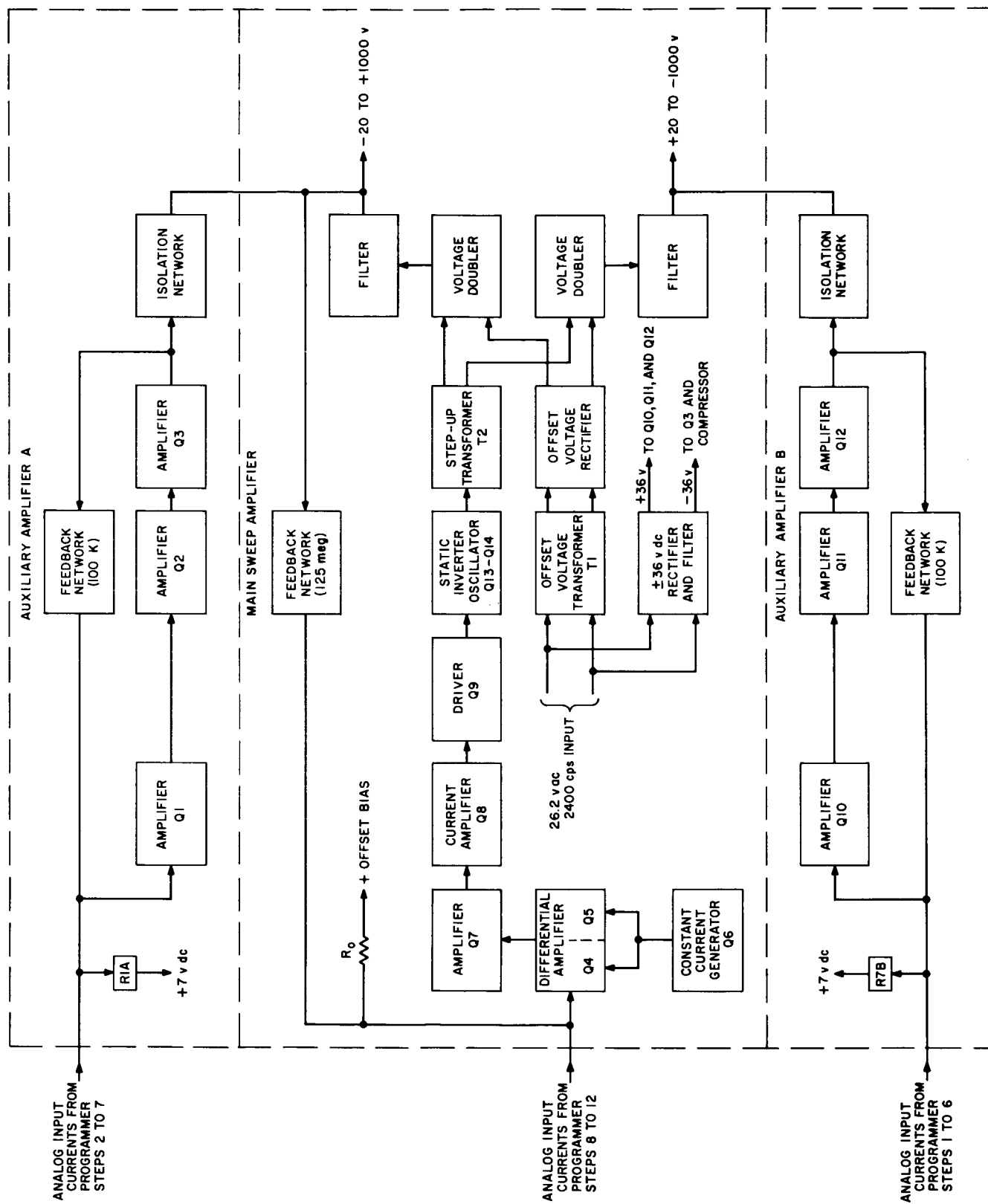
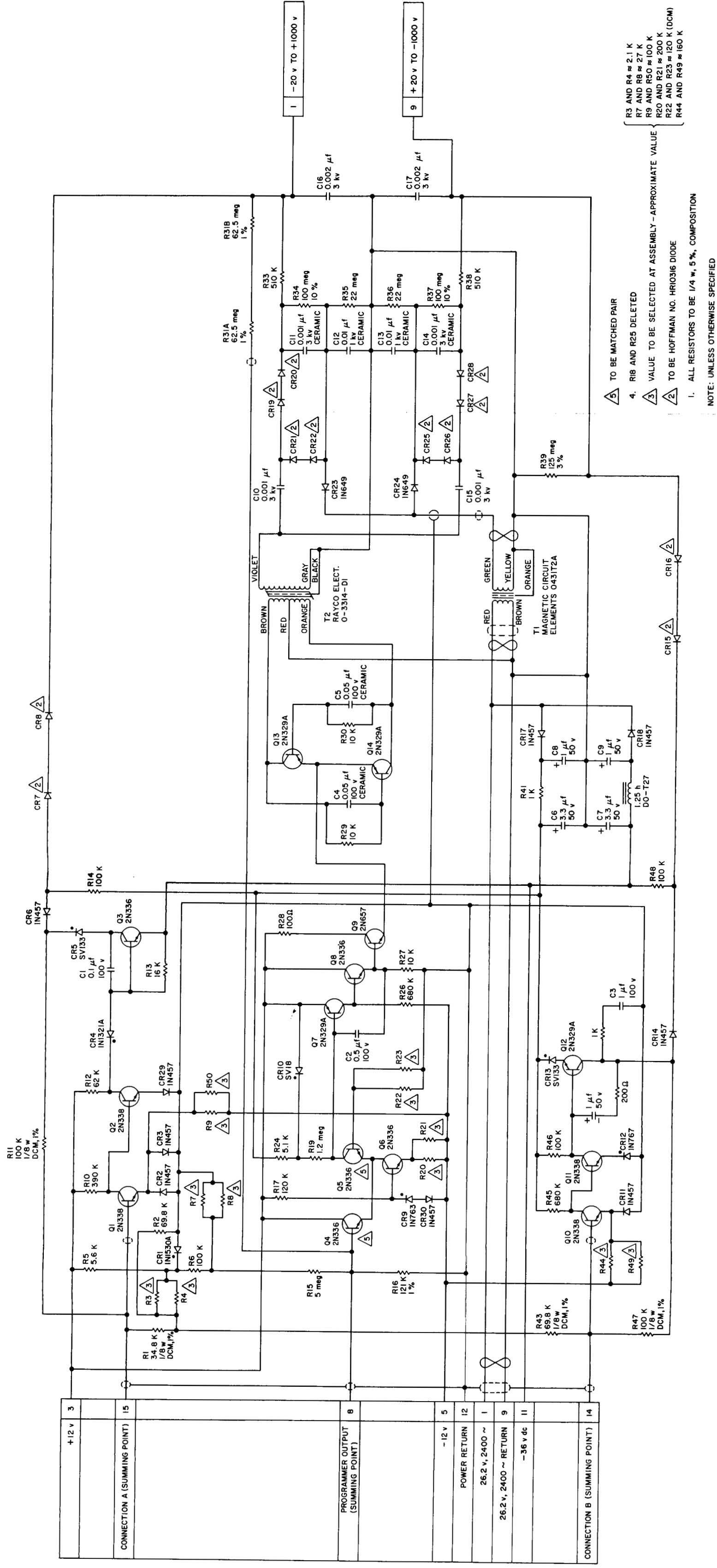


Fig. 45. Ranger high-voltage sweep amplifier block diagram



**Fig. 46. Ranger sweep amplifier schematic diagram**



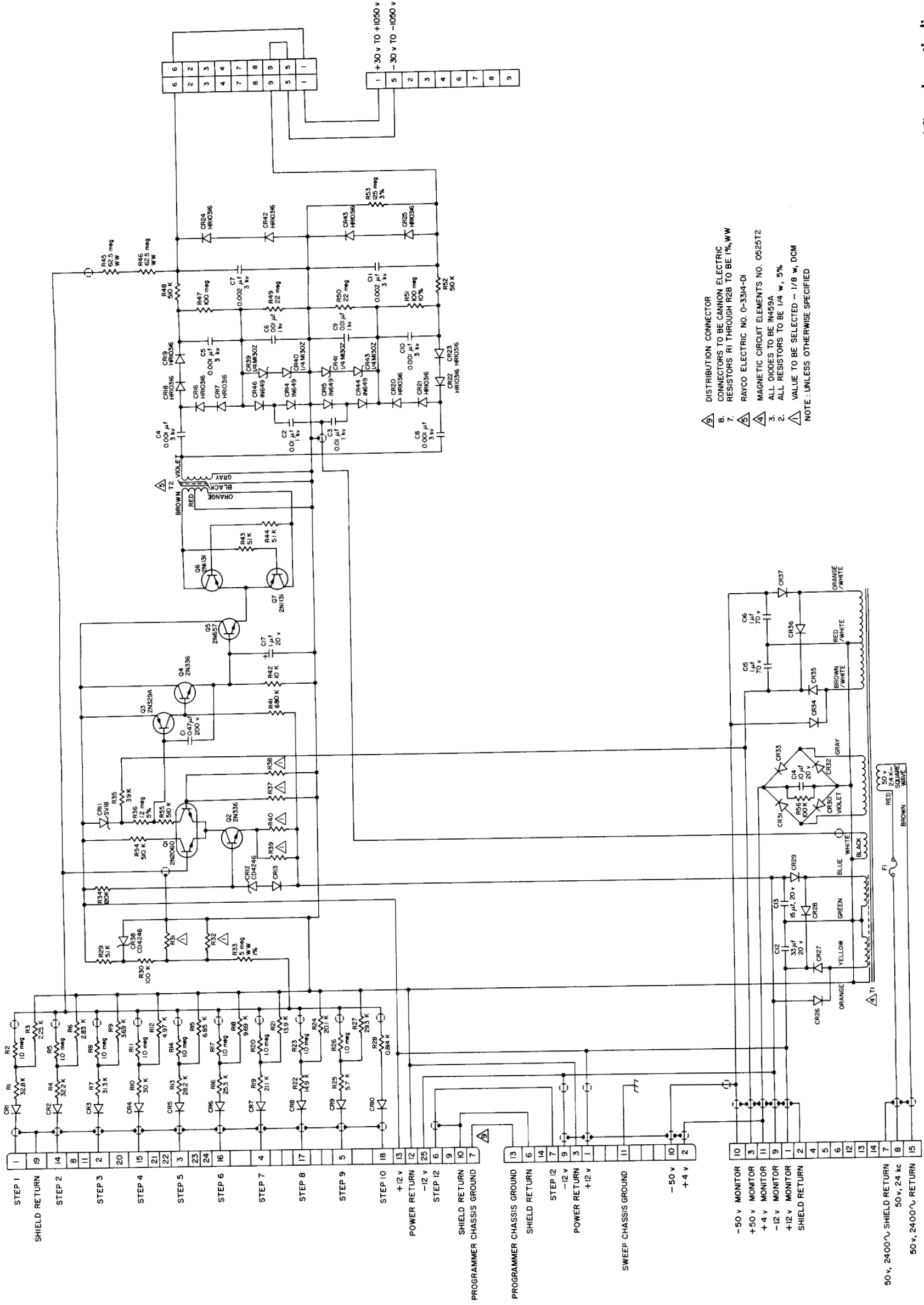


Fig. 47. Mariner sweep amplifier schematic diagram

given positive deflection voltage. Accordingly, the negative output of the static inverter increases and, since its offset voltage will remain constant, a nonsymmetrical system output will result. Zener diodes CR39 and 40, whose total threshold is slightly above the normal offset potential, limit voltage buildup on R49 to the zener breakdown voltage and so tend to keep the offset voltage symmetrical. At the +30-v output, either side of the system could sustain an injected loading current of 100  $\mu$ a with less than a 1-v unbalance.

Positive-ion current on the positive plate has a similar, though inverse, effect. In this case, the idling current of interest is delivered to R47 by the voltage-controlled oscillator and is a variable given by

$$\frac{E_o - E_{\text{buckling}}}{R_{47}} + \frac{E_o}{R_f}.$$

Inverse current in excess of this value will develop a voltage across R47 that will reverse-bias diodes CR18 and CR19. At the +30-v output, the outer plate could sustain an inverse or unloading current of 2.5  $\mu$ a before disconnecting rectifier diodes CR18 and CR19.

Diodes CR24 and 42 (CR43 and 25 on the negative side) clamp the output of the system to a small potential during the instrument reset and calibration periods. During Steps 11 and 12 in the *Mariner* scan cycle, all negative signal currents to the sweep amplifier are disconnected, and a fixed positive-input reference (which will be discussed below) forces the system outputs to the opposite polarity. The diodes then become forward biased, clamping the output, and the error signal increases and forces the static inverter to cut off. The offset supply then keeps the diodes in this condition, and charged-particle loading of the deflection plates can alter the resultant voltages only within the limitations of the conduction characteristics of the diodes. The resultant deflection voltage (-1.4 v dc) corresponds to electron energies of 5.6 ev and thus assures negligible interference with calibration current injected into the electrometer during the twelfth step.

Capacitor C1, which is bootstrapped about transistors Q3 and Q4, in combination with the Thevenin impedance looking from the junction of the capacitor with the base of Q3, provides the dominant pole that rolls off the open-loop response at 6 db per octave. This pole occurs at approximately 0.04 cps as illustrated in a measured loop-transmission characteristic (Fig. 48). The zero frequency  $A\beta$  is greater than 200, which is more than

adequate for 1% transfer function accuracy. This curve was obtained by placing an isolated dc or sinusoidal source in series with the positive output and the feedback resistor in the same manner as described in the electrometer evaluation. Care was exercised during the test to ensure that the output signal was a symmetrical sinusoid throughout the measurement. This waveshape is essential since a signal that tends to rapidly drive the positive output to a less positive value will be rate-limited by the output filter networks. The feedback loop will rapidly force the static inverter to a smaller value, the charge retained on the filter capacitor C5 will reverse-bias diodes CR18 and 19, and the loop will intermittently open; the resultant output will then be distorted owing to rate limiting. Since the deflection voltages consistently increased in magnitude during the measurement cycle and the system was always in a linear mode, this distortion did not occur. The rise time for a step-function input that drives the output from +5 to +50 v is 70 msec. Since the electrometer was allowed to settle out for one interval between the 1,050-v step and the calibration interval, the decay time of approximately 400 msec offered no problem.

The ultimate null stability of the sweep amplifier depends on the tracking characteristic of the balanced differential input stage. Changes in differential input currents and imperfect tracking of the base-emitter diode voltages of the comparator transistors are the most significant factors in the cause of output voltage drift. Current drift effects in the input stage are minimized by making the Thevenin equivalent resistance of the input networks (R1 through R33, Fig. 47) and feedback resistors (R45, 46) equal to the parallel combination of the reference base resistors (R37, 38). Assuming balanced collector currents and  $\beta$ -tracking of the comparator transistors, input current changes due to  $\beta$  variation cause common-mode signals and are not a significant factor in output drift. To ensure common-mode stability, a thermally compensated constant-current source consisting of Q2, CR12, CR13, and R39 and 40 is used. This thermal stabilization is essential, as any change in the current source must be absorbed by the input transistor of the comparator stage and will then cause input drift currents, since the output or referenced side has a regulated collector load. Diode CR12 is a low-temperature coefficient reference zener, and diode CR12 is used to compensate the base-emitter diode variation of Q2 in such a way as to maintain a constant voltage across R39 and R40, and hence a constant current. The current source proved to be stable to within 3% at a collector current of 30  $\mu$ a over a 100°C temperature range. In the

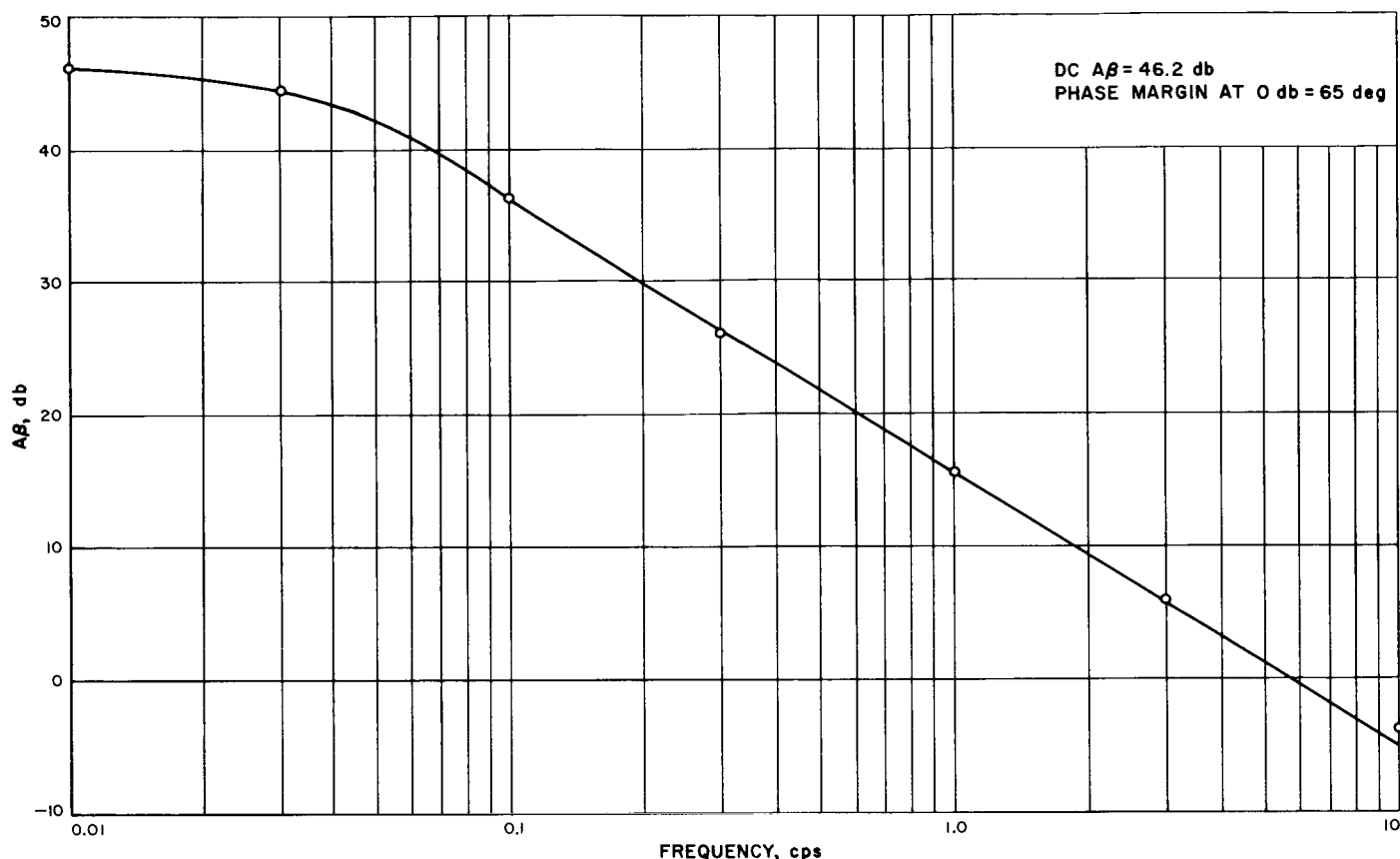


Fig. 48. Mariner sweep amplifier loop transmission response

initial adjustment procedure, the parallel combination of resistors R39 and 40 was selected for balanced comparator collector currents of approximately  $15 \mu\text{a}$ . In order to avoid variations in the collector current of the comparator output stage owing to base-emitter voltage variation of the subsequent PNP transistor (Q3) across the collector load resistor, a semi-stable current source was formed by R35, zener diode CR11, and collector load resistor R36. Resistors R54 and R55 were added to the Mariner design to equalize the collector operating voltages and thus achieve balance of the collector leakage currents.

The comparator transistors used in the early *Ranger* designs were 2N336 transistors and were carefully selected for matching characteristics; that is, the various values of  $V_{BE}$  and the current gains were matched at collector currents of  $15 \mu\text{a}$ . In addition, collector leakage currents were matched at a  $V_{CE}$  value of 12 v. Although this procedure was successful, the long-term results were not always so, since individual units tended to degrade with time. The advent of the passivated planar transistor in the fall of 1960 provided a solution to this problem.

A special unit was obtained which contained two 2N1613 transistors in a single TO-5 case (Fairchild FSP-2). This unit had a higher  $\beta$  and a leakage current lower by an order of magnitude than that of the available 2N336's. The common heat sink also contributed markedly to improved thermal tracking of the comparator stage. By the completion of the Mariner development, the superior 2N2060 was available as a standard (and cheaper) component. The irony of electronic design is that when a project reaches the production phase, having taken up to a year in development depending on the complexity of the task and the available manpower, components inevitably become available which make the present design obsolete since they permit vast simplification or increased performance.

Because of the small available input voltages, the large dynamic output range, and the necessity to avoid excessive power dissipation in the feedback resistor, the feedback attenuation

$$\frac{R_S}{R_S + R_F}$$

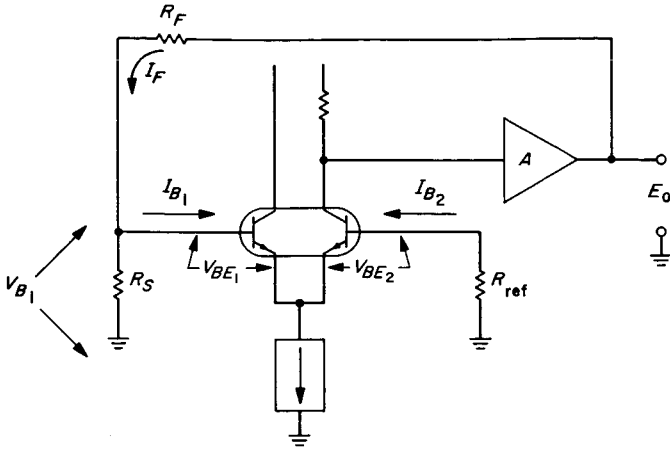


Fig. 49. Main sweep amplifier equivalent circuit

where

$R_S$  = Thevenin equivalent resistance of all input and bias networks

$R_F$  = sweep amplifier feedback resistance

became very small and thus magnified the effects of drift in the input stage. The effects of comparator current and base-emitter voltage drifts on the output may be studied with the aid of Fig. 49. In this equivalent circuit, the input networks have been replaced by their equivalent resistance  $R_S$ . It may be shown that

$$V_{B1} = (I_F - I_{B1}) R_S$$

and

$$V_{B1} = V_{BE1} - V_{BE2} - I_{B2} R_{ref}$$

so that

$$I_F = \frac{I_{B1} R_S - I_{B2} R_{ref} + \delta V_{BE}}{R_S}$$

where

$$\delta V_{BE} = V_{BE1} - V_{BE2}$$

The output voltage is given by

$$E_o = I_F R_F + V_{B1}$$

Assuming

$$V_{B1} \ll I_F R_F$$

then

$$E_o = (I_{B1} R_S - I_{B2} R_{ref} + \delta V_{BE}) \frac{R_F}{R_S}$$

and

$$\frac{\partial E_o}{\partial T} = \left( \frac{\partial I_{B1}}{\partial T} R_S - \frac{\partial I_{B2}}{\partial T} R_{ref} + \frac{\partial(\delta V_{BE})}{\partial T} \right) \frac{R_F}{R_S} \quad (45)$$

assuming

$$\frac{\partial R_S}{\partial T} = \frac{\partial R_{ref}}{\partial T} = 0.$$

Since  $R_S = 111 \text{ K}$  and  $R_F = 125 \text{ meg}$ , it is seen that the algebraic sum of the voltages around the comparator base-emitter loop that are due to input drift current and improper diode voltage tracking is reflected to the output by a factor of about 1,000. It is realized that the incremental variation of base currents and base-emitter voltages is not a linear function over a wide temperature range. Equation (45) is generalized, therefore, in terms of the total change of these parameters over a large temperature excursion.

For

$$\frac{\Delta E_o}{\Delta T} \rightarrow 0$$

$$\Delta I_{B1} R_S - \Delta I_{B2} R_{ref} = -\Delta(\delta V_{BE}). \quad (46)$$

From this result, it can be shown that the small base-emitter tracking errors can be compensated by the differential base current drift by variation of resistor  $R_{ref}$  with respect to  $R_S$ . For a representative 2N2060 at  $I_C = 15 \mu\text{a}$ , variations of these parameters from  $-25$  to  $+75^\circ\text{C}$  are as follows:

$$\Delta I_{B1} = 0.10 \mu\text{a}$$

$$\Delta I_{B2} = 0.14 \mu\text{a}$$

$$\Delta(\delta V_{BE}) = 2.6 \text{ mv.}$$

Substituting these parameters in Eq. (46),

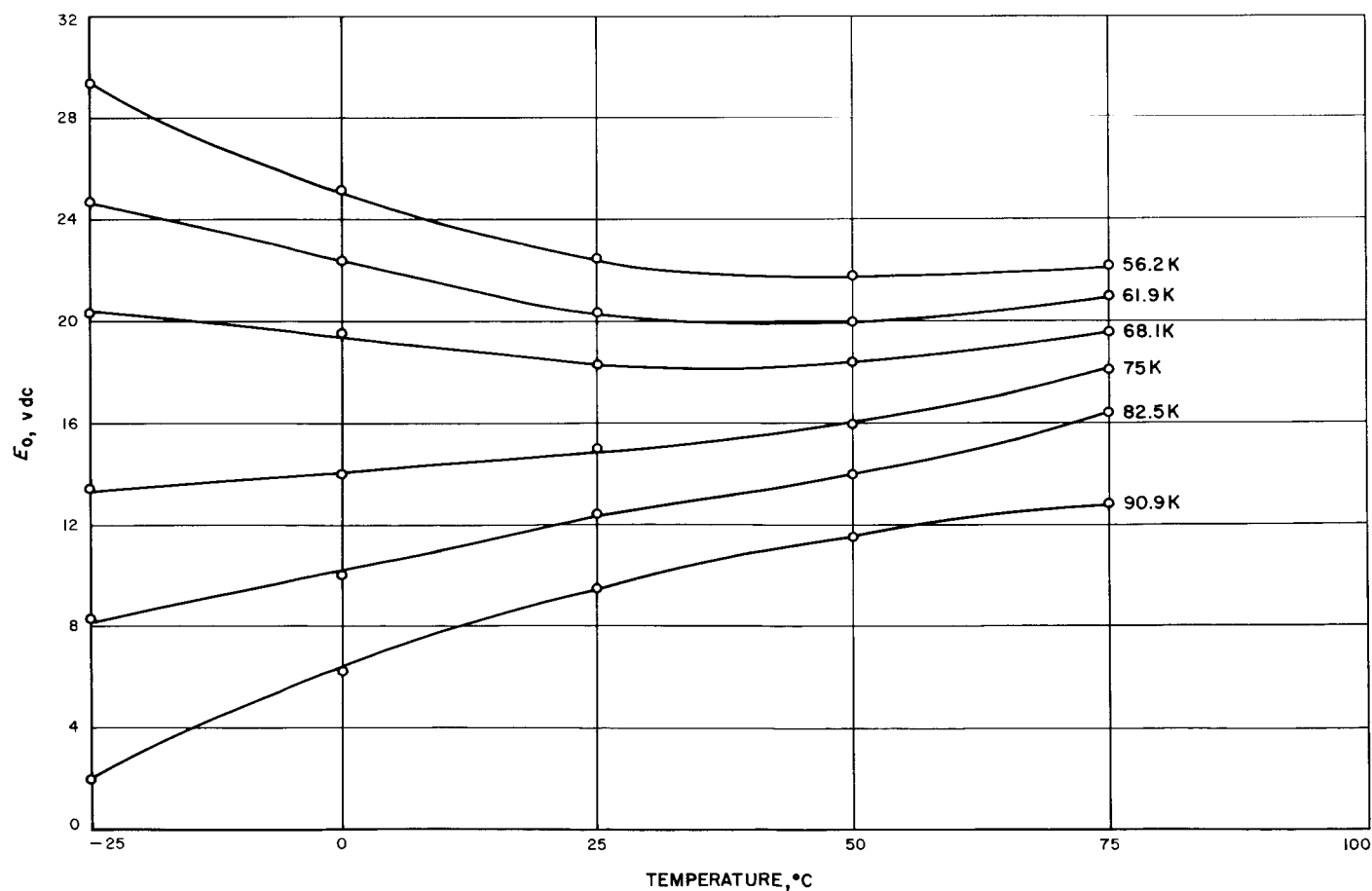
$$0.10 \times 10^{-6} \times 111 \times 10^3 - 0.14 \times 10^{-6} \times R_{ref} = -2.6 \times 10^{-3}$$

and

$$R_{ref} = 97 \text{ K.}$$

Table 8. Output voltage vs. temperature for *Ranger* sweep system

Energy-level step	Voltage, v			Energy-level step	Voltage, v		
	0°C	25°C	70°C		0°C	25°C	70°C
Positive				Negative			
1	-20.4	-20.3	-20.1	1	+20.5	+20.3	+20.0
2	-10.1	-10.1	-10.1	2	+10.2	+10.1	+9.9
3	-4.9	-5.0	-5.0	3	+5.4	+5.25	+5.0
4	-2.6	-2.7	-2.7	4	+2.7	+2.6	+2.4
5	+2.7	+2.55	+2.55	5	-2.2	-2.3	-2.5
6	+5.0	+4.85	+4.8	6	-4.7	-4.8	-5.0
7	+10.1	+10.0	+10.0	7	-10.0	-10.0	-10.1
8	+32	+32.5	+33	8	-31	-31	-32
9	+76	+76	+77	9	-74.5	-75	-76
10	+180	+181	+183	10	-179	-180	-181
11	+422	+425	+425	11	-422	-425	-425
12	+1000	+1000	+1000	12	-995	-1000	-995

Fig. 50. Thermal drift characteristics vs. reference base resistor for typical *Mariner* sweep amplifier

After the comparator collector currents are balanced in the sweep amplifier alignment procedure, the output voltage is recorded vs. temperature for different values of  $R_{ref}$ . A family of curves that depicts the test result for a typical *Mariner* sweep amplifier is shown in Fig. 50. It is seen that the flattest output characteristic over the 100°C temperature range was provided by a 68.1-K resistor. This corresponds to an average equivalent input drift of 20  $\mu\text{V}/^\circ\text{C}$ . Since this adjustment resulted in a stable output offset, a reference base resistor of the proper value was installed, the precise analog current was gated in on the first step (corresponding to 30 v

output), and a regulated input bias current was adjusted to give the correct output voltage. The regulated bias voltage is supplied by reference zener diode CR38 with an adjustable voltage divider R30 through R32, and the bias current is produced by R33. The temperature test is then rerun to prove the validity of the adjustment.

For a typical *Ranger* sweep amplifier (the *Mariner* design was similar) the output voltage is given vs. temperature and energy-level step in Table 8. The *Mariner 2* sweep amplifier calibration is presented in the next section, which describes preflight performance.

## V. THE MARINER 2 FLIGHT INSTRUMENT

### A. Preflight Calibrations

Four solar plasma instruments were built in preparation for the two 1962 launchings to Venus. Construction on the third unit, which was to fly aboard *Mariner 2*, was completed on February 9, 1962. Flight acceptance environmental tests were conducted between February 25 and March 5, 1962, during which time temperature, vibration, and vacuum-temperature performances were monitored. Between March 5 and May 8, 1962, the flight instrument was alternated with other plasma units for spacecraft systems tests. When not on the spacecraft, each unit was returned to the laboratory for routine calibrations and performance checks. The history of each unit as recorded in its log book provided an abbreviated yet effective instrument life test and burn-in record.

Vacuum-temperature tests were once again performed on May 8, 1962, and shortly afterward unit No. 3 was shipped with other spacecraft elements to AMR. Final laboratory calibration was performed on August 5, 1962, followed on the next two days by the last spacecraft systems test. The last useful data observed were electrometer calibrations taken in the explosive-safe area on August 14, 1962, prior to the move to the launching

pad. The next message from the instrument did not occur until August 29, 1962, about 2½ days after launch, when *Mariner 2* scientific instruments were turned on.

The curves and tables presented here describe the preflight performance of various parts of the *Mariner 2* solar plasma instrument. Figure 51, for instance, shows the result of final adjustment to the electrometer secondary feedback. Part of the logging operation, which started after completed construction of each unit, consisted of monitoring important instrument performance parameters and power supply levels in addition to the customary calibrations. Table 9 presents results of characteristic measurements taken in the 4-month period prior to launching. The mechanical resonance of the dynamic capacitor is measured by the frequency of its feedback-driven oscillator. The importance of this measurement is that large increases in frequency with time are indicative of leaks in the modulator vacuum seal, which suggest damping effects such as reduction in conversion efficiency and alteration in mechanical  $Q$ . Acceptance standards for frequency stability were based upon statistical data obtained from *Ranger* instrument modulators. During this period of time, loop gain variations were within +1.6 and -3.7 db of the nominal

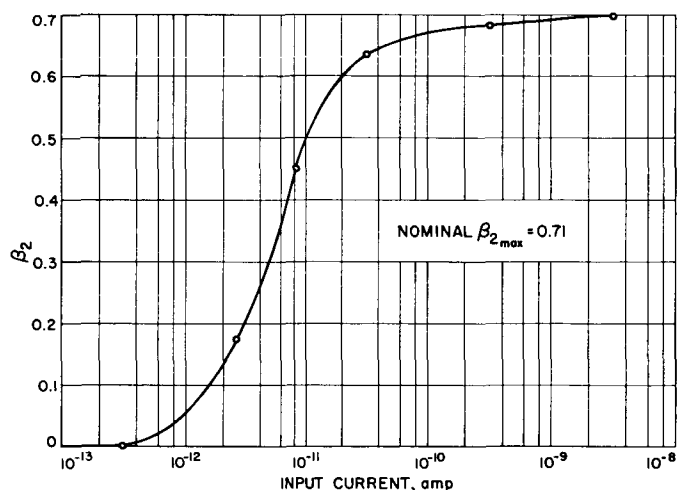


Fig. 51. Portion of secondary feedback connected ( $\beta_2$ ) vs. input current

60 db. Input error signal potentials were, therefore, about +2 mv for the tabulated values at input currents of  $10^{-6}$  amp. As a result, if -2-mv corrections are made to tabulated values of  $V_{in}$ , one has a thermal and temporal history of modulator contact potential. In most of the formal thermal tests of each flight unit, the instrument's temperature stabilized near that of the chamber wall or near the ambient temperature, depending upon which was controlled. Wherever possible, chassis tem-

peratures were recorded. Where results are listed for tests at atmospheric pressure with no chassis temperatures recorded (e.g., spacecraft systems tests), it is safe to assume a chassis temperature within a few degrees centigrade of the recorded ambient temperature. The final temperature listed in Table 9 (these values also appear in Tables 10 and 11) were somewhat different from the previous test values, because the instrument and its handling fixture were attached to a Plexiglas wall of a rollable vacuum chamber at AMR, and no internal thermal control was provided.

The curves of Fig. 52 provide the basic temperature calibration for the electrometer system, but for final adjustment they must be normalized to the last temperature calibration (columns 2 and 3 of Table 10). The effective translational drift of calibrations between May 8 and August 5, 1962, was about 8 mv.

During each spacecraft systems test a fixture attached to the plasma instrument permitted remote sequencing of electrometer calibration currents. During these tests, outputs from both the electrometer and the analog-to-digital converter of the spacecraft science Data Conditioning System (DCS) were monitored. The results of these measurements on the last systems test (August 7, 1962) are listed in columns 4 to 7 of Table 10. Differences between readings taken on ground support equip-

Table 9. Preflight electrometer performance

Date	Modulator frequency $f_0$ , cps	Loop gain $F_0$	$V_{in}$ at $I_{in} = 10^{-6}$ amp mv	Temperature <sup>a</sup> °C	Pressure Torr
5/8/62 (JPL) ↓	2,259.7	1,150	-26.5	+24	1 atm
	2,259.4	1,150	-26.1	+26	$10^{-4}$
	2,259.3	650	-25.4	-9	$2 \times 10^{-5}$
	2,261.1	1,110	-25.8	+68	$2 \times 10^{-5}$
	2,258.8	1,130	-28.4	+24	$10^{-5}$
	2,259.1	1,110	-29.7	+23	1 atm
6/28/62 (AMR) ↓	2,260.5	1,080	-25.3	A+25 <sup>b</sup>	1 atm
	2,260.9	730	-21.6	A-20	↓
	2,262.0	910	-25.5	A+70	
	2,260.0	1,051	-23.8	A+25	
8/5/62 (Final at AMR)	2,260.8	1,110	-28.0	+28	1 atm
	2,260.2	1,200	-23.7	+40	$1.3 \times 10^{-4}$

<sup>a</sup> Unless otherwise noted, all temperatures are those at the instrument chassis.

<sup>b</sup> A denotes ambient temperature.

Table 10. Final preflight electrometer calibrations

$I_{in}$ amp	Final instrument calibration <sup>a</sup> $E_0$ , v		Final spacecraft systems test <sup>b</sup>				Equivalent spacecraft calibration, <sup>c</sup> referenced to:	
	At atmospheric pressure <sup>d</sup>	In vacuum <sup>e</sup>	GSE readout, $E_0$ , v	DCS readout, steps		Corresponding step center value, v	GSE ground data, v	Data system, v
				Digital output in octal numbers	Digital output in decimal numbers			
$10^{-6}$	1.831	1.835	1.812	115	77	1.810	1.812	1.818
$10^{-7}$	2.120	2.125	2.106	132	90	2.115	2.102	2.108
$10^{-8}$	2.375	2.380	2.352	144	100	2.350	2.357	2.363
$10^{-9}$	2.618	2.624	2.594	156	110	2.590	2.601	2.607
$10^{-10}$	2.854	2.861	2.830	171	121	2.844	2.838	2.844
$10^{-11}$	3.073	3.095	3.040	202	130	3.055	3.072	3.078
$10^{-12}$	3.219	3.324	— <sup>f</sup>	—	—	—	3.301	3.307
$10^{-13}$	3.261	3.545	—	—	—	—	3.552	3.528
$10^{-10}^g$	2.855	2.860	2.832	171	121	2.844	2.837	2.843

<sup>a</sup> At AMR laboratory, 8/5/62.<sup>b</sup> At AMR, 8/7/62. Ambient temperature, 23°C; pressure, 1 atm.<sup>c</sup> Translated calibration of 8/5/62. Ambient temperature, 23°C; pressure,  $1.3 \times 10^{-4}$  Torr. This calibration assumes chassis temperature equal to ambient temperature during systems test.<sup>d</sup> Instrument temperature, 28°C.<sup>e</sup> Instrument temperature, 40°C; pressure,  $1.3 \times 10^{-4}$  Torr.<sup>f</sup> Calibrations on the spacecraft were generally suspect at or below  $10^{-12}$  amp because of humidity effects, and therefore were not usually taken.<sup>g</sup> Internal calibration.

ment (GSE) and those taken in the laboratory are attributable principally to ground reference differentials between measurements. Verification of these grounding

differentials was obtained by comparison of GSE-based readings with direct measurements at the output of the instrument compartment (case 1 of the 6-case *Mariner* hexagonal structure). The calibration in column 8 was produced by a  $-9$ -mv translation of column-3 data, normalizing it to  $+23^\circ\text{C}$ , and another  $-14$ -mv translation of the same data to account for ground-reference differentials, a total of  $-23$  mv displacement.

The nominal scale-factor and linearity of the analog-to-digital converter in the DCS were verified by measurement of step-crossings in subsystems tests prior to the final tests on August 7, 1962. The nominal voltage at step center was given by

$$V_{nom} = 0.0235 N \quad (47)$$

where  $N$  represents the number of quantizing steps. Assuming nominal scale factor and linearity for this part of the data system, a crude 7-point statistical average was taken of the differences between the GSE voltages and the center values of the recorded DCS steps. Although offsets also exist between GSE-based voltages and those appearing at the input to the DCS, a single

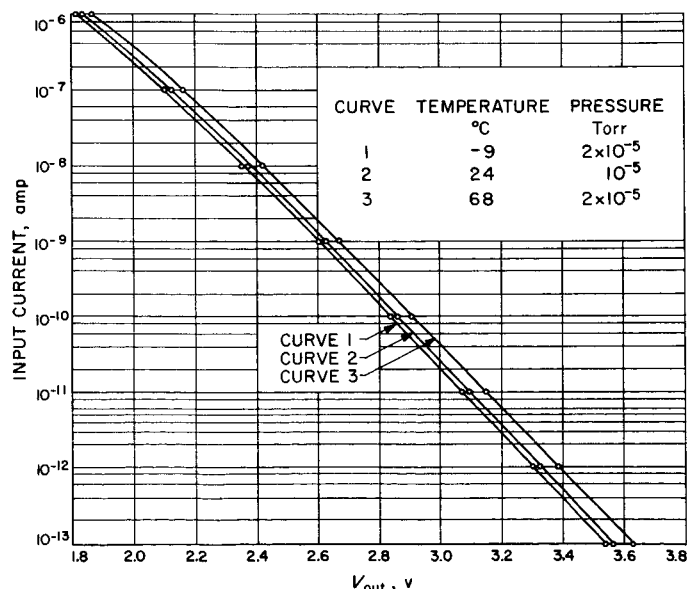


Fig. 52. Vacuum-temperature electrometer calibrations, May 8, 1962



Table 11. Preflight deflection voltage calibration<sup>a</sup>

Step	Deflection plate voltage, $v$ , for indicated conditions														
	JPL calibration, 5/8/62														
	+24°C, 1 atm		+26°C, 10 <sup>-1</sup> Torr		-9°C, 2 × 10 <sup>-3</sup> Torr		+68°C, 2 × 10 <sup>-3</sup> Torr		+24°C, 10 <sup>-5</sup> Torr		+23°C, 1 atm		Final AMR calibration, 8/5/62		
	Outer	Inner	Outer	Inner	Outer	Inner	Outer	Inner	Outer	Inner	Outer	Inner	Outer	Inner	
1	29.4	29.1	29.5	29.1	29.1	29.2	30.3	31.2	29.5	29.5	29.5	27.5	27.1	28.1	27.7
2	43.9	43.6	43.9	43.6	43.4	43.5	44.7	45.5	44.0	43.95	44.0	41.5	41.1	42.5	41.6
3	65.5	65.2	65.6	65.2	64.8	65.0	66.3	67.0	65.6	65.6	65.7	62.4	62.1	64.0	62.6
4	96.5	96.2	96.5	96.1	95.4	95.7	97.1	97.6	96.5	96.5	96.6	91.7	91.4	93.3	91.3
5	142	142	143	142	141	141	143	143	143	143	142	138	138	141	138
6	211	211	211	211	209	209	212	212	212	211	212	205	205	208	206
7	314	314	314	313	311	311	314	313	314	314	314	306	305	308	306
8	468	467	468	467	463	464	467	466	467	467	468	456	455	459	457
9	699	699	700	698	692	693	698	696	699	699	699	683	682	686	685
10	1,051	1,051	1,052	1,051	1,036	1,038	1,053	1,051	1,052	1,052	1,051	1,027	1,026	1,032	1,031
11	-0.7	+0.8	-0.7	+0.7	-0.9	+0.9	-0.5	+0.5	-0.7	+0.7	-0.7	-0.8	+0.7	-0.7	+0.7
12	-0.7	+0.8	-0.7	+0.7	-0.9	+0.9	-0.5	+0.5	-0.7	+0.7	-0.7	-0.8	+0.7	-0.7	+0.7

<sup>a</sup> Outer and inner plate voltages are positive and negative, respectively, unless otherwise indicated.

<sup>a</sup> Outer and inner plate voltages are positive and negative, respectively, unless otherwise indicated.

composite calibration characteristic can now be listed, based upon the nominal characteristic of the analog-to-digital converter (Eq. 47). This is accomplished in column 9 of Table 9 by a +6-mv translation of GSE-based calibration.

Table 11 contains preflight calibrations of deflection voltages. Scale-factor differences between readings taken on May 8 and those taken on August 5, 1962 (2%), are very likely produced by the different measurement equipment used at JPL and at AMR. Probes having nominal attenuations of 100 to 1 were used with electrometer-type voltmeters, whose analog outputs were recorded on a digital voltmeter. The offset shift can be accounted for in probe calibration.

## B. Flight Performance

*Mariner 2*, the second of a series of spacecraft designed and developed by JPL, was launched on August 27, 1962, at 1:53:14 Eastern Standard Time (EST) from AMR by the National Aeronautics and Space Administration. (*Mariner 1*, launched on July 22 from AMR, had been destroyed after approximately 290 sec of flight because of a deviation from the planned flight path.) The *Mariner 2* spacecraft (Fig. 7) was identical with *Mariner 1* and had the same mission.

### 1. General Flight Data

Of six scientific instruments carried by the spacecraft, two were used in close-range infrared and microwave measurements of the planet Venus and four performed experiments during the flight and in the vicinity of Venus and collected and transmitted information on interplanetary phenomena.

The flight to Venus lasted approximately 109 days, during which time an over-all flight distance of about 180 million miles was traversed. At Venus encounter, the spacecraft communicated its scientific data to Earth over an interplanetary distance of 36 million miles.

Radio signals from the *Mariner* spacecraft were heard for the last time by the JPL Deep Space Instrumentation Facility station in Johannesburg, South Africa, at the conclusion of its acquisition period at 2:00 a.m. EST on January 3, 1963. At that time the spacecraft was 53.9 million miles from the Earth and 5.6 million miles beyond Venus, and had traveled 223.7 million miles since launch on August 27, 1962. During the 129 days between launching and the final loss of radio contact with the spacecraft, interplanetary or cruise science instruments

operated for a total of 118.2 days, and data produced by these instruments were actually recorded by the tracking stations for approximately 104.1 days. Information on cruise science experiments was recorded without interruption for one period of 38.3 days and for three other periods of more than 9 days.

### 2. Instrument Performance

The *Mariner 2* solar plasma instrument operated successfully throughout the entire flight, in both the cruise and encounter modes.

The digital programmer that commutated different inputs to the high-voltage sweep amplifier operated normally. There was no measurement of deflection plate voltage, although plasma energy spectra do indirectly corroborate the presence of appropriate voltages. Future instrumentation should unquestionably provide at least a coarse direct monitor of deflection plate voltage.

Electrometer performance is probably best summarized by calibration history and by signal range and fluctuation patterns. Cruise science was turned on by an Earth-transmitted command on August 29, 1962 (day 241), at 16:13 GMT, about 2½ days after liftoff. The spacecraft was then Sun-oriented, rotating approximately once every 120 min about its roll axis. Earth acquisition took place on day 246, at which time the steerable directional antenna was optically pointed towards the Earth and the spacecraft roll motion stopped. (A chronology of important spacecraft events such as this is shown in Table 12; see also Ref. 21.) The first calibration change took place 6 hr after the Earth-reacquisition sequence that followed a midcourse correction. The calibration output (programmer step 12) dropped one DCS step (23.5 mv/step) in an unexplained fashion (see Table 13). On day 281, another downward shift of two DCS steps occurred. On day 315, the calibration value began increasing, and by planet encounter it had returned to 120. The expected shift for the entire flight was between two and three steps increase. Therefore, at least part of the increase in calibration value after day 315 can be explained by expected changes due to temperature. The three-step increase after day 315 denotes a shift of between 47 and 94 mv, and vacuum-temperature histories account for 36 mv.

In comparing these shifts with other spacecraft events, it was noted that the science temperature measurement for the magnetometer shifted about 1.2 DCS steps on day 281. The engineering temperature measurements did not record a similar shift. Since the magnetometer temperature is measured on a seven-bit channel, this

**Table 12. Spacecraft events affecting cruise science<sup>a</sup>**

No.	Event	Day	Cruise-science OFF time <sup>b</sup>		
			days	hr	min
1	Liftoff	239	2	9	20
2	Cruise science on	241			
3	Earth-acquisition sequence	246			30
4	Midcourse maneuver sequence	247-248		1	44
5	Earth-reacquisition sequence	248			26
6	Reacquisition sequence loss of orientation	251			30 <sup>c</sup>
7	Reacquisition sequence loss of orientation	272			30 <sup>c</sup>
8	Power failure	304	8	6	52
9	Power failure	319			
10	Planet encounter mode	348			
11	Spacecraft's last signal	003			

<sup>a</sup> Ref. 21.  
<sup>b</sup> Total elapsed time was 129 days, 17 min; cruise-science ON time was 118 days, 4 hr, 15 min.  
<sup>c</sup> Estimated.

**Table 13. Electrometer calibration history**

Day	Temperature range, °F <sup>a</sup>	Calibration step	Duration of calibration, days
242-248	85-89	120	6
248-281	89-100	119	33
281-281	100	118	11 hr
281-315	100-122	117	34
315-325	122-133	118	10
375-337	133-146	119	12
337-001	146-170 <sup>b,c</sup>	120	23

<sup>a</sup> Temperatures are listed in degrees Fahrenheit, the same units used in instrument temperature transducer calibrations.  
<sup>b</sup> Maximum telemeterable temperature was 153°F. Maximum readings during this period were estimated.  
<sup>c</sup> Maximum heating occurred near perihelion, December 27, 1962 (day 361).

shift, if attributable to translational effects in common data elements such as a ground reference, would correspond to a 2.4-step decrease on the eight-bit plasma channel. During this time, the threshold of the discriminator in the electrometer assembly was being regularly exceeded by effects of negative background current. A table of discriminator thresholds obtained from electrometer data maxima revealed a two-step downward shift

concurrent with the change in electrometer calibration. The simultaneous downward shifts of plasma calibration, discriminator threshold, and magnetometer temperature measurements suggest translational or offset effects between at least these two instruments and the staircase generator of the analog-to-digital converter in the DCS. If nominal calibration current is assumed during the flight (actual internal test-current variations about the adjusted value at 23°C are  $\pm 8\%$  at temperatures of  $-10$  and  $+70^\circ\text{C}$ , respectively), preflight temperature-vacuum calibrations can then be normalized to the equivalent step center value of the flight calibration with an uncertainty of  $\pm 11.75$  mv. The uncertainty may be appreciably reduced by interpolation between points on a plot of step-crossings vs. time, especially where the resultant curve is a monotonic function of time.

To extract meaningful data from the instrument with negative or very-low-value positive input currents, one should consider the electrometer operation between the discriminator threshold and the low-current end of the static characteristic. Negative background current may be caused by sunlight reflecting down the blackened, curved deflection plates and liberating electrons from the suppressor electrode. It may also be caused by energetic electrons reaching the collector cup after having been scattered from the walls of the analyzer deflection plates at least twice. This background current fluctuated throughout the flight and on occasion was observed to be as high as  $-10^{-13}$  amp. The minimum net positive current needed to charge the capacitance of the electrometer feedback compressor from the discriminator threshold to the proper point on the static characteristic is calculated to be  $5 \times 10^{-13}$  amp when the voltage excursion is 2 v, the time interval is 20 sec, and the diode capacitance is 5 pf. All net positive currents above  $5 \times 10^{-13}$  amp may be taken directly from the static characteristic. An integration calculation may be used for average positive currents of less than  $5 \times 10^{-13}$  amp when the electrometer feedback capacitance is in a highly discharged state. The integration scale factor for this condition is  $6 \times 10^{-15}$  amp per DCS step per measurement time interval. An electrostatic transient caused by the reed switch coil in sequencing from calibration to energy level No. 1 usually leaves the electrometer output near the discriminator threshold at the end of Step 1. The ability of a  $3 \times 10^{-13}$  amp current to restore the output to its steady-state value within 20 sec is illustrated in the transient record of Fig. 53. Transients occurring in higher steps are produced by the coupling of minute amounts of energy from the deflection system to the electrometer (sometimes by test cables).

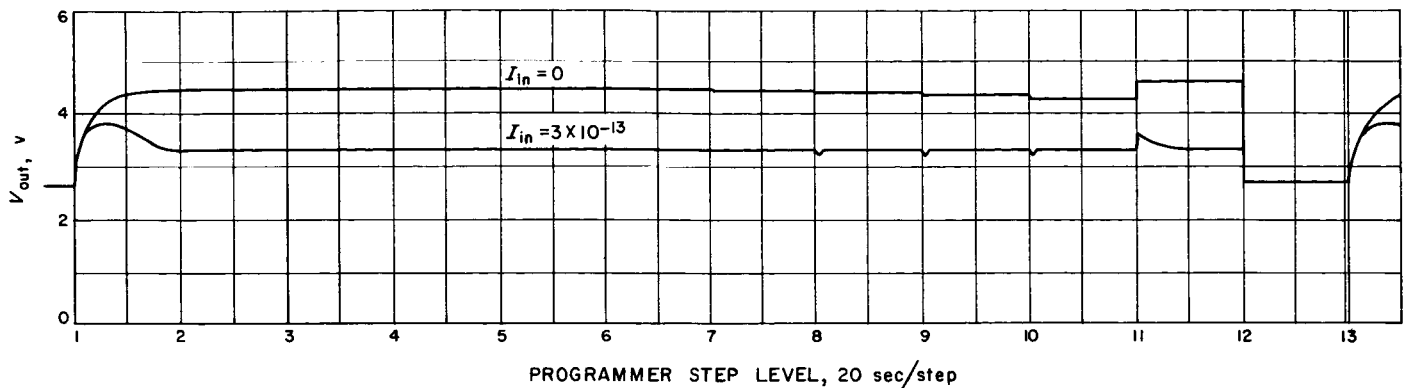


Fig. 53. Electrometer transient response

In the encounter mode, odd-step sampling intervals are reduced to approximately 1/6 of the cruise intervals. In this condition, the minimum current required to charge the electrometer to its correct steady-state value in odd steps, when the feedback capacitance is in the maximum discharged state, is six times the cruise threshold or  $3 \times 10^{-12}$  amp. However, worst-case conditions did not generally apply during actual planet encounter, and most odd-step data were therefore directly usable with no corrections required. Step-1 readings were different from cruise-mode readings owing to the switch coil transient, but even there the results were very predictable.

### 3. Scientific Results

The solar plasma experiment required 3.7 min to acquire a complete energy spectrum of the plasma and during the flight of *Mariner 2*, approximately 40,000 such spectra were obtained. Perhaps the most interesting new information to arise from the very large volume of data on interplanetary fields and particles is the demonstration that solar plasma flowing radially out from the Sun was detectable in every one of the 40,000 spectra obtained in the 4-month mission and is therefore presumably always present.

The solar wind has been explained theoretically as a continuous expansion of the solar corona. *Mariner 2* results show that the velocity of this expansion (if such is the mechanism) undergoes frequent fluctuations. Approximately 20 occasions were seen when the velocity increased within a day or two by amounts of 20 to 100 percent (Ref. 22, 23, 24). Indeed, solar wind velocities observed during the flight varied from 200 to 500 mi/sec. The fluctuations correlate very well with the amount of magnetic disturbance observed on the Earth, and in several cases sudden and sharp increases in the density, velocity, and temperature of the plasma preceded the

onset of sudden magnetic storms on the Earth. The time delay was attributable to the fact that *Mariner* was always inside the Earth's orbit, so that the outward-moving plasma cloud would generally reach the spacecraft first. The following interesting account of one such magnetic disturbance was published on December 7, 1962, before Venus encounter (Ref. 25):

"There were six geomagnetic storms during the period August 29 through October 18. Figure 2 [not included] shows the plasma flux for the period of the geomagnetic storm which started at 2025 UT, October 7. One could see a sudden increase in plasma flux and energy at about 1547 UT, October 7, when the spacecraft was  $8.55 \times 10^6$  km closer to the Sun than was the Earth. If it is assumed that this plasma front was advancing with spherical symmetry and constant velocity from the center of the Sun (at least for the region of space containing the spacecraft and the Earth), then the velocity of the front was 504 km/sec. This velocity corresponds fairly well to the measured plasma velocity spectrum in which more current was measured at 464 km/sec than at 379 or 563 km/sec.

"The discontinuity, or plasma front, passed the spacecraft so quickly that the instrument with its 3.7 min time resolution could not resolve its structure, which must therefore be less than 112,000 km thick. The *Mariner* magnetometer data for this period could be interpreted as showing a front thickness of the order of 50,000 km."

During the flight, scientific data became available in several forms such as quick-look telemetry data, decommutated telemetry data, hand-tabulated copies of the decommutated data, and computer-plotted spectra. Table 14 shows a page of hand-collated data. On this occasion, currents above  $+10^{-13}$  amp were observed only in energy

Table 14. Manually collated plasma data beginning Sept. 24, 1962 (Day 267), 23:55 GMT<sup>a</sup>

DCS frame count	Digitized output (steps) of electrometer for indicated programmer step and corresponding E/Q											
	1 218 v	2 330 v	3 498 v	4 732 v	5 1,104 v	6 1,640 v	7 2,444 v	8 3,644 v	9 5,460 v	10 8,212 v	11 0 v	12 b
43013	238	243	150	123	135	138	153	159	162	164	160	119
43014	238	243	155	126	135	140	154	160	163	164	160	119
43015	238	243	151	125	135	140	154	159	163	164	161	119
43016	238	243	155	123	136	139	154	159	162	164	160	119
43017	238	243	155	124	136	139	154	159	162	163	159	119
43018	238	243	157	124	135	139	154	159	162	164	158	119
43019	238	243	157	124	136	135	152	158	162	163	158	119
43020	238	243	154	124	137	135	153	158	162	163	159	119
43021	238	243	154	124	138	137	154	159	162	164	159	119
43022	238	243	155	123	137	139	154	159	162	163	158	119
43023	238	243	243	122	138	137	153	158	162	163	158	119
43024	238	243	243	123	137	137	152	158	162	163	159	119
43025	238	243	243	122	138	137	153	158	161	163	158	119
43026	238	243	243	123	139	137	153	158	162	163	158	119
43027	238	242	242	122	138	137	153	158	162	163	158	119
43028	238	243	242	123	136	138	154	159	162	163	158	119
43029	238	242	242	122	139	137	155	159	162	164	158	119

<sup>a</sup> Approximate calibration:

DCS step	Input current, amp
119	10 <sup>-10</sup>
129	10 <sup>-11</sup>
139	10 <sup>-12</sup>
149	10 <sup>-13</sup>

<sup>b</sup> Data were obtained with an internal calibration source of 10<sup>-10</sup> amp.

levels 4, 5, and 6. Peak currents at that time were occurring in level 4 with a particle flux corresponding to a current of about  $5 \times 10^{-11}$  amp. Over the course of the experiment, net positive currents were observed in steps 3 to 10 with peaks occurring in steps 4 to 8. The largest

current observed during the flight was about  $4 \times 10^{-10}$  amp. During these periods of intense solar activity, electrometer outputs at supposedly quiet adjacent energy levels gave evidence of an integrating-type discharge corresponding to currents of up to  $-10^{-13}$  amp.

## NOMENCLATURE

### Abbreviations

AMR	Atlantic Missile Range
DAS	Data Automation System
DCS	Data Conditioning System
GSE	Ground Support Equipment

### Symbols

$A$	(1) area (2) amplifier gain
$A_0$	dc voltage gain of entire electrometer $A_0 = G_1 G_2$
$A\beta$	feedback factor, loop gain, or loop transmission ( $F$ )
$C$	coupling capacitance
$C_0$	source capacitance (rest capacitance)
$C2$	coupling capacitor
$C_A$	vacuum dielectric coupling capacitor
$C_B$	equivalent capacitance
$C_D$	interelectrode capacitance
$C_f$	feedback capacitance
$C_o$	collector-to-shield capacitance
$C_v$	instantaneous value of dynamic capacitance
$d$	separation between plates
$E$	energy
$E_{1(oc)}$	open-circuit preamplifier output voltage

$E_c$	(1) contact potential (2) energy required for a trajectory with a constant radius of curvature for normally incident, singly charged particles
$E_D$	average demodulated signal
$E_{in}$	open-circuit output voltage of the triplet amplifier, or equivalent input voltage to demodulator
$E_o$	output voltage
$E_p$	peak voltage
$E_T$	test voltage
$F$	loop transmission ( $A\beta$ )
$F_0$	dc loop transmission
$f_0$	resonant frequency
$f_{gc}$	gain crossover frequency
$f'_{gc}$	gain crossover frequency with secondary feedback
$G_1$	dc voltage gain of carrier section (modulator to demodulator)
$G_2$	gain of dc filter-amplifier
$G_{AC}$	ac voltage gain of carrier amplifier
$H$	transfer impedance normalized to feedback resistance $R_f$
$I$	total emission current
$I_0$	initial-velocity electron current
$i_1$	primary current in preamplifier input transformer

## NOMENCLATURE (Cont'd)

$i_a$	capacitor current during switch closure	$R_{in}$	current-forming resistor connected to electrometer input
$I_B$	transistor base current	$R_{LK}$	leakage resistance
$i_b$	capacitor current during switch opening	$R_p$	resistance seen at primary of preamplifier transformer
$I_c$	circulating current	$R_{ref}$	resistance in reference base of sweep amplifier differential comparator
$I_{co}$	collector cutoff current	$R_S$	Thevenin equivalent resistance of all input and bias networks in sweep amplifier
$I_F$	feedback current	$S_{I_C}$	transistor collector stability factor. $S_{I_C} = \frac{\partial I_C}{\partial I_{co}}$ where $I_C$ = collector current and $I_{co}$ = collector cutoff current
$I_f$	filament current	$T$	temperature in degrees Kelvin
$I_{in}$	input current to diode grid or diode plate	$t$	time
$i_{in}$	transient or instantaneous value of input current	$V_B$	(1) dc bias voltage (2) transistor base voltage
$I_p$	dc plate current	$V_{BE}$	transistor base-to-emitter voltage
$j$	$\sqrt{-1}$	$V_{CE}$	transistor collector-to-emitter voltage
$K$	(1) Boltzmann constant (2) closed-loop gain	$v_c$	voltage across coupling capacitor
$-K_i$	closed-loop gain with infinite feedback factor	$v_{c1}$	coupling capacitor voltage at start of cycle
$M$	slope of the semilog diode characteristic	$v_c(p)$	capacitor voltage as represented in complex ( $p$ ) plane
$N$	number of quantizing steps in analog-to-digital converter	$V_D$	translational offset voltage
$p$	Laplace operator	$V_g$	series generator voltage in feedback loop
$Q$	(1) resonant selectivity $\left( \frac{\text{resonant frequency}}{\text{3-db bandwidth}} \right)$ (2) charge	$V_{in}$	dc input voltage to dynamic capacitor assembly
$q$	electron charge	$V_{nom}$	nominal voltage at center of analog-to-digital converter step
$Q_m$	mechanical $Q$	$V_p$	plate voltage
$R_2$	input resistor to dynamic capacitor	$v_{R_2}$	average demodulated output voltage
$R_A$	equivalent resistance during demodulation switch closure	$v_s$	voltage across secondary of preamplifier input transformer
$R_B$	equivalent resistance during demodulation switch opening	$X_0$	source reactance of modulator capacitance
$R_c$	dynamic resistance of diode CR1 in parallel with R7 and R8	$X_A$	reactance of vacuum dielectric capacitor ( $C_A$ )
$r_D$	dynamic resistance of a diode in its retarded field region	$X_2$	reactance of coupling capacitor C2
$R_F$	sweep amplifier feedback resistance		
$R_f$	electrometer feedback resistance		

## NOMENCLATURE (Cont'd)

$X_g$	equivalent series reactance	$\beta_2$	portion of output returned to secondary damping capacitor
$Z_f$	feedback impedance	$\epsilon_0$	dielectric constant of free space
$Z_{in}$	input impedance	$\eta_c$	conversion efficiency
$Z_{o_1}$	preamplifier open-circuit output impedance	$\eta_D$	demodulation efficiency
$Z_T$	transfer impedance	$\eta_{D_0}$	dc or steady-state demodulation efficiency
$\alpha_i$	inverse short-circuit emitter-to-collector current gain	$\tau$	time constant
$\beta$	(1) short-circuit base-to-collector current gain (2) portion of output returned to summing point	$\omega$	angular frequency
		$\omega_0$	angular resonant frequency

## REFERENCES

1. *Scientific Experiments for Ranger A-1 and A-2*, Technical Memorandum No. 33-4, Jet Propulsion Laboratory, Pasadena, California, March 18, 1960, pp. 9-17.
2. *Scientific Experiments for Ranger 1 and 2*, Technical Report No. 32-55, Jet Propulsion Laboratory, Pasadena, California, January 3, 1961, pp. 15-16.
3. Chamberlain, J. W., "Interplanetary Gas. II. Expansion of a Model Solar Corona," *Astrophysical Journal*, Vol. 131, 1960, pp. 47-56.
4. Parker, E. N., "Dynamics of the Interplanetary Gas and Magnetic Fields," *Astrophysical Journal*, Vol. 128, 1958, pp. 664-676. See also: Parker, E. N., "The Hydrodynamic Treatment of the Expanding Solar Corona," *Astrophysical Journal*, Vol. 132, 1960, pp. 175-183.
5. Bierman, L., "Solar Corpuscular Radiation and the Interplanetary Gas," *Observatory*, Vol. 107, 1957, pp. 109-110. See also: Bierman, L., "Physical Processes in Comet Tails and Their Relation to Solar Activity," *Mémoires de la Société Royale des Sciences de Liège*, Vol. 13 (Series 4), 1953, pp. 291-301.
6. Coleman, P. J., Jr., Davis, L., and Sonett, C. P., "Steady Component of the Interplanetary Magnetic Field: Pioneer V," *Physical Review Letters*, Vol. 5, 1960, pp. 43-46.
7. *The Ranger Program*, Technical Report 32-141 (reprinted from *Astronautics*, Vol. 6, No. 9, September 1961, pp. 22-52), Jet Propulsion Laboratory, Pasadena, California.
8. "Lunar Program," *Space Programs Summary No. 37-11*, Vol. I, Jet Propulsion Laboratory, Pasadena, California, October 1, 1961, pp. 3-4.
9. Bonetti, A., Bridge, H. S., Lazarus, A. J., Lyon, E. F., Rossi, B., and Scherb, F., "Explorer X Plasma Measurements," *Space Research III*, North-Holland Publishing Co., Amsterdam, 1963, pp. 540-542.
10. Bridge, H. S., Lazarus, A. J., Rossi, B., Scherb, F., Lyon, E. F., and Dilworth, C., "Explorer X Interplanetary-Plasma Observations," *IGY Bulletin No. 55*, National Academy of Sciences, January 1962.



## REFERENCES (Cont'd)

11. Neugebauer, M., *The Detection of the Plasma Component of Magnetohydrodynamic Waves in Space*, Technical Memorandum No. 33-93, Jet Propulsion Laboratory, Pasadena, California, June 12, 1962, pp. 10-11.
12. *Scientific Experiments for Mariner R-1 and R-2*, Technical Report No. 32-315, ed. by R. C. Wyckoff, Jet Propulsion Laboratory, Pasadena, California, July 15, 1962, pp. 24-27.
13. Chao, S. K., "Logarithmic Characteristic of Triode Electrometer Circuits," *Review of Scientific Instruments*, Vol. 30, No. 12, December 1959, pp. 1087-1092.
14. Chance, B., Hughes, V., Sayre, D., and Williams, F. C., *Waveforms*, Massachusetts Institute of Technology Radiation Laboratory Series, Vol. 19, McGraw-Hill Book Co., Inc., New York, 1949.
15. Slaughter, D. W., "Reed Drive Oscillator for a Vibrating-Reed Electrometer," *Research Summary No. 36-12*, Vol. 1, Jet Propulsion Laboratory, Pasadena, California, January 2, 1962, pp. 11-13.
16. Palevsky, H., Grenchik, R., and Swank, R. K., "Design of Dynamic Condenser Electrometers," *Review of Scientific Instruments*, Vol. 18, No. 5, May 1947, pp. 298-314.
17. Ebers, J. J., and Moll, J. L., "Large-Signal Behavior of Junction Transistors," *Proceedings of the IRE*, Vol. 42, Part 2, December 1954, pp. 1761-1772.
18. *Cary Model 31-31V Vibrating Reed Electrometer Instruction Manual*, Applied Physics Corporation, Monrovia, California.
19. Harris, L., McGinnies, R. T., and Seigel, B. M., "The Preparation and Optical Properties of Gold Blacks," *Journal of the Optical Society of America*, Vol. 38, 1948, p. 582.
20. Josias, C. S., "Radiation Instrumentation Electronics for the Pioneer III and IV Space Probes," *Proceedings of the IRE*, Vol. 48, April 1960, p. 735.
21. *Flight Performance Report by Spacecraft Data Analysis Team*, Engineering Planning Document No. 149, Jet Propulsion Laboratory, Pasadena, California, February 22, 1963.
22. *Mariner Mission 1962*, Engineering Planning Document No. 129, Jet Propulsion Laboratory, Pasadena, California, April 12, 1963.
23. Snyder, C., Neugebauer, M., and Rao, U. R., *The Solar-Wind Velocity and its Correlation with Cosmic-Ray Variations and with Solar and Geomagnetic Activity*, Technical Report No. 32-514, Jet Propulsion Laboratory, Pasadena, California, October 15, 1963. Also published in the *Journal of Geophysical Research*, Vol. 68, No. 24, December 15, 1963, pp. 6361-6370.
24. Snyder, C., and Neugebauer, M., "Interplanetary Solar-Wind Measurements by Mariner II," to be published in *Space Research IV*, North-Holland Publishing Co., Amsterdam.
25. Snyder, C., and Neugebauer, M., "The Mission of Mariner 2: Preliminary Observation—Solar Plasma Experiment," *Science*, December 7, 1962, pp. 1095-1096.